MEASUREMENT SCIENCE REVIEW, **18**, (2018), No. 3, 86–93

DE GRUYTER OPEN

MEASUREMENT SCIENCE REVIEW

Journal homepage: http://www.degruyter.com/view/j/msr

ISSN 1335-8871

Proportional Error Back-Propagation (PEB): Real-Time Automatic Loop Closure Correction for Maintaining Global Consistency in 3D Reconstruction with Minimal Computational Cost

Morteza Daneshmand[1], Egils Avots[1], Gholamreza Anbarjafari[1,2]

[1]*iCV Research Group, Institute of Technology, University of Tartu, Tartu, Estonia, {ea,md,shb}@icv.tuit.ut.ee*
[2]*Department of Electrical and Electronic Engineering, Hasan Kalyoncu University, Gaziantep, Turkey*

This paper introduces a robust, real-time loop closure correction technique for achieving global consistency in 3D reconstruction, whose underlying notion is to back-propagate the cumulative transformation error appearing while merging the pairs of consecutive frames in a sequence of shots taken by an RGB-D or depth camera. The proposed algorithm assumes that the starting frame and the last frame of the sequence roughly overlap. In order to verify the robustness and reliability of the proposed method, namely, Proportional Error Back-Propagation (PEB), it has been applied to numerous case-studies, which encompass a wide range of experimental conditions, including different scanning trajectories with reversely directed motions within them, and the results are presented. The main contribution of the proposed algorithm is its considerably low computational cost which has the possibility of usage in real-time 3D reconstruction applications. Also, neither manual input nor interference is required from the user, which renders the whole process automatic.

Keywords: 3D reconstruction, global consistency, loop closure correction, Iterative Closest Point, Proportional Error Back-propagation.

1. Introduction

Reconstruction of 3D objects and scenes has various applications in research and industry contexts, examples of which include virtual reality [1–3], 3D Scanning [4], and Simultaneous Localization and Mapping (SLAM) [5] by autonomous systems [6]. The latter goal is usually achieved through taking multiple shots of RGB, depth or RGB-D frames and registering each of them onto the previous one through finding the relevant transformations, using algorithms such as Iterative Closest Point (ICP) [7, 8]. Nevertheless, each individual transformation usually entails a certain level of error, which when accumulated throughout a large sequence, will cause a noticeable misalignment between the two ends.

The problem of correctly closing the loop for achieving global consistency in 3D reconstruction has been investigated and approached through different techniques in the existing literature. In most cases, especially in the presence of large sequences of frames, the latter is necessary. Incrementally tracking the motion by accumulating the drift throughout the frame transformations [9] is one of the earliest examples that has been utilized along with the Structure from Motion (SfM) [10]. The offline optimization procedure proposed in [11] is another early example from the foregoing list.

One of the first algorithms accomplishing real-time performance in creating globally consistent 3D representations of objects based on sequences of frames taken by a handled camera was devised on the basis of probabilistic analysis of feature position approximations [12], which was not capable of dealing with sequences larger than a certain amount. More clearly, due to the high computational cost involved, the latter method will fail to demonstrate real-time performance if a large scene is going to be reconstructed, which demands creating great feature vectors and incorporating them into the calculations. Even with smaller scenes, the amount of data to be handled is larger than what could be sustained along with a dense filter map, which incurs having to ignore some of the features, which is tantamount to reducing the accuracy.

Apart from detecting the loop, the majority of the loop closure correction methods proposed in the literature relies on complex and time-consuming statistical and mathematical algorithms and operations, including computationally expensive optimization procedures, which often require intense manual input and interference from the user as well, practically preventing a real-time functionality, even if other elements of the pipeline comply with it. In [13] the closing of loop is achieved using a pose graph optimization algorithm based on the features extracted using the RGB data, for instance. The foregoing approach is an example of the long list of methods possibly leading to impressive global alignment, but in the case of being exposed to large databases, either delaying the whole reconstruction process or loosing the potential precision and accuracy due to implementing a global fu-

DOI: 10.1515/msr-2018-0013

sion algorithm, which is responsible for reducing the frames to representations that are based on dense patches.

In the article proposed by Steinbrucker et al. [14] the loop closure is estimated based on key-frames, where each new key frame is matched against all previous key frames. The loop closure is detected based on entropy ratio, where a small error between frames coincides with high entropy value.

To reduce the computational cost in frame feature matching, an efficient mechanism detecting loop closures via landmarks is presented in the article by Liu et al. [15]. The landmarks are compared between the incoming images and all landmarks. According to the match information, the loop closure can be detected.

Article by Shiratori et al. [16] describes a method for aligning very large sets of 3D point clouds. From an initial estimate of the sensor paths, a 3D graph is constructed and the alignment problem is decomposed into smaller ones based on the loop closures that exist in this graph. Data is aligned with Simultaneous GICP (S-GICP) that exploits the loop closure property to produce highly accurate intra-loop registration results. The individual loops are then combined into a single, consistent point cloud via an inter-loop alignment step that reconnects the graph of loops, according to a least squares optimization.

The loop-closure problem is most widely explored int the SLAM (simultaneous localization and mapping), where the absence of loop-closure detection and error correction can cause large errors, as it accumulates over the frames. In SLAM problems, usually, a pose graph is built and then corrected using the loop-closure constraint.

A popular approach [17] for this problem is the iSAM [18] algorithm that is based on fast incremental matrix factorization for the correction of transformation matrices. With the help of QR decomposition of the matrix only the values that change are updated, resulting in fast performance. The information matrix was also used for error estimation.
Similar to this solution is the iSAM2 [19] system, where Keiss proposed to use Bayesian trees, a data structure that provides a better understanding of the matrix factorization in terms of probability densities. It was shown how the fairly abstract updates to a matrix factorization translated to a simple editing of the Bayes tree and its conditional densities. As a result this system was faster and more accurate than the previous one.

Another commonly used approach for loop-closure is using RANSAC and keyframes as proposed in [20]. Once detected, to minimize the conflict between sequential constraints and loop closure constraints, TORO [21] was employed. TORO provides a gradient descend based error minimization solution for constraint-networks. The authors ran TORO each time a loop-closure was detected, using the output of the previous run as initial guess.

Even though iSAM, TORO and iSAM2 are a great solution for the SLAM problem, they are overly complicated for simpler and more controlled environments, where building a location graph would be unnecessary.

In this paper, a loop closure correction algorithm with a negligible computational load is proposed, which is referred to as Proportional Error Back-Propagation (PEB), and aims at applications where the sequence always possesses similar first and last frames, whose examples, among others, include scanning a room while stopping at a pose similar to that of the starting frame. The main virtue of the PEB is its unparalleled fastness, i.e. it usually takes a fraction of a second for it to correct the transformations throughout the whole sequence. Such algorithm can be used in producing more realistic models subject to use in virtual fitting rooms or virtual reality applications [22–28].

The remainder of the paper is organized as follows: The proposed method is introduced in the next section. Afterwards, the experimental results are presented and discussed. Finally, the paper is concluded.

2. The Proposed Method

In this section, the underlying idea of the PEB is described, along with the associated mathematical framework. It is worth noticing that in a 3D reconstruction context, various modules shall either precede or succeed the loop closure system, none of which is investigated in this paper, where only a selection of the existing solutions is considered for verifying the efficiency of the PEB. From a broad perspective, the items from the foregoing list may include preprocessing and registering the depth frames and post-processing the resulting point cloud.

The input to the PEB algorithm is a sequence of depth frames, containing the 3D coordinates of the corresponding points in the associated systems, and a set of homogeneous transformations each of which supposedly maps every point in a frame to the system of coordinates through which the points from the one preceding it within the sequence are represented. More clearly, the foregoing transformations have been calculated by a registration algorithm which is expected to find the camera poses for all the frames, based on which it obtains transformations that approximately map every point in a frame to the one matching it in the previous frame.
However, the above transformations are usually not totally accurate, and the negligible error entailed by each of them still contributes to a considerable overall error, which causes overall inconsistency and prevents the reconstruction loop from closing. More clearly, all the points in each frame are supposed to be mapped to their locations in the reference coordinate system, which is tantamount to that of the first frame, by means of a homogeneous transformation resulted from accumulating a sequence of transformations each of which maps them one step backward, i.e. from the coordinate system associated with a frame to that of the one preceding it, where although no outstanding misalignment might show up at every step, the aggregated error may be considerable. The latter errors may have been caused or compounded by a variety of factors, including vibration of the camera or its movement in

directions, or under axes, other than the intended ones and measurement noise.

The purpose of the PEB is to overcome the above error, and correct the loop closure, taking the following principle into account as the criterion: If the first and the last frames are exactly the same, the cumulative homogeneous transformation taking the latter to the former must be equal to the identity transformation. If the aforementioned condition is met, i.e. if the first and the last frames are the same, the overall error is equivalent to the existing cumulative transformation supposedly mapping the last frame to the first one. By the PEB, to correct the foregoing error, it is back-propagated throughout the chain of transformations based on their proportional contribution to the overall transformation.

In order to do so, the rotation and translation components of the transformations are modified separately and respectively, where an extra module mediating between them compensates for the effect of the modification of the rotation on the translation. It should be noted that the condition that the first and the last frames input into the PEB must be the same necessitates making a copy of the first frame and inserting it at the end of the sequence before performing registration, where the difference between the poses of the camera between the first frame and the original last one needs not to be larger than the threshold that could be tolerated by the registration algorithm when finding the transformation mapping one to the other, meaning that the scanning process should finish at a pose close enough to its starting one.

The underlying methodology of the PEB will be described in mathematical terms in what follows. Assuming that n distinct frames, being each stood for by a set F_i, $i = 1,2,\ldots,n$, exist in the whole sequence, the points in the i^{th} one, i.e. F_i, are represented through a Cartesian coordinate system $\mathscr{F}_i$ which is defined by the origin O_i and the axes X_i, Y_i, and Z_i, as follows:

$$\forall j,\ j \in \{1,2,\ldots,n_i\} \Longrightarrow \left[\boldsymbol{p}_{i_{j_{(3\times 1)}}}\right]_{\mathscr{F}_i} \in F_i, \tag{1}$$

where $\boldsymbol{p}_{i_j}$ represents the position vector of the j^{th} point in F_i, namely, P_{i_j}, and n_i is the total number of the points in F_i. It should be noted that i and j are dummy variables to be changed throughout the paper. Then, having in mind that a copy of the first frame, $F_{n+1} = F_1$, has been added to the end of the sequence, i.e. there are now $n+1$ frames in the sequence, upon constructing the homogeneous coordinates of P_{i_j}, namely, $\left\{\boldsymbol{p}_{i_j}\right\}_{\mathscr{F}_i}$, as follows:

$$\begin{gathered}\forall i \forall j, i \in \{1,2,\ldots,n+1\} \wedge j \in \{1,2,\ldots,n_i\} \Longrightarrow \\ \left\{\boldsymbol{p}_{i_j}\right\}_{\mathscr{F}_i} = \left[\left[\boldsymbol{p}_{i_j}\right]_{\mathscr{F}_i}^{\mathrm{T}} \quad 1\right]^{\mathrm{T}},\end{gathered} \tag{2}$$

the homogeneous transformation matrix $\boldsymbol{T}_{i_{(4\times 4)}}$, which has been obtained by the registration algorithm, maps the homogeneous coordinates of every point in the $(i+1)^{\text{th}}$ frame, $\left\{\boldsymbol{p}_{i+1_j}\right\}_{\mathscr{F}_{i+1}}$, from its native coordinate system, being $\mathscr{F}_{i+1}$, to that of a point $\left\{\boldsymbol{p}^*_{i+1_{j_{(3\times 1)}}}\right\}_{\mathscr{F}_i}$ supposed to match it in the preceding one, namely, $\mathscr{F}_i$, meaning that:

$$\begin{gathered}\forall i \forall j, i \in \{1,2,\ldots,n\} \wedge j \in \{1,2,\ldots,n_{i+1}\} \Longrightarrow \\ \left\{\boldsymbol{p}^*_{i+1_j}\right\}_{\mathscr{F}_i} = \boldsymbol{T}_i \left\{\boldsymbol{p}_{i+1_j}\right\}_{\mathscr{F}_{i+1}},\end{gathered} \tag{3}$$

where:

$$\boldsymbol{T}_i = \begin{bmatrix} \boldsymbol{Q}_{i_{(3\times 3)}} & \boldsymbol{t}_{i_{(3\times 1)}} \\ \boldsymbol{0}_{(1\times 3)} & 1 \end{bmatrix}, \tag{4}$$

in which $\boldsymbol{Q}_i$ and $\boldsymbol{t}_i$ stand for a rotation matrix and a translation vector, respectively, and $\boldsymbol{0}$ denotes a vector of all-zeros. If the camera poses have been calculated flawlessly, the latter transformation will map the homogeneous coordinates of every point from the corresponding coordinate system to its own representation in the coordinate system associated with the previous frame, i.e. ideally, $\left\{\boldsymbol{p}^*_{i+1_j}\right\}_{\mathscr{F}_i}$ should be equivalent to $\boldsymbol{T}_i \left\{\boldsymbol{p}_{i+1_j}\right\}_{\mathscr{F}_{i+1}} = \left\{\boldsymbol{p}_{i+1_j}\right\}_{\mathscr{F}_i}$, which is usually not the case, due to the errors having, as aforementioned, arisen because of a variety of reasons. The foregoing inconsistency explains the cause of the loop closure error, i.e. the accumulation of the error throughout the transformations prevents the ends of a closed loop of the frames from coinciding with each other at the pose they are supposed to do.

In order to define measures describing the overall error, which is tantamount to the loop closure error and should be back-propagated so as to correct the loop closure by modifying the transformations, one could find the overall transformation supposedly mapping the points from the coordinate system associated with the newly inserted last frame to that of the first frame, which are in fact the same, and upon noticing that ideally it has to become an identity homogeneous transformation, deriving the loop closure pose error from it. In other words, the accumulation of the first to the n^{th} homogeneous transformations, namely, $\boldsymbol{T}_{T_{(4\times 4)}}$, which can be found as follows:

$$\boldsymbol{T}_T = \prod_{i=1}^{n} \boldsymbol{T}_i, \tag{5}$$

can be considered as a homogeneous transformation constructed on the basis of the parameters standing for the loop closure error, such that with the following representation:

$$\boldsymbol{T}_T = \begin{bmatrix} \boldsymbol{Q}_{T_{(3\times 3)}} & \boldsymbol{t}_{T_{(3\times 1)}} \\ \boldsymbol{0} & 1 \end{bmatrix}, \tag{6}$$

$\boldsymbol{Q}_T$ and $\boldsymbol{t}_T$ denote a cumulative rotation matrix and a cumulative translation vector, respectively, which could be utilized to extract the rotation and translation loop closure errors.

For extracting the loop closure error correction terms based on the overall homogeneous transformation, i.e. $\boldsymbol{T}_T$, first, Eq. (5) can be expanded through substituting each individual

homogeneous transformation by the expression describing it from Eq. (4) in order to find $\boldsymbol{Q}_T$ and $\boldsymbol{t}_T$ in Eq. (6), as follows:

$$\boldsymbol{Q}_T = \prod_{i=1}^{n} \boldsymbol{Q}_i, \quad \boldsymbol{t}_T = \sum_{i=1}^{n} \left(\prod_{j=0}^{i-1} \boldsymbol{Q}_j \right) \boldsymbol{t}_i, \tag{7}$$

where $\boldsymbol{Q}_{0_{(3\times3)}} = \boldsymbol{I}_3$ is an identity matrix.
In fact, the goal of the PEB is to find modified rotation matrices $\hat{\boldsymbol{Q}}_{i_{(3\times3)}}$ and translation vectors $\hat{\boldsymbol{t}}_{i_{(3\times1)}}$, according to the original ones $\boldsymbol{Q}_i$ and $\boldsymbol{t}_i$, respectively, $i = 1,2,\ldots,n$, based on their proportional contributions to the overall rotation matrix $\boldsymbol{Q}_T$ and the overall translation vector $\boldsymbol{t}_T$, respectively, such that the resulting homogeneous transformation matrices $\hat{\boldsymbol{T}}_{i_{(4\times4)}}$ constructed as follows:

$$\hat{\boldsymbol{T}}_i = \begin{bmatrix} \hat{\boldsymbol{Q}}_i & \hat{\boldsymbol{t}}_i \\ \boldsymbol{0} & 1 \end{bmatrix}, \tag{8}$$

would overall accumulate the identity homogeneous transformation, represented by the 4×4 identity matrix $\boldsymbol{I}_4$, meaning that:

$$\hat{\boldsymbol{T}}_T = \begin{bmatrix} \hat{\boldsymbol{Q}}_T & \hat{\boldsymbol{t}}_T \\ \boldsymbol{0} & 1 \end{bmatrix} = \prod_{i=1}^{n} \hat{\boldsymbol{T}}_i = \boldsymbol{I}_4, \tag{9}$$

where $\hat{\boldsymbol{Q}}_T$ and $\hat{\boldsymbol{t}}_T$ denote the corrected cumulative rotation matrix and the corrected cumulative translation vector, respectively.

In the context of the transformation correction procedure of the PEB, first, the rotation matrices are corrected. The purpose is to modify each rotation matrix $\boldsymbol{Q}_i$, $i = 1,2,\ldots,n$, such that the corrected overall rotation would become an identity rotation. In order to do so, a set of rotation correction matrices $\boldsymbol{Q}_{e_{i_{(3\times3)}}}$, $i = 1,2,\ldots,n$, should be calculated to be incorporated into the construction of the corresponding corrected rotation matrices. In what follows, the proposed mathematical framework for achieving the latter goal is explained, where the virtue of the fact that the inverse of every rotation matrix is equal to its own transpose has been resorted to for the sake of reducing the consequent computational cost.

In order to format the structure of the rotation correction procedure, an expression for each corrected rotation matrix, $\hat{\boldsymbol{Q}}_i$, $i = 1,2,\ldots,n$, in terms of the rotation and rotation correction matrices, is first derived in a way that would enable the algorithm to manipulate the corrected overall rotation, which must become identity, by adjusting the rotation correction matrices. To this end, the cumulative rotation matrices $\boldsymbol{Q}_{c_{i_{(3\times3)}}}$, $i = 1,2,\ldots,n$, and their corrected counterparts $\hat{\boldsymbol{Q}}_{c_{i_{(3\times3)}}}$ are defined as follows:

$$\boldsymbol{Q}_{c_i} = \prod_{j=1}^{i} \boldsymbol{Q}_j, \quad \hat{\boldsymbol{Q}}_{c_i} = \prod_{j=1}^{i} \hat{\boldsymbol{Q}}_j. \tag{10}$$

Then by noticing that each corrected cumulative rotation matrix should assimilate all the associated rotation correction matrices, meaning that:

$$\forall i,\, i \in \{0,1,\ldots,n\} \Longrightarrow \hat{\boldsymbol{Q}}_{c_i} = \left(\prod_{j=0}^{i} \boldsymbol{Q}_{e_j} \right) \boldsymbol{Q}_{c_i}, \tag{11}$$

where $\boldsymbol{Q}_{e_0} = \boldsymbol{I}_3$, a closed-form expression can be found for the corrected rotation matrices $\hat{\boldsymbol{Q}}_i$, $i = 1,2,\ldots,n$, as follows:

$$\begin{aligned} \forall i,\, i \in \{1,2,\ldots,n\} \Longrightarrow \hat{\boldsymbol{Q}}_{c_i} = \hat{\boldsymbol{Q}}_{c_{i-1}} \hat{\boldsymbol{Q}}_i \Longrightarrow \hat{\boldsymbol{Q}}_i = \hat{\boldsymbol{Q}}_{c_{i-1}}^{\mathrm{T}} \hat{\boldsymbol{Q}}_{c_i} = \\ \left(\left(\prod_{j=0}^{i-1} \boldsymbol{Q}_{e_j} \right) \boldsymbol{Q}_{c_{i-1}} \right)^{\mathrm{T}} \left(\prod_{j=0}^{i} \boldsymbol{Q}_{e_j} \right) \boldsymbol{Q}_{c_i} = \\ \boldsymbol{Q}_{c_{i-1}}^{\mathrm{T}} \left(\prod_{j=0}^{i-1} \boldsymbol{Q}_{e_j} \right)^{\mathrm{T}} \left(\prod_{j=0}^{i-1} \boldsymbol{Q}_{e_j} \right) \boldsymbol{Q}_{e_i} \boldsymbol{Q}_{c_i} = \boldsymbol{Q}_{c_{i-1}}^{\mathrm{T}} \boldsymbol{Q}_{e_i} \boldsymbol{Q}_{c_i}, \end{aligned} \tag{12}$$

where $\boldsymbol{Q}_{c_0} = \hat{\boldsymbol{Q}}_{c_0} = \boldsymbol{I}_3$.
Assuming that the accumulation of the above rotation correction matrices is represented as $\boldsymbol{Q}_{e_{T_{(3\times3)}}}$, which is calculated as follows:

$$\boldsymbol{Q}_{e_T} = \prod_{i=1}^{n} \boldsymbol{Q}_{e_i}, \tag{13}$$

one has:

$$\hat{\boldsymbol{Q}}_T = \left(\prod_{i=1}^{n} \boldsymbol{Q}_{e_i} \right) \boldsymbol{Q}_T = \boldsymbol{I}_3 \Longrightarrow \prod_{i=1}^{n} \boldsymbol{Q}_{e_i} = \boldsymbol{Q}_T^{\mathrm{T}}, \tag{14}$$

meaning that $\boldsymbol{Q}_{e_T}$ shall become the inverse of the overall rotation matrix, i.e. $\boldsymbol{Q}_T$, meaning that the individual rotation correction matrices can be constructed such that they stand for rotations around the same axis as that of $\boldsymbol{Q}_T$, but lead to rotation angles which accumulate the negation of that of $\boldsymbol{Q}_T$. Therefore, assuming that $\boldsymbol{Q}_T$ is represented by $\boldsymbol{e}_T$ and ϕ_T as the unit vector along the rotation axis and the rotation angle, respectively, using the same rotation axis and the following rotation angles:

$$\forall i,\, i \in \{1,2,\ldots,n\} \Longrightarrow \phi_{e_i} = -\frac{|\phi_i|}{\sum_{i=1}^{n} |\phi_i|} \phi_T, \tag{15}$$

meaning that:

$$\sum_{i=1}^{n} \phi_{e_i} = -\sum_{i=1}^{n} \frac{|\phi_i|}{\sum_{i=1}^{n} |\phi_i|} \phi_T = -\phi_T, \tag{16}$$

the corresponding rotation correction matrices, i.e. $\boldsymbol{Q}_{e_i}$, can be obtained, where ϕ_i stands for the rotation angle associated with $\boldsymbol{Q}_i$, the ratio $\frac{|\phi_i|}{\sum_{i=1}^{n} |\phi_i|}$ being meant to make each rotation correction matrix proportional to the contribution of the corresponding original rotation matrix to the overall one.

However, the correction of the rotation matrices affects the translation vectors as well. More clearly, while the rotations are being fixed, further drift will be introduced into the alignments, which appears as a higher level of error in the translations. Therefore, the translations are first revised such that

the effect of the changes in the rotation would be minimized. In order to do so, it is assumed that the average position of the points from a given frame must be affected in the same manner before and after revising the corresponding rotation, which can be mathematically represented as follows:

$$\begin{gathered}\forall i,\, i \in \{1,2,\ldots,n\} \Longrightarrow \boldsymbol{Q}_i \frac{\sum_{j=1}^{n_{i+1}} \boldsymbol{p}_{i+1_j}}{n_{i+1}} + \boldsymbol{t}_i = \\ \hat{\boldsymbol{Q}}_i \frac{\sum_{j=1}^{n_{i+1}} \boldsymbol{p}_{i+1_j}}{n_{i+1}} + \boldsymbol{u}_i \Longrightarrow \boldsymbol{u}_i = \boldsymbol{t}_i + \left(\boldsymbol{Q}_i - \hat{\boldsymbol{Q}}_i\right) \frac{\sum_{j=1}^{n_{i+1}} \boldsymbol{p}_{i+1_j}}{n_{i+1}},\end{gathered} \tag{17}$$

where $\boldsymbol{u}_i$, $i = 1,\ldots,n$, is the revised translation vector. Thus, the overall translation based on the newly obtained rotation matrices and translation vectors could be found based on Eq. (7), as follows:

$$\boldsymbol{v}_T = \sum_{i=1}^{n} \left(\prod_{j=0}^{i-1} \hat{\boldsymbol{Q}}_j \right) \boldsymbol{u}_i = \hat{\boldsymbol{Q}}_{c_{j-1}} \boldsymbol{u}_i, \tag{18}$$

Similarly to what preceded regarding correcting the rotations, when it comes to doing so on the translations, the above vector, i.e. $\boldsymbol{v}_T$, can be considered as the new overall translation error, since given the fact that the sequences consisting of $n+1$ frames stands for a fully closed loop with identical first and last frames, if the transformations had been calculated perfectly, then it would need to become zero.

Thus the task of correcting the translations will consist of distributing the aforementioned overall translation error to the individual translation vectors, $\boldsymbol{u}_i$, proportionally to their contributions. The latter are represented as follows:

$$\begin{gathered}\forall i,\, i \in \{1,2,\ldots,n\} \Longrightarrow \boldsymbol{v}_i = \begin{bmatrix} v_{i_1} & v_{i_2} & v_{i_3} \end{bmatrix}^{\mathrm{T}} = \\ \hat{\boldsymbol{Q}}_{c_{j-1}} \boldsymbol{u}_i.\end{gathered} \tag{19}$$

Thus the translation correction vectors can be constructed as follows:

$$\begin{gathered}\forall i,\, i \in \{1,2,\ldots,n\} \Longrightarrow \boldsymbol{t}_{e_i} = \\ -\begin{bmatrix} |v_{i_1}| & |v_{i_2}| & |v_{i_3}| \end{bmatrix}^{\mathrm{T}} \oslash \sum_{j=1}^{n} \left(\begin{bmatrix} |v_{j_1}| & |v_{j_2}| & |v_{j_3}| \end{bmatrix}^{\mathrm{T}} \right) \odot \boldsymbol{v}_T,\end{gathered} \tag{20}$$

which are proportional to the corresponding contributions $\boldsymbol{v}_i$ to the overall error, i.e. $\boldsymbol{v}_T$, and their cumulative value is its negation, being realized as follows:

$$\begin{gathered}\sum_{i=1}^{n} \boldsymbol{t}_{e_i} = \\ -\sum_{i=1}^{n} \left(\begin{bmatrix} |v_{i_1}| & |v_{i_2}| & |v_{i_3}| \end{bmatrix}^{\mathrm{T}} \oslash \sum_{j=1}^{n} \left(\begin{bmatrix} |v_{j_1}| & |v_{j_2}| & |v_{j_3}| \end{bmatrix}^{\mathrm{T}} \right) \odot \boldsymbol{v}_T \right) = \\ -\sum_{i=1}^{n} \left(\begin{bmatrix} |v_{i_1}| & |v_{i_2}| & |v_{i_3}| \end{bmatrix}^{\mathrm{T}} \right) \oslash \sum_{j=1}^{n} \left(\begin{bmatrix} |v_{j_1}| & |v_{j_2}| & |v_{j_3}| \end{bmatrix}^{\mathrm{T}} \right) \odot \boldsymbol{v}_T = \\ -\boldsymbol{v}_T.\end{gathered} \tag{21}$$

Subsequently, the revised contributions to the overall translation are obtained as follows:

$$\forall i,\, i \in \{1,2,\ldots,n\} \Longrightarrow \hat{\boldsymbol{v}}_i = \boldsymbol{v}_i + \boldsymbol{t}_{e_i} = \hat{\boldsymbol{Q}}_{c_{j-1}} \boldsymbol{u}_i + \boldsymbol{t}_{e_i}. \tag{22}$$

Lastly, in order to incorporate the above conclusion into the calculation of the corrected translation vectors, Eq. (19) is recalled, and the relationship between the translation contribution vectors found through Eq. (22) and the corrected translation vectors is establishes as follows:

$$\forall i,\, i \in \{1,2,\ldots,n\} \Longrightarrow \hat{\boldsymbol{v}}_i = \hat{\boldsymbol{Q}}_{c_{j-1}} \hat{\boldsymbol{t}}_i, \tag{23}$$

based on which, utilizing Eq. (22), the corrected translation vectors can be obtained as follows:

$$\begin{gathered}\forall i,\, i \in \{1,2,\ldots,n\} \Longrightarrow \hat{\boldsymbol{t}}_i = \hat{\boldsymbol{Q}}_{c_{j-1}}^{\mathrm{T}} \hat{\boldsymbol{v}}_i = \\ \hat{\boldsymbol{Q}}_{c_{j-1}}^{\mathrm{T}} \left(\hat{\boldsymbol{Q}}_{c_{j-1}} \boldsymbol{u}_i + \boldsymbol{t}_{e_i} \right) = \boldsymbol{u}_i + \hat{\boldsymbol{Q}}_{c_{j-1}}^{\mathrm{T}} \boldsymbol{t}_{e_i}.\end{gathered} \tag{24}$$

3. Experimental Results and Discussion

As mentioned before, the PEB has been devised such that given the assumption that the sequence showing a sequence or object possesses first and last frames which have been taken from similar poses, the raw transformations which have been found using an alignment method could be revised, thereby removing the apparent overall misalignment from the point cloud resulting from merging the individual depth maps.

A typical task to be left upon the PEB could be to modify the preliminary outcome of a standard 3D reconstruction pipeline consisting of filming an object while being rotated on top of a turntable, using an RGB-D sensor such as the Microsoft Kinect 2 RGB-D camera [29]. In such a scenario, although the individual transformations may appear to be reasonable, the slight misalignments present in them usually accumulate, and appear as a noticeable diversion between the parts of the reconstructed point cloud corresponding to the initial and final images from the sequence.

Thus, the aim of the PEB would be to distribute the overall misalignment to the individual transformations, so that the structure of the object would be maintained. Similarly, if a scene, e.g., a rectangular room, has been filmed instead, the PEB can be employed to modify an initial reconstructed point cloud.

However, filming scenes, as opposed to objects, usually takes a higher number of frames, which is due to the fact that every pair of consecutive frames fed into an alignment algorithm need to have been taken such that the pose of the camera in the second frame relatively to that of the first one would lead to a reasonable difference, in order for the optimization routine to converge with a tolerable level of error. More clearly, if the pairs of consecutive frames are too different from each other, then the transformation returned by the alignment algorithm may be wrong enough for the PEB to perform weakly in terms of compensating for the present misalignments.

Thus due to the higher number of frames, and as a result, transformations reconstructing a scene are usually associated with higher levels of misalignments, handling which would be more challenging for the PEB. Therefore, in this paper, it is assumed that if the capabilities of the PEB are verified in modifying reconstructions of scenes, its reliability in reconstructing objects would be implied as well. Based on the latter

Fig.1. The first initial reconstruction result.

Fig.2. The second initial reconstruction result.

Fig.3. The third initial reconstruction result.

Fig.4. The corrected counterpart of the result shown in Fig. 1.

Fig.5. The corrected counterpart of the result shown in Fig. 2.

Fig.6. The corrected counterpart of the result shown in Fig. 3.

reasoning, in this paper, the performance of the PEB is examined only in the context of reconstructing scenes, where rectangular rooms are considered as case-studies. The sequences have been taken using Kinect 2.

While filming, it is ensured that the camera will stop at a pose which is close to the starting one, being demanded by the PEB. In order to evaluate the performance of the PEB under arbitrary conditions, and examine its robustness, various trajectories have been considered for the motions of the camera, which include wavy patterns and movements of the camera in the opposite direction of the general trend. The latter is necessary for realizing whether the PEB could handle cases where the experimental setup requires the user to perform indisciplined movements, e.g., due to the restrictions caused by the lengths of the cables connecting the camera and the computer to each other, as well as to the electricity outlet.

The sequences considered for the purpose of evaluating the PEB consist of series of RGB-D frames taken while the user moves throughout the room and holds the camera such that it is facing a part of one of the walls at all of the timestamps, which leads to around 500 frames for a 3×4 m rectangular room, using a frame-rate of 30 Hz. The foregoing frames have all been intentionally kept and fed into the reconstruction pipeline, i.e. downsampling has been avoided, for the sake of introducing a strong amount of misalignment, thereby verifying the robustness of the PEB.

The initial results of reconstructing the sequences using the Iterative Closest Point (ICP) [30] algorithm are shown in Figs. 1 through 3, whose counterparts which have been improved through applying the PEB can be found in Figs. 4 through 6, in the same order.

It is noteworthy that the end of the sequence is determined by taking the first frame of the sequence and iteratively comparing it to the frames from the end of the sequence, starting from the last frame and going backwards. The frame similarity is determined by SSIM and once a frame with highest similarity is found, the process is stopped. If the first frame is placed at the end of a partial loop, the algorithm will still consider the sequence as a full loop, meaning that the final results will be incorrect. Currently the implementation, does not check for such cases.

As it could be seen from the results shown in the aforementioned figures, although the PEB incurs a negligible computational load, it provides a reliable platform for revising the transformations returned by a typical alignment algorithm such as ICP, which leads to smoothly distributing the overall error to the relative poses, thereby obtaining a visually appealing representation of the scene that believably corresponds to the expected 3D structure.

4. Conclusion

In this paper, a fast loop closure correction algorithm, namely, Proportional Error Back-Propagation (PEB), was proposed, which performs the task in a fraction of a second on a sequence of frames meant to reconstruct a 3D representation of a scene, where the overall transformation error is distributed to the individual relative poses proportionally to their contributions to the cumulative transformation. The underlying assumption was that the initial and final frames from the sequence need to be taken at similar poses of the camera, which makes it a suitable choice for reconstructing a room, where the camera films its surroundings trying to stop at a similar pose as it had started. The proposed method was verified in terms of visual and computational efficiency through applying it to a variety of sequences. The future works may involve incorporating the possibility of correcting the transformations in case multiple closures appear in a given sequence of frames.

Acknowledgement

This work has been partially supported by Estonian Research Council Grants (PUT638), The Scientific and Technological Research Council of Turkey (TÜBiTAK) (Proje 1001 - 116E097) , the Estonian Centre of Excellence in IT (EXCITE) funded by the European Regional Development Fund and the European Network on Integrating Vision and Language (iV&L Net) ICT COST Action IC1307.

References

[1] Berg, L.P., Vance, J.M. (2017). Industry use of virtual reality in product design and manufacturing: A survey. *Virtual Reality* 21(1), 1–17.

[2] Avots, E., Daneshmand, M., Traumann, A., Escalera, S., Anbarjafari, G. (2016). Automatic garment retexturing based on infrared information. *Computers & Graphics*, 59, 28–38.

[3] Anbarjafari, G., Haamer, R.E., Lusi, I., Tikk, T., Valgma, L. (2018). 3D face reconstruction with region based best fit blending using mobile phone for virtual reality based social media. *Bulletin of the Polish Academy of Sciences Technical Sciences*, 66, 1–11.

[4] Daneshmand, M., Helmi, A., Avots, E., Noroozi, F., Alisinanoglu, F., Arslan, H.S., Gorbova, J., Haamer, R.E., Ozcinar, C., Anbarjafari, G. (2018). 3D scanning: A comprehensive survey. *arXiv:1801.08863 [cs.CV]*.

[5] Bailey, T., Durrant-Whyte, H. (2006). Simultaneous localization and mapping (SLAM): Part II. *IEEE Robotics & Automation Magazine* 13(3), 108–117.

[6] Sim, R., Roy, N. (2005). Global a-optimal robot exploration in SLAM. In *IEEE International Conference on Robotics and Automation (ICRA 2005)*. IEEE, 661–666.

[7] Tomono, M. (2009). Robust 3d SLAM with a stereo camera based on an edge-point ICP algorithm. In *International Conference on Robotics and Automation (ICRA'09)*. IEEE, 4306–4311.

[8] Valgma, L., Daneshmand, M., Anbarjafari, G. (2016). Iterative closest point based 3D object reconstruction using RGB-D acquisition devices. In *24th Signal Processing and Communication Application Conference (SIU)*. IEEE, 457–460.

[9] Beardsley, P.A., Zisserman, A., Murray, D.W. (1997). Sequential updating of projective and affine structure from motion. *International Journal of Computer Vision*, 23(3), 235–259.

[10] Turner, D., Lucieer, A., Watson, C. (2012). An automated technique for generating georectified mosaics from ultra-high resolution unmanned aerial vehicle (UAV) imagery, based on structure from motion (SFM) point clouds. *Remote Sensing* 4(5), 1392–1410.

[11] Fitzgibbon, A.W., Zisserman, A. (1998). Automatic camera recovery for closed or open image sequences. In: *Computer Vision – ECCV'98*. Springer, 311–326.

[12] Curless, B., Levoy, M. (1996). A volumetric method for building complex models from range images. In: *23rd Annual Conference on Computer Graphics and Interactive Techniques (SIGGRAPH '96). ACM*, 303–312.

[13] Henry, P., Krainin, M., Herbst, E., Ren, X., Fox, D. (2010). RGB-D mapping: Using depth cameras for dense 3d modeling of indoor environments. In: *Experimental Robotics: 12th International Symposium on Experimental Robotics*. Springer, STAR 79, 477-491.

[14] Frank Steinbrucker, Christian Kerl, J.S., Cremers, D. (2013). Large-scale multi-resolution surface reconstruction from RGB-Dsequences. In: *IEEE International Conference on Computer Vision (ICCV)*. IEEE, 3264-3271.

[15] Liu, T., Zhang, X., Wei, Z., Yuan, Z. (2013). A robust fusion method for RGB-D SLAM. In: *Chinese Automation Congress (CAC)*. IEEE, 474–481.

[16] Shiratori, T., Berclaz, J., Harville, M., Shah, C., Li, T., Matsushita, Y., Shiller, S. (2015). Efficient large-scale point cloud registration using loop closures. In: *International Conference on 3D Vision (3DV)*. IEEE, 232–240.

[17] Whelan, T., Kaess, M., Johannsson, H., Fallon, M., Leonard, J.J., McDonald, J. (2015). Real-time large-scale dense RGB-D SLAM with volumetric fusion. *The International Journal of Robotics Research*, 34(4-5), 598–626.

[18] Kaess, M., Ranganathan, A., Dellaert, F. (2008). ISAM: Incremental smoothing and mapping. *IEEE Transactions on Robotics*, 24(6), 1365–1378.

[19] Kaess, M., Johannsson, H., Roberts, R., Ila, V., Leonard, J.J., Dellaert, F. (2011). ISAM2: Incremental smoothing and mapping using the Bayes tree. *The International Journal of Robotics Research*, 31(2), 216-235.

[20] Wang, Y., Zhang, Q., Zhou, Y. (2015). Dense 3D mapping for indoor environment based on kinect-style depth cameras. In: *Robot Intelligence Technology and Applications 3.*. Springer, 317–330.

[21] Grisetti, G., Stachniss, C., Grzonka, S., Burgard, W. (2007). TORO - Tree-based netwORk Optimizer. `https://openslam.org/toro.html`.

[22] Wu, J., Cui, Z., Sheng, V.S., Zhao, P., Su, D., Gong, S. (2013). A comparative study of SIFT and its variants. *Measurement Science Review*, 13(3), 122–131.

[23] Daneshmand, M., Aabloo, A., Ozcinar, C., Anbarjafari, G. (2016). Real-time, automatic shape-changing robot adjustment and gender classification. *Signal, Image and Video Processing*, 10(4), 753–760.

[24] Kim, K., Lawrence, R.L., Kyllonen, N., Ludewig, P.M., Ellingson, A.M., Keefe, D.F. (2017). Anatomical 2D/3D shape-matching in virtual reality: A user interface for quantifying joint kinematics with radiographic imaging. In *IEEE Symposium on 3D User Interfaces (3DUI).*, IEEE, 243–244.

[25] Lüsi, I., Anbarjafari, G., Meister, E. (2015). Real-time mimicking of estonian speaker's mouth movements on a 3D avatar using Kinect 2. In *International Conference on Information and Communication Technology Convergence (ICTC)*, IEEE, 141–143.

[26] Kühnapfel, U., Cakmak, H.K., Maaß, H. (2000). Endoscopic surgery training using virtual reality and deformable tissue simulation. *Computers & Graphics*, 24(5), 671–682.

[27] Traumann, A., Daneshmand, M., Escalera, S., Anbarjafari, G. (2015). Accurate 3D measurement using optical depth information. *Electronics Letters*, 51(18), 1420–1422.

[28] Daneshmand, M., Aabloo, A., Anbarjafari, G. (2015). Size-dictionary interpolation for robot's adjustment. *Frontiers in Bioengineering and Biotechnology*, 3, 63.

[29] Microsoft Corporation. Kinect for Windows. `https://developer.microsoft.com/en-us/windows/kinect`.

[30] Besl, P.J., McKay, N.D. (1992). Method for registration of 3-D shapes. In *Robotics-DL tentative*, SPIE, 586–606.

Received October 01, 2017.
Accepted April 25, 2018.

MEASUREMENT SCIENCE REVIEW, **18**, (2018), No. 3, 94–99

DE GRUYTER OPEN

MEASUREMENT SCIENCE REVIEW

ISSN 1335-8871

Self-Organizing Map Classification of the Extremely Low-Frequency Magnetic Field Produced by Typical Tablet Computers

Darko Brodić[1], Alessia Amelio[2], Ivo R. Draganov[3]

[1]*University of Belgrade, Technical Faculty in Bor, 19210 Bor, Serbia, dbrodic@tfbor.bg.ac.rs*
[2]*DIMES, University of Calabria, 87036 Rende (CS), Italy, aamelio@dimes.unical.it*
[3]*Faculty of Telecommunications at Technical University of Sofia, Sofia 1000, Bulgaria, idraganov@tu-sofia.bg*

In this paper, the extremely low frequency magnetic field produced by the tablet computers is explored. The measurement of the tablet computers' magnetic field is performed by using a measuring geometry previously proposed for the laptop computers. The experiment is conducted on five Android tablet computers. The measured values of the magnetic field are compared to the widely accepted TCO safety standard. Then, the results are classified by the Self-Organizing Map method in order to create different levels of safety or danger concerning the magnetic field to which tablet computer users are exposed. Furthermore, a brief comparison of the obtained magnetic field levels with the ones from typical laptops is performed. At the end, a practical suggestion on how to avoid the high exposure to the low frequency magnetic field emitted by the tablet computers is given.

Keywords: Classification, magnetic field, measurement, Self-organizing map, tablet computers.

1. Introduction

The artificial magnetic field is a byproduct of the electric current, which flows through electrical or electronic devices. Accordingly, the magnetic field is present everywhere in our environment. It is characterized by its frequency. The time varying magnetic field produced by electrical gadgets contains an Extremely Low Frequency (ELF) component. The ELF magnetic field typically includes frequencies from 30 Hz to 300 Hz. The magnetic field is strong if it is close to the emitter. Also, it rapidly decreases in the case of extremely low frequencies if we are getting away from the source. It is worth noting that some materials can block or rapidly decrease the level of magnetic field spreading.

A magnetic field with different frequencies can interact with the human body creating internal currents [1]. Although it is not destructive as the ionizing radiation, such as gamma or x-rays, it has some potential negative effects on humans. At extremely low frequencies, the levels of induced currents inside the body are too small to produce meaningful effects. However, such magnetic field induces currents within the human body, which can be sufficient to produce a variable effect on humans during long work. Also, there is no doubt that a short-term exposure to very high levels of magnetic field can be harmful to the human health. The current public concern focuses on possible long-term health effects caused by an exposure to magnetic fields at levels below those required to trigger acute biological responses. Up until now, the extensive research in many studies, which have been conducted in the area of the ELF magnetic field, has not given a clear answer on how it is harmful to human health. With more and more available research expertise, it has become increasingly likely that an exposure to magnetic fields determines serious health hazards. Nevertheless, some uncertainties remain. The original scientific discussion about the interpretation of controversial results has shifted to become a societal as well as an economic issue.

International safety standards concerning the magnetic fields have been developed to establish the level of exposure to the magnetic field which is not harmful to the human health. Accordingly, the standards for low frequency magnetic fields ensure that induced electric currents are below the normal level of background currents within the body. During the measurement of low frequency magnetic fields, the magnetic flux density has been characterized in terms of field amplitude and WP index [2], [3], that implement the weighted peak approach, well-suited in the case of complex waveforms. The security limits for exposure to a magnetic field are different according to different authors: 0.2 μT [4], 0.4 μT [5], and 1 μT [6]. Also, an exposure to 1 μT of magnetic field reduces the total sleep time as well as sleep efficiency [6]. The widely accepted TCO standard proposes the following: (i) a prescribed geometry for the measurement of the magnetic field (measured at 0.30 m in front of and around the emitter) and (ii) a test procedure with reference values of the magnetic

DOI: 10.1515/msr-2018-0014

flux density in the frequency region between 5 Hz and 2 kHz [7].

A tablet computer, tablet for short, represents a mobile computer, which includes a touchscreen display, circuitry, and battery. Also, it is equipped with sensors, cameras, a microphone, and an accelerometer. The touchscreen display typically uses finger recognition to replace the mouse and keyboard. The keyboard is given as a pop-up virtual keyboard which is used for typing. The tablet can also include some physical buttons. They are used for basic features such as speaker volume and power, and ports for network communications and battery charging. The tablet is usually characterized by screen size. It is supposed that the tablets incorporate a screen from 7" to 10" wide.

In this paper, we pay special attention to the ELF magnetic field produced by the tablets. Hence, an experiment is conducted in order to measure, evaluate, and classify the ELF magnetic field to which the users are exposed. Accordingly, the high frequency magnetic field from the tablets' components like WIFI, 3G/4G or similar is out of the scope of this paper. To the best of our knowledge, this is one of the first studies that analyze this problem. It has great importance because of the wide-spreading of the tablets among the younger population. It is worth noting that the experiment is conducted on typical tablets. It means that we tested 5 tablets with screens from 7" to 10" wide, working in the "normal" operating condition. This condition means that the tablets are only used for Internet browsing. The tested tablets operate under the most widely spread tablet operating system, i.e. Android. In this way, we test the tablets in similar or the same conditions. The tablets are usually made of gorilla glass material at their top, and of plastic material at their bottom. At the end, we make the assumption that the users' hands are in close contact with the touch area as well as its back. Hence, we accustom the measuring geometry to this way of using the tablets.

The rest of the paper is organized as follows. Section 2 describes the elements of the measuring method, the measuring equipment, the proposed measuring geometry, and the experiment. Section 3 gives the results of the measured ELF magnetic field. Section 4 explains the classification technique, which will be used for the classification of the obtained measurement results. Section 5 presents the classification of the measurement results in order to establish the dangerous and safe levels of the magnetic field. At the end, Section 6 draws the conclusions.

2. Methods and Materials

2.1. Magnetic fields

In the normal operating condition, the inner components of the tablet are supplied by a current I. In this way, the current I flows through these electronic or electrical components inducing a magnetic field. This magnetic field is registered and measured by measuring devices. Usually, these devices register the scalar components of the magnetic induction: B_x, B_y, and B_z as well as the Root Mean Square (RMS) of the magnetic induction B, which is calculated as:

$$B = \overline{B_x + B_y + B_z}. \quad (1)$$

2.2. Measuring devices

The magnetic field measurement is performed by the measuring device Lutron EMF-828 with separate probe, which includes the sensing head as well as the spectrum analyzer AARONIA NF-5030.

Lutron EMF-828 measures the scalar components of the magnetic induction B_x, B_y, and B_z in the range between 0.01 μT and 2 mT. It is measured in the ELF range, i.e. between 30 and 300 Hz. The device has three measurement extents: 20 μT, 200 μT, and 2 mT. The precision of the measurement is of the order of 0.01 μT for the measurement extent of 20 μT, 0.1 μT for the measurement extent of 200 μT, and 1 μT for the measurement extent of 2 mT. Also, the measurement is confirmed by the measuring device AARONIA NF-5030. This device registers the minimum, maximum, average, and RMS magnetic induction in the range between 1 pT and 2 mT. It covers the full ELF range between 1 Hz and 30 MHz. It has six predefined measurement extents in the given frequency range. However, each user can adjust the measuring device in order to register the magnetic field amplitude in a custom-defined frequency measurement range.

2.3. The measuring geometry

The method consists of measuring the ELF magnetic field produced by the tablet computers. The measuring geometry consists of 22 measurement points on the surface of and around the tablet. It is an integration of the previously proposed measuring geometry for portable computers [8], [9] and an improvement of the measuring geometry proposed in the TCO standard [7]. The magnetic field is measured: (i) at nine different positions at the tablet touchscreen at the top, (ii) at nine different positions at the bottom of the tablet, and (iii) at four positions around the tablet (30 cm away from the edge of the tablet). This measuring geometry is chosen as a considerable extension to the TCO proposed measuring geometry [7]. We have strong reasons to accept the new proposed measuring geometry because of the typical way of using the tablet. Usually, the tablet users are in direct and constant contact with the top and the bottom part of the tablet with their fingers. Hence, the geometry proposed by TCO does not give a real condition of the exposure of the tablet users to the magnetic field. Fig. 1 shows the measuring positions at the top and bottom of the tablet computer.

2.4. Experiment

The experiment was conducted on 5 different tablet computers. All tablets use the Android operating system. The tablets are tested in their typical working condition, i.e. during Internet browsing. The magnetic field is measured ten times at the measuring positions: (i) at the top: tbmp1 ... tbmp9 (top body measurement point - tbmp), (ii) at the bottom: bbmp1 ... bbmp9 (bottom body measurement point - bbmp) [8], [9],

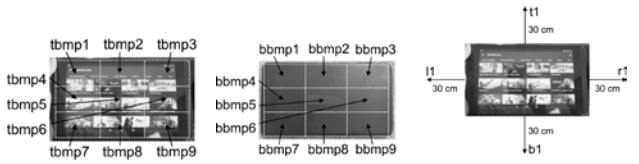

Fig. 1. Measuring positions of the tablet: (a) at the top (tbmp1,...,tbmp9), (b) at the bottom (bbmp1,...,bbmp9), (c) 30 cm away from the edge of the tablet (t1,b1,l1,r1)

and (iii) at four measuring positions away from the edge of the tablet (t1,b1,l1,r1). The average values of the measurement are used as reference. Hence, we measure the magnetic field of the tablets at no distance from the touchscreen display or its bottom. We make this assumption taking into account the typical use of the tablet where the users' fingers are positioned on its top and/or bottom parts all the time. Fig. 2 shows a typical way of using a tablet.

Fig.2. A typical way of using a tablet

3. Measurement Results

At the four measuring positions away from the edge of the tablet (t1,b1,l1,r1), the obtained magnetic field was below 0.02 μT. It can be considered as a background magnetic field. Hence, it is negligible.

The measurement results of the magnetic field for all tablets Tj where j=1,...,5 are given in Fig. 3.

Each area is characterised by a number representing the value of the emitted magnetic field in μT. As a thresholding (dangerous) level, we used the proposed TCO reference level of 0.2 μT.

Table 1 shows the values of ELF magnetic field that are emitted by the top and bottom parts of the tablets in the min-max manner.

Table 1. Measured magnetic field at the top and bottom part of the tablet given in the min-max manner (in μT)

Tablet	Top Min.	Top Max.	Bott. Min.	Bott. Max.
T1	0.04	0.15	0.05	0.20
T2	0.06	0.43	0.07	0.86
T3	0.02	0.22	0.01	0.51
T4	0.05	0.86	0.05	0.96
T5	0.06	0.45	0.07	0.11

From Table 1 (see max. values), we can see that all tablets have some dangerous areas, which emit a magnetic field value above the safety reference level. Also, 3 out of 5 tablets have dangerous values on both sides, i.e. at the top as well as bottom. Also, it is worth noting that the left and right side areas are the most exposed to the tablet users due to the typical way of using them.

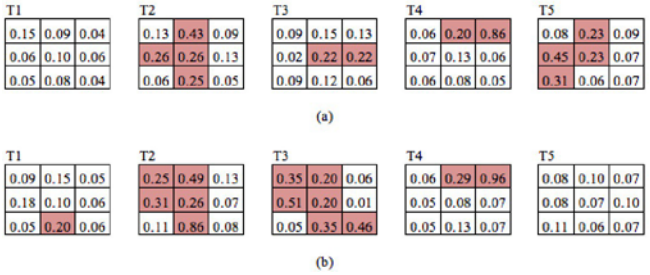

Fig. 3. Magnetic field measurement results given in μT: (a) measured values at the top areas of the tablets (touchscreen display area), (b) measured values at the bottom areas of the tablets. Colored fields represent the areas with higher magnetic field than it is allowed by the TCO standard ($\geq 0.2\mu T$) [7]

4. Self-Organizing Map Classification

In our analysis, we use a one-dimensional Self-Organizing Map (SOM) [10] to classify the measured values. It was selected because of its ability to adapt to the shape of the input data in order to manage a large variety of samples, and to cluster complex data sets in acceptable time. Furthermore, the SOM usually works fine in various applications, as it correctly finds the classification of the data points. Finally, the SOM revealed its potential in discretising numerical values in different contexts [11]. All these aspects make the SOM an invaluable model to be employed in multiple domains where other methods fail to accurately classify the input data. The adopted SOM is characterised by one input neuron and 5 output neurons. Fig. 4 illustrates the applied SOM.

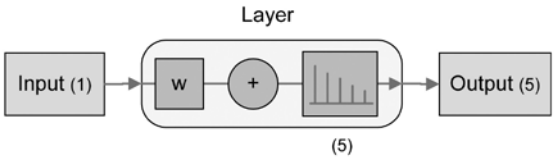

Fig.4. Illustration of the applied SOM structure

All neurons are initialized at the center of the feature space which corresponds to all the values from the minimum (typically 0) to a maximum of the magnetic induction *B*. For each experiment, the inputs are all 9 measured values for the given set of tablets at one of their sides, e.g., at the top and later at the bottom parts in their typical workload. The training of the network includes changes for the weights and bias by following the learning rules with incremental updates after each presentation of an input [12]:

$$w_i(t+1) = w_i(t) + h_{ci}(t)[x(t) - w_i(t)], \qquad (2)$$

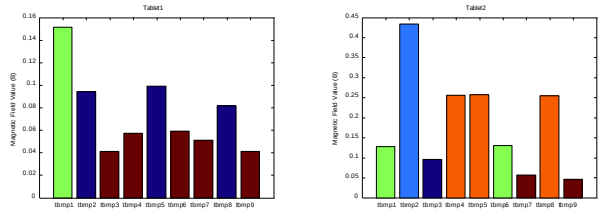

(a) T1 (b) T2

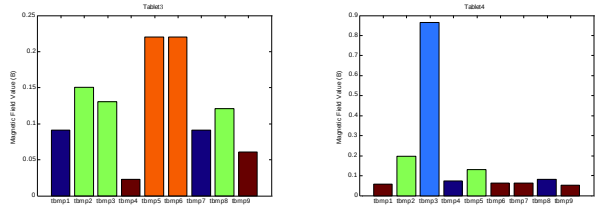

(c) T3 (d) T4

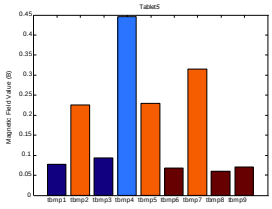

(e) T5

Fig. 5. Classification of the five tablets' magnetic field values at all nine measuring top positions (tbmp1...tbmp9)

Fig.6. Dangerousness maps of the ELF magnetic field levels for the top parts of the measured tablets

where $w_i(t)$ is the i-th weight of the network at time t; h_{ci} - the neighborhood function; x - the current input vector, and i=1...5.

The inputs are presented in random order for 1000 epochs in each simulation. Every training sample causes changes in the position of the nearest neuron, the most in accordance to the update value - an increment by which the neuron is moved towards the current position of the input. The Euclidean distance is used here as a measure [12]:

$$c = argmin_i ||x - w_i|| = argmin_i \sqrt{(x_0 - w_{i0})^2 + \cdots + (x_k - w_{ik})^2}, \quad (3)$$

where x and w_i are one-dimensional for this particular realization. All other neurons change their position in a lighter degree. After reaching the end of the last epoch, the training is finished and the position of all neurons along the B axis gives the cluster centroids. This is the final step of the clustering process.

In the next stage, which is the simulation of the network for every tablet at the given mode and side, all induction values are independently passed one by one through the input. Inside the SOM, the closest neuron is found for them by calculating the Euclidean distance to all 5 weights and selecting the minimal from them. A number from 1 to 5 is generated at the output denoting the associated class which the current test sample belongs to. Thus, the classification process takes place.

5. Classification Results and Discussion

Fig. 5 shows the classification results (5 classes) from all five tablets measured at the top positions. If we project the ELF magnetic field levels obtained by the classification into the measuring positions, then we can build a map of ELF magnetic field dangerousness levels. This map is shown in Fig. 6.

The ELF magnetic field levels are given in Table 2.

Table 2. The ELF magnetic field levels obtained by the SOM classification for the top parts of the tablets in the min-max manner (in μT)

Magnetic field level	Dangerousness	Min.	Max.
L1 (cyan)	Highly Dangerous	0.43	0.86
L2 (orange)	Dangerous	0.22	0.31
L3 (green)	Middle Safe	0.12	0.20
L4 (blue)	Safe	0.07	0.10
L5 (brown)	High Safe	0.02	0.07

From Table 2, we can see that the top part of the tablet emits two dangerous levels of ELF magnetic field, which are L1 and L2, and three safe levels of ELF magnetic field, which are L3, L4, and L5. The highest peak is 0.86 μT, which is much higher than the safety reference limit of 0.2 μT [7].

From Fig. 5, we can observe that 40-60% of the top positions in most of the tablets emit Highly Dangerous and Dangerous levels or a Middle Safe level, which is a borderline level of values just below or equal to the safety reference limit of 0.2 μT.

From the top dangerousness maps of Fig. 6, we can notice that the Highly Dangerous, Dangerous, and Middle Safe levels mostly cover the areas where CPU and RAM are located. It can be observed in T4, where the Highly Dangerous and Middle Safe levels of ELF magnetic field are obtained in correspondence with the RAM, followed by the CPU, with values of 0.86 μT, 0.2 μT and 0.13 μT, respectively. Also, in T5 the RAM and CPU emit a Dangerous level, with values of 0.31 μT and 0.23 μT, respectively. Also, in T1 the highest peak of ELF magnetic field is obtained in correspondence with the CPU, emitting a Middle Safe level with a value of 1.15 μT. Similar considerations can be performed for T2 and T3, where the areas emitting Highly Dangerous and Dangerous levels have a correspondence with the CPU and RAM, with the highest peaks of 0.43 μT and 0.22 μT, respectively.

Fig. 7 shows the classification results (5 classes) for all five tablets measured at the bottom positions. The ELF magnetic field levels projected into the measuring positions provide the

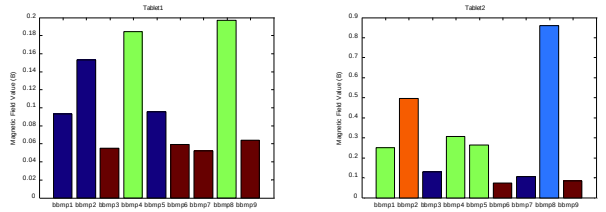

(a) T1

(b) T2

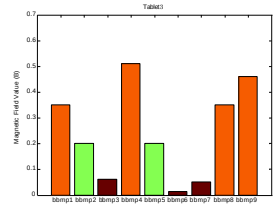

(c) T3

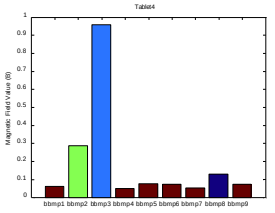

(d) T4

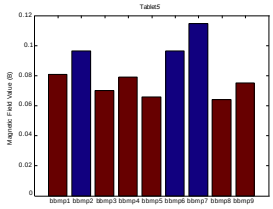

(e) T5

Fig. 7. Classification of the five tablets' magnetic field values at all nine measuring bottom positions (bbmp1...bbmp9)

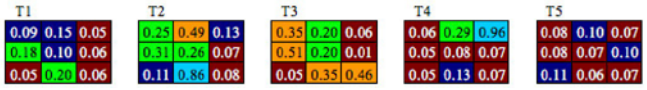

Fig.8. Dangerousness maps of the ELF magnetic field levels for the bottom parts of the measured tablets

dangerousness maps of the ELF magnetic field levels given in Fig. 8.

The ELF magnetic field levels are given in Table 3.

Table 3. The ELF magnetic field levels obtained by the SOM classification for the bottom parts of the tablets in the min-max manner (in μT)

Magnetic field levels	Dangerousness	Min.	Max.
L1 (cyan)	Highly Dangerous	0.86	0.96
L2 (orange)	Middle Dangerous	0.35	0.51
L3 (green)	Dangerous	0.18	0.31
L4 (blue)	Safe	0.09	0.15
L5 (brown)	High Safe	0.01	0.08

From Table 3, we can realize that the bottom part of the tablet emits three dangerous levels of ELF magnetic field, i.e. L1, L2, and L3, and only two safe levels of ELF magnetic field, i.e. L4 and L5. L3 is a borderline level, because it includes some values which are just below the safety reference limit of 0.2 μT [7]. However, it is considered as a dangerous level, because most of the included values are above the reference limit of 0.2 μT. The highest peak of ELF magnetic field is 0.96 μT, which is noticeably higher than the safety reference limit of 0.2 μT.

Fig. 7 shows that two out of five tablets, i.e. T2 and T3, have 50-60% of positions emitting Highly Dangerous, Middle Dangerous or Dangerous levels. The other two tablets, T1 and T4 have 20% of positions with Highly Dangerous or Dangerous levels. Finally, the last tablet, T5, safely emits at its bottom positions.

From the bottom maps in Fig. 8, it is confirmed that the positions emitting the highest dangerous levels are mostly associated with the RAM and CPU. It indicates that these components not only have an influence on the top part, but also on the bottom part of the tablet. On the contrary, it is interesting to observe that the battery has only an influence in ELF magnetic field emission on the bottom part of the tablet, because of its disposition in the tablet case. In particular, in T4 the position where the CPU is located emits a Highly Dangerous level, with a value of 0.96 μT, followed by the position where the RAM is located, emitting a Dangerous level, with a value of 0.29 μT. Also, in T1 a Dangerous level is obtained in the area where the battery is positioned, with the highest peak of 0.20 μT. Finally, T2 and T3 obtain Highly Dangerous, Middle Dangerous and Dangerous levels in the area of the CPU, RAM, and battery. In particular, in T2 the highest peak of ELF magnetic field is reached at the Highly Dangerous level, with a value of 0.86 μT. In T3, the highest peak is obtained at the Middle Dangerous level, with a value of 0.51 μT. In both cases, this peak is much higher than the safety reference limit of 0.2 μT.

A comparison between the top and the bottom ELF magnetic field levels shows that the bottom part emits higher dangerous levels than the top part. It is clearly visible from Tables 2 and 3. In fact, Highly Dangerous level is higher for the bottom part than for the top part of the tablet. Also, Middle Dangerous level is detected as a bottom range, but not detected as a top range. Dangerous level is very similar for the top and bottom parts. However, it is worth noting that the bottom part of the tablet adds a dangerous level (Middle Dangerous) which is not emitted at the top part of the tablet. On the contrary, Middle Safe level is emitted by the top part of the tablet (see Table 2), but it is not found at the bottom part of the tablet (see Table 3). Hence, a safe level is emitted at the top part, but not emitted at the bottom part. On the other hand, it is worth noting from Fig. 5 that most of the tablets have 40-60% of top positions with dangerous levels of ELF magnetic field. It is different from Fig. 7 where only 2 out of 5 tablets have 50-60% of bottom positions with dangerous levels. Nonetheless, in the last case, the ELF magnetic field value associated with these bottom positions is much higher than the value of the first case associated to the top positions.

From the aforementioned results, it is worth noting that the tablets do not emit the same level of measured magnetic field, which is emitted by the laptops [1], [8], [9], [13]. However, their intensity is still above the safety reference level proposed by TCO. To have a fair comparison between the tablets' and

laptops' ELF magnetic field emission, we only have to compare the emitted magnetic field of the battery powered devices. In these conditions, the laptops emit an ELF magnetic field between 0.2 μT and 4.5 μT at the top body (case) parts and between 0.2 μT and 3.5 μT at the bottom body parts [8]. On the contrary, the tablets emit an ELF magnetic field at the top body parts between 0.02 μT and 0.86 μT and at the bottom body parts between 0.01 μT and 0.96 μT.

Also, the comparison between tablets and laptops should take into account that the tablets have much less processing power than the laptops. Furthermore, they typically work as battery powered devices. Hence, an objective comparison can be only established with laptops working in battery mode. Also, it is worth noting that the tablets emit a higher level of magnetic field at their bottom parts compared to their top parts. This result is similar to the laptops. However, the reasons for such ELF magnetic field emission are different in laptops and tablets. The primary reason for a higher ELF magnetic field at their bottom parts are battery, CPU, and RAM memory. Furthermore, it can be assumed that the gorilla glass as a material has a lower magnetic field permeability than the plastic one. Hence, the top of the tablets is much more resistant to the magnetic field spreading than the bottom of the tablets. It is very important for a safe use of the tablets, because they are held in the users' hands. Consequently, some precautions are necessary during the tablets use. The most important suggestion is to keep a safe distance of 30 cm for usage. In fact, visually impaired people may tend to read text close to their eyes. This also happens with children that usually play games on tablets. Of course, this has a relation with the magnetic field decay around the tablet.

6. Conclusions

The proposed study represents one of the first measurement experiments linked with the ELF magnetic field to which the tablet users are exposed. It is very important, because the tablets are very popular and spread in the younger population. Hence, the real determination of the tablets' emitted ELF magnetic field is invaluable for their users as well as for designers of the tablets. Furthermore, the measured magnetic field values were compared to the widely accepted safety standard, i.e. TCO. The results of the study showed that the level of magnetic field is typically above the safety limits. Hence, some precautions during the work with the tablets are necessary. Accordingly, an important suggestion for the safe use of the tablets was proposed.

7. Acknowledgement

This work was partially supported by the Grant of the Ministry of Education, Science and Technological Development of the Republic of Serbia, as a part of the project TR33037.

References

[1] Bellieni, C.V., Pinto, I., Bogi, A., Zoppetti, N., Andreuccetti, D., Buonocore, G. (2012). Exposure to electromagnetic fields from laptop use of "laptop" computers. *Archives of Environmental & Occupational Health*, 67(1), 31–36.

[2] ICNIRP (2010). Guidelines for limiting exposure to time-varying electric and magnetic fields (1 Hz to 100 kHz). *Health Physics*, 99(6), 818–836.

[3] ICNIRP (2014). Guidelines for limiting exposure to electric fields induced by movement of the human body in a static magnetic field and by time-varying magnetic fields below 1 Hz. *Health Physics*, 106(3), 418–425.

[4] Gurney, J.G., Mueller, B.A., Davis, S., Schwartz, S., Stevens, R., Kopecky, K. (1996). Childhood brain tumor occurrence in relation to residential power line configurations, electric heating sources, and electrical appliance use. *American Journal of Epidemiology*, 143(2), 120–128.

[5] Ahlbom, A., Bridges, J., De Seze, R., Hillert, L., Juutilainen, J., Mattsson, M.O., Neubauer, G., SchÄL'z, J., Simko, M. and Bromen, K. (2008). Possible effects of electromagnetic fields (EMF) on human health-opinion of the scientific committee on emerging and newly identified health risks (SCENIHR). *Toxicology*, 246(2-3), 248–250.

[6] COMAR. (1997). Biological and health effects of electric and magnetic fields from video display terminals. A technical information statement. *IEEE Engineering in Medicine and Biology Magazine*, 16(3), 87–92.

[7] TCO Development AB. (2012). *TCO Certified Notebooks 4.0*. `http://tcodevelopment.com/files/2013/04/TCO-Certified-Notebooks-4.0.pdf`

[8] Brodić, D., Amelio, A. (2015). Classification of the extremely low frequency magnetic field radiation measurement from the laptop computers. *Measurement Science Review*, 15(4), 202–209.

[9] Brodić, D., Amelio, A. (2016). Detecting of the extremely low frequency magnetic field ranges for laptop in normal operating condition or under stress. *Measurement*, 91, 318–341.

[10] Oja, M., Kaski, S., Kohonen, T. (2002). Bibliography of self-organizing map (som) papers: 1998-2001 addendum. *Neural Computing Surveys*, 3, 1–156.

[11] Vannucci, M., Colla, V. (2004). Meaningful discretization of continuous features for association rules mining by means of a SOM. In *European Symposium on Artificial Neural Networks*, 28-30 April 2004, Bruges, Belgium, 489–494. 489–494.

[12] Kohonen, T. (2001). *Self-Organizing Maps*. Springer Series in Information Sciences, Vol. 30.

[13] Zoppetti, N., Andreuccetti, D., Bellieni, C., Bogi, A., Pinto, I. (2011). Evaluation and characterization of fetal exposures to low frequency magnetic fields generated by laptop computers. *Progress in Biophysics and Molecular Biology*, 107(3), 456–463.

Received January 03, 2018.
Accepted April 25, 2018.

MEASUREMENT SCIENCE REVIEW, **18**, (2018), No. 3, 100-106

DE GRUYTER OPEN

MEASUREMENT SCIENCE REVIEW

Journal homepage: http://www.degruyter.com/view/j/msr

ISSN 1335-8871

Development of a Device to Measure Mass and Resuspension Rate of Dust inside Confined Environments

Andrea Malizia[1], Riccardo Rossi[2]

[1]*Department of Biomedicine and Prevention, Faculty of Medicine and Surgery, University of Rome Tor Vergata, Via di Montpellier, No.1, 00133, Rome, Italy, malizia@ing.uniroma2.it*
[2]*Department of Industrial Engineering, University of Rome Tor Vergata, Via del Politecnico, No.1, 00133, Rome, Italy.*

A dust explosion is one of the key security issues for many industrial, pharmaceutical and agro-alimentary plants and for the safety of the workers. We have developed an optoelectronic sensor system to determine the mass of deposited dust and the resuspension rate. The authors also mount antennas on an optoelectronic sensor system to perform measurements remotely. The technique used is based on a non-invasive light absorption method. The paper reports a cost analysis in order to demonstrate the possibility to use, in our optoelectronic sensor system, several sensors to monitor large volume. In this paper the authors present the sensor system, the test and calibration of its components together with the results and the error analysis, demonstrating experimentally what is the maximum and the minimum readable range.

Keywords: Measure, sensor, mass, resuspension rate, non-invasive.

1. Introduction

A dust explosion is one of the key security issues for many industrial plants [1]-[5]. The main cause is the presence of large concentrations of combustible dust in an oxidant atmosphere with the presence of ignition sources. Major damage to the industrial plants is produced when dust is mobilized in confined volumes [6]-[16].

In the laboratory of Quantum Electronics and Plasma Physics (QEP), University of Rome "Tor Vergata", the sensor system with the experiment STARDUST-Upgrade has been developed. It is a cylindrical stainless-steel vessel, where it is possible to replicate Loss of Vacuum Accidents with different conditions [17]-[24].

In the previous experimental campaigns, QEP research group studied the monophase fluid dynamic of STARDUST-U [20]-[23] and, after that, PIV (Particle Image Velocimetry), PTV (Particle Tracking Velocimetry) and SHADOWGRAPH measures have been implemented [17]-[19], [25].

The aim of this paper is to present the calibration and test of a sensor, based on an optical technique, to measure dust mobilization factors together with the results obtained, the error analysis and the limits of the optical technique adopted. The idea is to design a sensor system for dust mobilization replicating this sensor in many positions inside STARDUST-U.

2. Materials and Methods

The technique developed to measure dust mobilization in confined environments (like STARDUST-U) is based on absorption of light. The light that crosses a material is attenuated; the attenuation factors are function of the optical properties and concentration of the material. It is possible to measure the concentration of the material starting from its optical properties [26].

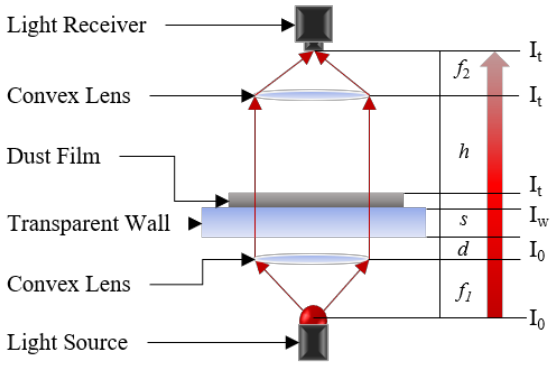

Fig.1. Scheme of the sensor developed to measure the deposited dust.

Fig.1. shows a simplified scheme of the device developed in this work. A light source emits the light, which is parallelized through a first convex lens. Then, the light

DOI: 10.1515/msr-2018-0015

crosses the wall where the dust is deposited. The wall must be transparent to the light source wavelength. Thus, the light passes the measurement region. At the end, a second convex lens converges the light in the light receiver, which reads the transmitted light. The initial intensity of the light is I0. Let us neglect the loss of light intensity due to the lenses. When the light crosses the wall, it loses a portion of light that is function of the Beer-Lambert-Bouguer law. The transmitted intensity is called Iw:

$$I_w = I_0 e^{-\int \sigma N dx} = I_0 e^{-\mu_v x} \quad (1)$$

Where σ is the absorption cross-section of the material, N its molecular concentration and x is the coordinate parallel to the direction of the light propagation. If we use a homogeneous dust layer on the tray, the product of σ with N is constant and the integrative term can be written as $\mu_v x$, where μ_v is the coefficient of linear attenuation. Once the light crosses the measurement region, interacting with the dust, a portion of this light is transmitted (It) and it is a function of dust concentration. If the deposited dust is homogeneous:

$$I_t = I_w e^{-\int \sigma N dx} = I_w e^{-\sigma \bar{N} x} = I_w e^{-\frac{\sigma}{PMA} m} I_w = e^{-\xi \frac{m}{A}} \quad (2)$$

Where PM is the molecular mass, A is the measurement section, m is the mass and ξ is the absorption cross section referred to the mass. Then, the measurement of mass can be achieved by (2):

$$m = \frac{A}{\xi} \ln\left(\frac{I_w}{I_t}\right) \quad (3)$$

Note that the measured mass is the entire mass of dust contained in the measurement volume. We can say that it coincides with the deposited mass only if the resuspended dust is negligible.

In our experimental facility, we are interested in mapping dust mobilization. The large number of these devices needed to map entirely STARDUST-U led to the necessity of developing a low-cost system.

The sensor system comprises a light source, two convex lenses, a light filter, a glass window, and a light detector. The light source is a red LED (High-output solid-state light source). It has a dominant wavelength of 627 nm and the forward voltage is 3.51 V. The first lens (LA-1951 THORLABS) has a focal length equal to 25.4 mm. The second lens (LA-1805 THORLABS) has a focal length equal to 30.0 mm. A light filter (THORLABS NE10A) is used to avoid light source saturation. The light detector is a high-speed silicon detector (THORLABS DET210). Mechanical supports are used to fix each component. Fig.2. shows a photo of the experimental setup described.

A microcontroller (Arduino Uno) [27] is used to power up the light source and read the transmitted intensity. Arduino Uno is a microcontroller board, with some input/output analog/digital pins. One digital output is used to power up the light source. The output voltage is 5 V, and then a resistor is used to decrease the voltage on the LED The light source signal is read through analog input pins. The input pins have a resolution of 10 bits, and their influence on the measurements is analyzed in the results section.

Four different types of dust are used inside STARDUST-Upgrade. They are flour, stainless steel, tungsten, and graphite. The stainless-steel dust is an AISI 814 (Fe/Cr18/Ni10/Mo8) powder, supplied by Good Fellow. The maximum particle size is 45 μm. The carbon dust is a natural graphite powder F, produced by LUBRITECH. It is a very fine dust with a high level of purity, generally used as a solid lubricant. The tungsten dust is a powder with 99.95 % of purity of the Alfa Aesar products. The last dust type is flour. We used a commercial "00" type flour of wheat, normally used for cooking. [24]

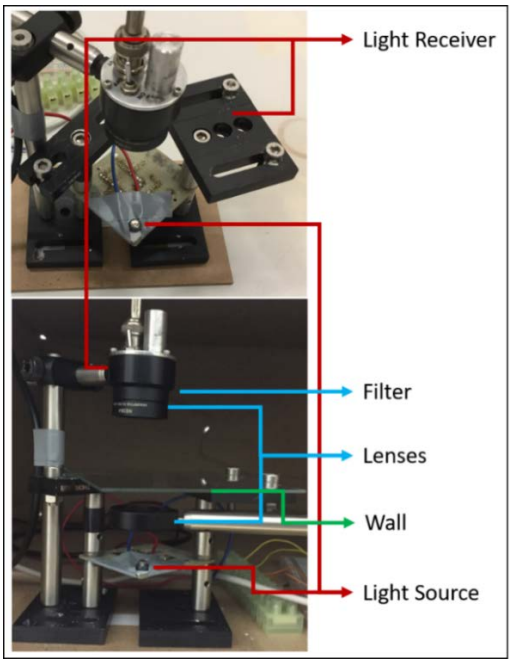

Fig.2. Photo of the sensor system in two different views. This is the device to test, calibrate and analyze the method.

3. RESULTS

A. Calibration

The calibration is performed for each type of dust. At first, the transmitted intensity without dust is measured. We also measured the transmittance of the glass plate, which is 92 %. One hundred measurements have been performed for each dust type. Each measurement follows these steps:

- Deposition of dust over the glass plate. The dust is deposited through a sieve (that has a grid size of 50 μm) in order to avoid agglomerated particles;
- The mass of deposited dust is measured through a precision weighing scale;
- The plate with the dust is positioned in the prototype;
- The light source turns on and the light receiver starts the acquisition. The light receiver performs 300 measurements. The mean and the standard deviation are calculated;
- Light source and receiver turn off and another measurement begins.

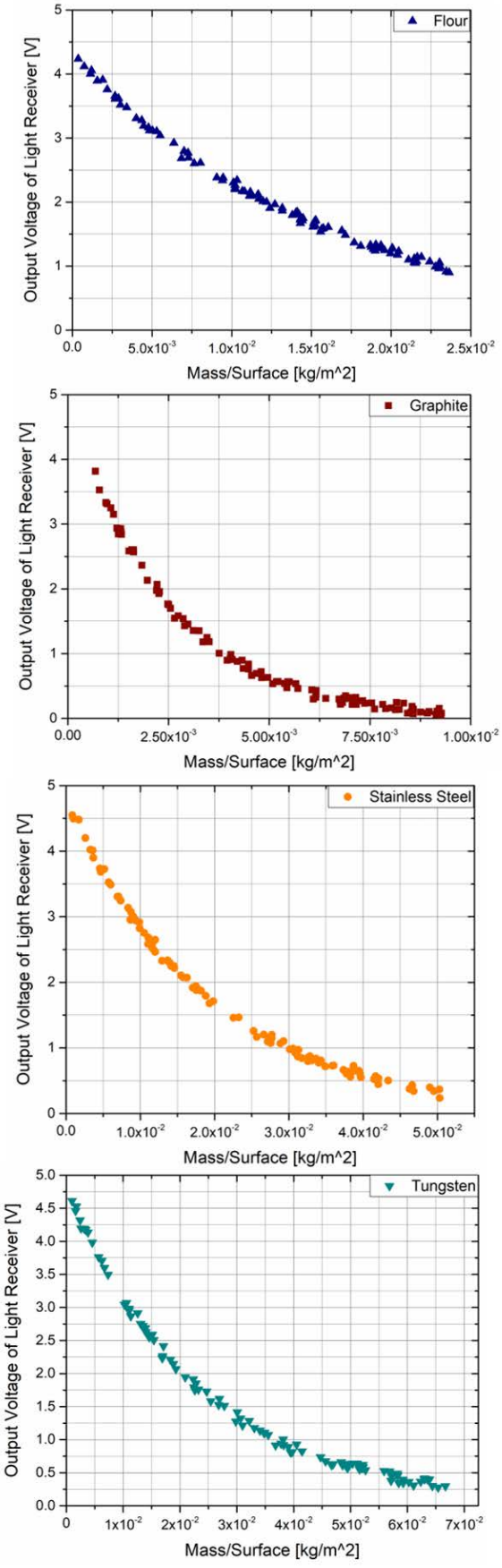

Fig.3. Transmitted intensity (It) in function of mass per surface deposited on the wall.

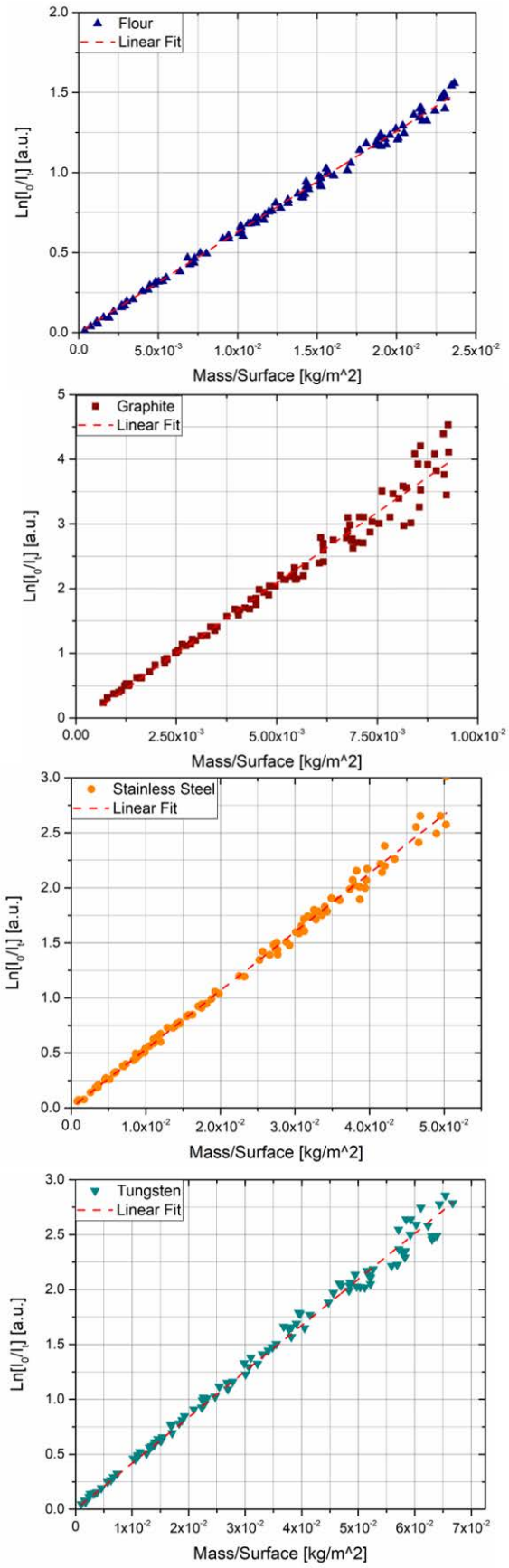

Fig.4. Natural logarithm of intensities ratio in function of mass per surface measured experimentally and the linear fit of the data.

Fig.3. shows the transmitted light in function of the mass deposited on the glass wall. The mass is divided by the analyzed surface. The intensity exponentially decreases according to the Beer-Lambert-Bouguer law. Each point is calculated as the average of 300 consecutive measurements. Now, we have to find the absorption cross-section of each dust type. It can be calculated by means of (3). Then, we calculate the natural logarithm of the ratio between transmitted intensity by glass and mass (I_w/I_t).

Fig.4. shows this variable in function of the mass surface. Then, a linear regression is performed, and the linear curves are shown in the figure. An intercept has been placed at (0,0) since we must have no light intensity variation when there is no mass concentration. Then, we have a curve with a general equation y = mx, where y is the mass per surface (m/A) and x is the natural logarithm of the intensities. Then, the slope coefficient (m) is equal to the absorption cross section (ξ).

Table 1. shows the results of the calibration. The data confirmed the linearity, and the coefficients of determination (R2) are near one.

Table 1. Calculated absorption cross sections and coefficients of determination of the linear regression.

Dust	***ξ [m2/kg]***	***R²***
Flour	62.93	99.59%
Tungsten	41.85	99.20%
SS	53.302	99.41%
Graphite	421.64	97.34%

B. Error analysis of mass measurement

This section shows the error analysis of the method, in order to understand the limits of the techniques and the influence that the microcontroller has on the measurements. Consider (3) and let us apply the equation of error propagation for independent variables [28]:

$$\sigma_m = \sqrt{\left(\frac{\partial m(A,\xi,I_w,I_t)}{\partial A}\,\sigma_A\right)^2 + \left(\frac{\partial m(A,\xi,I_w,I_t)}{\partial \xi}\,\sigma_\xi\right)^2 + \left(\frac{\partial m(A,\xi,I_w,I_t)}{\partial I_w}\,\sigma_{I_w}\right)^2 + \left(\frac{\partial m(A,\xi,I_w,I_t)}{\partial I_t}\,\sigma_{I_t}\right)^2} \quad (4)$$

Where σi is the standard deviation of the variable i. We calculate each term inside the equation:

$$\frac{\partial m(A,\xi,I_w,I_t)}{\partial A}\,\sigma_A = \frac{1}{\xi}\ln\left(\frac{I_w}{I_t}\right)\sigma_A = \frac{A}{\xi}\ln\left(\frac{I_w}{I_t}\right)\frac{\sigma_A}{A} = m\frac{\sigma_A}{A} \quad (5)$$

$$\frac{\partial m(A,\xi,I_w,I_t)}{\partial \xi}\,\sigma_\xi = -\frac{A}{\xi^2}\ln\left(\frac{I_w}{I_t}\right)\sigma_\xi = -m\frac{\sigma_\xi}{\xi} \quad (6)$$

$$\frac{\partial m(A,\xi,I_w,I_t)}{\partial I_w}\,\sigma_{I_w} = \frac{A}{\xi}\frac{I_t}{I_w}\frac{1}{I_t}\sigma_{I_{tw}} = \frac{A}{\xi}\frac{\sigma_{I_w}}{I_w} \quad (7)$$

$$\frac{\partial m(A,\xi,I_w,I_t)}{\partial I_t}\,\sigma_{I_t} = -\frac{A}{\xi}\frac{I_t}{I_w}\frac{I_w}{I_t^2}\sigma_{I_{tw}} = -\frac{A}{\xi}\frac{\sigma_t}{I_t} \quad (8)$$

Using equations (5), (6), (7), and (8) combined with (4) we obtain the following formulation of error propagation for the mass measurement:

$$\sigma_m = \sqrt{\left(m\frac{\sigma_A}{A}\right)^2 + \left(m\frac{\sigma_\xi}{\xi}\right)^2 + \left(\frac{A}{\xi}\frac{\sigma_{I_w}}{I_w}\right)^2 + \left(\frac{A}{\xi}\frac{\sigma_t}{I_t}\right)^2} \quad (9)$$

That equation can be used also to calculate the relative error of the mass:

$$\frac{\sigma_m}{m} = \sqrt{\left(\frac{\sigma_A}{A}\right)^2 + \left(\frac{\sigma_\xi}{\xi}\right)^2 + \left(\frac{1}{\ln\left(\frac{I_w}{I_t}\right)}\frac{\sigma_{I_w}}{I_w}\right)^2 + \left(\frac{1}{\ln\left(\frac{I_w}{I_t}\right)}\frac{\sigma_t}{I_t}\right)^2} \quad (10)$$

This equation is fundamental in the evaluation of error analysis and in understanding the technique limits.

The relative error of the measurement area is function of the first convex lens, its distance from the light source and light source properties, especially the divergence of the emitted light. In fact, the relative distance between light source and lens determines the size of the area and its divergence. The divergence involves a change of the measurement area along the optical axis. The small depth of the deposited dust involves a very small error due to divergence.

The relative error of the absorption cross-section can be calculated in the calibration section. We calculated it through a B method [28] and it was always lower than 5 %.

The influence of both intensities plays an important role. In fact, they are directly proportional to the natural logarithm of their ratio (10). Then, when the mass is very small, and the natural logarithm goes to zero, there is a huge increase in the relative error. We have another critical value of the relative error of mass; that is when the transmitted intensity goes to zero. The error of light intensity is mainly due to the minimum resolution of the light receiver and to random error. Let us neglect the random error influence and call the minimum resolution of the light receiver δ (this parameter is constant).

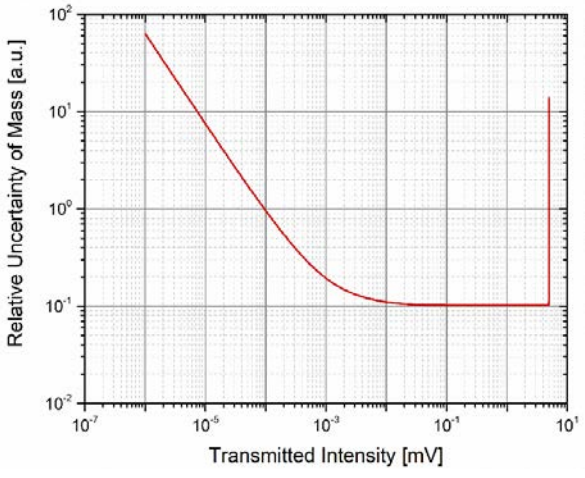

Fig.5. Relative mass error in function of transmitted intensity calculated through error propagation equation.

Fig.5. shows the relative error of mass in function of transmitted intensity. This is calculated by (10), using a relative error of surface equal to 10 % and a no-mass intensity (Iw) equal to 5 mV. The error has been taken constant and equal to 1/210; that is the minimum voltage resolution readable by our instrument. The function has two vertical asymptotes for the transmitted light which tends to zero and to the no-mass intensity (Iw). It implies that there are two limits of transmitted intensity, which limits the minimum and maximum readable mass.

Now, we calculate the experimental error using the experimental data and the model calculated. Then, we compute the error and the relative error as follows:

$$Error_i = \left| m_{exp,i} - \frac{A}{\xi} \ln\left(\frac{I_w}{I_{t,i}}\right) \right| \tag{11}$$

$$Relative\ Error_i = \frac{\left| m_{exp,i} - \frac{A}{\xi} \ln\left(\frac{I_w}{I_{t,i}}\right) \right|}{m_{exp,i}} \tag{12}$$

Where mexp is the mass measured through the weighing scale.

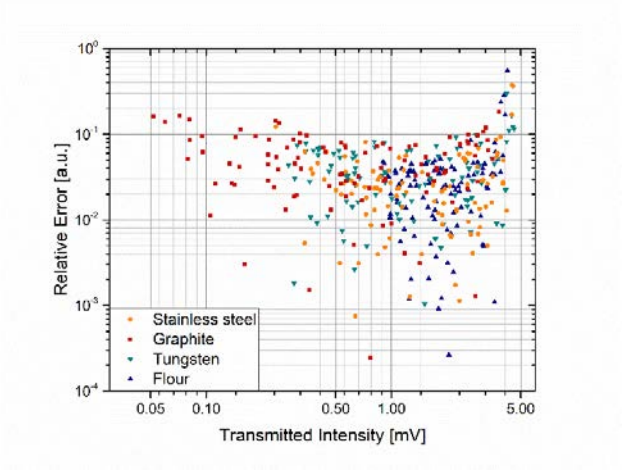

Fig.6. Relative error in function of transmitted intensity. The experimental data confirm the numerical model. We have an asymptote for the transmitted intensity which goes to I_w and to zero.

Fig.6. shows the relative error calculated by the previous (12). This graph confirms what we demonstrated with the analytical analysis the two asymptotic trends for extreme values of transmitted intensity.

The authors show the maximum and minimum readable mass through this method and this sensor system. At first, an acceptable error must be selected (it is arbitrary). In this case, the choice is 10 %. Then, consider the error propagation (10). It follows:

$$\sqrt{\left(\frac{1}{\ln\left(\frac{I_w}{I_t}\right)}\frac{\sigma_{I_w}}{I_w}\right)^2 + \left(\frac{1}{\ln\left(\frac{I_w}{I_t}\right)}\frac{\sigma_t}{I_t}\right)^2} < 0.10 \tag{13}$$

Solving this equation, it is possible to find the maximum and minimum acceptable transmitted intensity. The minimum transmitted intensity is 0.001168 mV and the maximum is 0.499 mV. This limit implies a maximum and a minimum limit of measurable mass, which depends on the absorption cross-section of the dust. The maximum and minimum mass changes for the different dust samples (see Table 2.) and are calculated by (3).

This technique is sensitive to dust in the entire volume of measurements, so deposited dust should not be overestimated. In fact, if there is a cloud of resuspended dust, the transmitted intensity will decrease and then, according to (3), the read deposited mass increase. This error can be neglected only in two cases:

1. The light sensor is very close to the surface. This case is usually unacceptable because of fluid-dynamic interaction with the light sensor. In fact, it may change the fluid-dynamic behavior and then the measurement is falsified.
2. The concentration of resuspended dust is very low. This solution depends on what we are measuring, for example, when we have a low expected concentration in the volume measurement. It may happen when the mass inside the vessel is small and the volume is very large, that is equal to say that the average concentration of dust is low.

Table 2. Calculated absorption cross sections and coefficients of determination of the linear regression.

Dust	ξ [m^2/kg]	*Minimum m/A* [kg/m^2]	*Maximum m/A* [kg/m^2]
Flour	62.93	0.0366	0.1328
Tungsten	41.85	0.0550	0.1998
Steel	53.302	0.0432	0.1568
Graphite	421.64	0.0054	0.0198

C. Remote measurements and cost analysis

We can connect the Arduino board directly to a ZigBee antenna. If we have another antenna in the external environment, connected to a PC, we are able to read the measurements without the use of any cable. It may imply a better isolation of the vacuum vessel. Furthermore, the system could be used also in industrial applications, where usually the distance between the measurement devices and the control room are much larger.

There are a lot of different antennae, which can reach different ranges of distances and frequencies. In our case, we used the XBEE SERIES 1 802.15.4. It has a data rate of 250 kbs, 100 m in indoor range and 1.6 km outdoor. The frequency band is 2.4 GHz.

At last, we performed a cost analysis of sensor. Table 3. shows the costs of each optical device. The light receiver cost is the highest in our sensor system. Anyway, this device has been used because of our laboratory availabilities. Cheaper light receivers can be used and their influence on the experimental setup can be evaluated following the steps in the previous section. Convex lenses and filter have an average cost which depends on their quality. The light source is the cheapest device (our light source costs 1.50 €).

Table 3. Optical device costs.

Optical Device	***Average cost***
Laser source	1.00 – 3.00 €
Convex lenses	20.00 – 45.00 € (each)
Filter	30.00 – 45.00 €
Light receiver	100.00 – 200.00 € (cheaper devices exist)

Table 4. shows the costs of the electrical and electronic components. The electrical conductors depend on their length, and then cost per meter is given. Arduino Uno is the electronic device used to power the light source and read the signal. Its use and influence on the measurement accuracy have been analyzed in the previous section.

Table 3. Electronics and electrical device costs.

Electronic and Electrical Device	***Average cost***
Arduino Uno	15.00 – 30.00 €
Electrical Conductors	1.69 [€/m]

In case of remote measurements, the antenna implementation has an additional cost that depends on the antenna properties. The cost range is around 150.00 €.

The low cost of the apparatus will allow us to set a large number of sensors inside the entire vessel of STARDUST-Upgrade. Through these we will be able to understand where dust re-suspends and deposits, the resuspension rate, and the deposition rate.

4. CONCLUSIONS

Information about dust resuspension and deposition is fundamental to understand the physics of multiphase interactions inside our experimental facility. The absorption-based techniques are well known and used also to perform dust concentration. We developed a sensor to track resuspension and deposition of dust inside our vessel. Since we are interested in the use of several sensors, their cost is another important variable to take into account.

The technique uses a light emitter, two lenses, a transparent wall, and a light receiver. The electronic device is an Arduino Uno and some conductor. This equipment is extremely cheap and the effect of this low quality should be analyzed.

We calibrated our sensor and found the absorption cross-section of each dust type. A good data fit has been found, which means a reliable technique. The error analysis has shown the accuracy of the method and highlighted two important limits. The first limit is the maximum readable dust. When there is too much dust on the surface, the transmitted light is too low and the error due to the maximum resolution of the light receiver dominates the measurement. The other limit is the minimum dust, since the ratio of the intensities goes to one and its logarithm goes to zero. It implies a singularity which makes the measurement wrong.

We also consider the possibility to use an antenna, in our case an XBee, to avoid long wires and connector between the vacuum chamber and external environment.

The cost analysis has been shown and the cost of the instrumentation is very low, especially if we change the light receiver. The cheapness of these devices allows using a lot of them to monitor the entire vessel of STARDUST-Upgrade.

The sensitivity and the limits of this apparatus are acceptable for our aim and we are working on the design and making an instrumentation to set inside the STARDUST-Upgrade facility. Anyway, this kind of application could find also interesting use in industrial fields, where the monitoring of dust may be crucial for safety and health issues.

REFERENCES

[1] Abbasi, T., Abbasi, S. (2007). Dust explosions-Cases, causes, consequences, and control. *Journal of Hazardous Materials*, 140 (1-2), 7-44.

[2] Dust Explosion Info. (2016). *Dust Explosions - the basics.* http://www.dustexplosion.info/dust%20explosions%20-%20the%20basics.htm.

[3] Eckhoff, R.K. (2003). *Dust Explosions in the Process Industries.* Gulf Professional Publishing.

[4] U.S. Chemical Safety and Hazard Investigation Board. (2005). *Investigation digest: Dust explosion at West Pharmaceutical Services*.

[5] U.S. Chemical Safety and Hazard Investigation Board. (2009). *Investigation report: Sugar dust explosion and fire.*

[6] Amyotte, P.R., Eckhoff, R.K. (2010). Dust explosion causation, prevention and mitigation: An overview. *Journal of Chemical Health & Safety*, 17 (1), 15-28.

[7] Eckhoff, R. (2009). Understanding dust explosions. The role of powder science and technology. *Journal of Loss Prevention in the Process Industries*, 22 (1), 105-116.

[8] Gao, W., Mogi, T., Sun, J., Yu, J., Dobashi, R. (2013). Effects of particle size distributions on flame propagation mechanism during octadecanol dust explosions. *Powder Technology*, 249, 168-174.

[9] Giby, J., CSB Hazard Investigation Team. (2007). Combustible dusts: A serious industrial hazard. *Journal of Hazardous Materials*, 142 (3), 589-591.

[10] Hauert, F., Vogl, A., Radandt, S. (1996). Dust cloud characterization and the influence on the pressure-time-history in silos. *Process Safety Progress*, 15 (341), 178-184.

[11] Occupational Safety and Health Administration (OSHA). (2014). *Hazard alert: Combustible dust explosion.* OSHA Fact Sheet, DSG 12, 1-2.

[12] Abuwser, M., Amyotte, P., Khan, F., Morrison, L. (2013). An optimal level of dust explosion risk management: Framework and application. *Journal of Loss Prevention in the Process Industries*, 26 (6), 1530-1541.

[13] Eckhoff, R.K. (1996). Prevention and Mitigation of dust explosions in the process industries: A survey of recent research and development. *Journal of Loss Prevention in the Process Industries*, 9 (1), 3-20.

[14] Yuan, Z., Khakzad, N., Khan, F., Amyotte, P., Reniers, G. (2013). Risk-based design of safety measures to prevent and mitigate dust explosion hazards. *Industrial & Engineering Chemistry Research*, 52 (50), 18095-18108.

[15] Murillo, C., Dufand, O., Bardin-Monnier, N., Lopez, O., Munoz, F., Perrin, L. (2013). Dust explosions: CFD modeling as a tool to characterize the relevant parameters of the dust dispersion. *Chemical Engineering Science*, 104, 103-116.

[16] Federici, G., Skinner, C.H., Brooks, J.N. et al. (2001). Plasma-material interactions in current tokamaks and their implications for next step fusion reactors. *Nuclear Fusion*, 41 (12), 1967.

[17] Poggi, L.A., Gaudio, P., Rossi, R., Ciparisse, J.F., Malizia, A. (2017). Non-invasive assessment of dust concentration and relative dustiness in a dust cloud mobilized by a controlled air inlet inside STARDUST-U facility. *Reliability Engineering and System Safety*, 167, 527-535.

[18] Rossi, R., Malizia, A., Poggi, L.A., Ciparisse, J.-F., Peluso, E., Gaudio, P. (2016). Flow motion and dust tracking software for PIV and dust PTV. *Journal of Failure Analysis and Prevention*, 16 (6), 951-962.

[19] Camplani, M., Malizia, A., Gelfusa, M. et al. (2016). Image computing techniques to extrapolate data for dust tracking in case of an experimental accident simulation in a nuclear fusion plant. *Review of Scientific Instruments*, 87 (1), 013504.

[20] Poggi, L.A., Malizia, A., Ciparisse, J.F. et al. (2016). STARDUST-U experiments on fluid-dynamic conditions affecting dust mobilization during LOVAs. *Journal of Instrumentation*, 11 (7), C07012.

[21] Malizia, A., Poggi, L.A., Ciparisse, J.-F., Rossi, R., Bellecci, C., Gaudio, P. (2016). A review of dangerous dust in fusion reactors: From its creation to its resuspension in case of LOCA and LOVA. *Energies*, 9 (8), 578.

[22] Poggi, L.A., Malizia, A., Ciparisse, J.F., Gelfusa, M., Murari, A., Pierdiluca, S., Lo Re, E., Gaudio, P. (2015). First experimental campaign to demonstrate STARDUST-upgrade facility diagnostics capability to investigate LOVA conditions. *Journal of Fusion Energy*, 34 (6), 1320-1330.

[23] Gaudio, P., Malizia, A., Lupelli, I. (2010). Experimental and numerical analysis of dust resuspension for supporting chemical and radiological risk assessment in a nuclear fusion device. In *International Conference on Mathematical Models for Engineering Science*, 134-147.

[24] Malizia, A., Poggi, L.A., Ciparisse, J.-F., Rossi, R., Bellecci, C., Gaudio, P. (2016). A review of dangerous dust in fusion reactors: From its creation to its resuspension in case of LOCA and LOVA. *Energies*, 9 (8).

[25] Rossi, R., Gaudio, P., Poggi, L.A., Peluso, E., Malizia, A. (2018). Imaging of dust re-suspension in case of LOVA. *Fusion Engineering and Design*, 126, 156-159.

[26] Weiner, J., Ho, P.T. (2003). *Light-Matter Interaction: Fundamental and Applications, Volume 1*. Wiley.

[27] D'Ausilio, A. (2012). Arduino: A low-cost multipurpose lab equipment. *Behavior Research Methods*, 44 (2), 305-313.

[28] Joint Committee for Guides in Metrology (JCGM). (2008). *Evaluation of measurement data – Guide to the expression of error in measurement.* JCGM 100:2008 (Gum 1995 with minor corrections).

Received January 09, 2018.
Accepted April 25, 2018.

MEASUREMENT SCIENCE REVIEW, **18**, (2018), No. 3, 107-112

DE GRUYTER OPEN

MEASUREMENT SCIENCE REVIEW

Journal homepage: http://www.degruyter.com/view/j/msr

ISSN 1335-8871

Design and Construction of Novel Instrumentation for Low-Field MR Tomography

Daniel Gogola[1], Pavol Szomolanyi[1,2], Martin Škrátek[1], Ivan Frollo[1]

[1]*Institute of Measurement Science, Department of imaging method, Dúbravská cesta, 9, 841 04, Bratislava, Slovakia, daniel.gogola@savba.sk*

[2]*High Field MR Centre, Department of Biomedical Imaging and Image-guided Therapy, Medical University of Vienna, Vienna General Hospital, Waehringer Guertel 18-20, A-1090, Vienna, Austria*

Magnetic resonance imaging (MRI) is a very popular tool for diagnostic applications and research studies. Low-field MR scanners, usually with an open design, are suitable for claustrophobic and obese patients, as well as for children, who may be fearful in closed MR scanners. However, these types of scanners provide lower spatial resolution and a lower signal-to-noise ratio (SNR) if compared with the same examination performed at the same time at high field scanners. It is dominantly caused by the low field strength and other factors, such as radiofrequency noise. Therefore, a long measurement time is usually necessary. This research paper is focused on the development of novel probes and preamplifiers for low-field MR scanners to improve SNR, and thus, shorten the measurement time. In this study, we describe the design of a high impedance preamplifier and a high temperature superconductor (HTS) coil. This novel instrumentation was compared with uncooled and cooled copper coils. Improvement in SNR in the case of an HTS coil is reported.

Keywords: Imaging, MRI, low-field tomography, signal-to-noise ratio (SNR), probe, coils, preamplifiers.

1. INTRODUCTION

Signal-to-noise ratio (SNR) is one of the most important parameters for assessing the quality of images obtained by magnetic resonance imaging (MRI) in biomedical applications. Parameters such as spatial resolution and acquisition times are closely related to the SNR [1], [2], [3]. SNR is especially crucial at low fields, as the signal intensity is field-dependent. Although MR systems with high magnetic field strengths are the mainstream scanners these days, low-field systems are still commonly used, as they provide space and accessibility important for claustrophobic and obese patients, for example, as well as for children, who are often fearful in closed MR scanners. Low fields are also useful for modern applications, such as blood oxygenation level dependent contrast MRI (BOLD MRI) [4], [5] and are even more desirable than high fields in some special applications, e.g., hyperpolarized gas lung MRI [6], [7]. In these types of scanners, the SNR is usually increased through signal averaging, which also makes the examination time-demanding.

There are many sources of noise that reduce image quality. Some of the most important of these are sample noise, patient noise, amplifier noise, and internal noise caused by the receiving coil itself. Impact of these noise categories depends on operating frequency and coil size. Based on these parameters we can operate in the sample noise dominant regime or in the coil noise dominant regime. Sample or patient noise are caused by the thermal (Brownian) motion of electrons within the body's conducting tissue. Brownian motion gives rise to random radiofrequency (RF) currents, organized in a number of round-shaped eddy current loops, when the sample is placed into the magnetic field. These current loops produce random changes in magnetic fields, thus inducing noise voltage in the receiving RF coil [8]. This source of noise is important for both high-field MR scanners and low-field scanners. The way to reduce the impact of this source of noise on the MR images is to reduce the receiver bandwidth around the observed Larmor frequency. This can be achieved with a receiving coil of the highest possible quality. The coil quality can be expressed as:

$$Q = \frac{f_0}{\Delta f} \tag{1}$$

where Q is the quality of the receiving coil (resonance circuit), f_0 is the Larmor (observed) frequency, and Δf is the bandwidth.

The second important source of noise is the noise produced by the receiving coil itself, sometimes called Johnson noise. The inherent coil noise can be reduced by cooling down the temperature of the receiving coil [9]. This will also improve the quality of the receiving coil through a bandwidth

DOI: 10.1515/msr-2018-0016

reduction (1). To improve the SNR gain of the receiving coils, it is advantageous to use high temperature superconducting (HTS) materials for the construction of the receiving coils.

The dominant source of Johnson's noise at low frequencies can be the receiver [8]. Furthermore, low-field systems often use a resistive type magnet with a volume-limited homogeneous static magnetic field. For large diameter coils with large objects measured with the coil, the sample exceeds limited volume where B0 homogeneity region is guaranteed. As a consequence, lower SNR is achieved.

The usual cooling method for the winding of HTS coils is immersion into liquid nitrogen. The reason liquid nitrogen is used is that its boiling temperature is 77 K, and therefore, it is easier to handle [8] than liquid helium.

Cooling of the coil causes a decrease in its resistance, together with the noise it causes. Closely linked with the decreased resistance of the coil windings is the improvement in the quality of the coil windings. The quality of the coil windings with serial resistance can be expressed as [10]:

$$Q_U = \frac{\omega_0 L}{R_C} \tag{2}$$

where Q_U is the quality of unloaded coil windings, ω_0 is the Larmor frequency, L is the inductance of the unloaded coil windings, and R_C is the resistance of unloaded coil windings. Improved SNR has been described [11] by the following formula:

$$SNR = \sqrt{\frac{Q_L}{T}} \tag{3}$$

where T is temperature of coil windings, and Q_L is quality of the coil loaded by the sample.

A common measure of probe performance is the ratio r between the Q factor of the unloaded and loaded coil (i.e., sensitivity to loading) described as follows [12]:

$$r = \frac{Q_U}{Q_L} = \frac{R_C + R_{SAMPLE}}{R_C} \tag{4}$$

Another property of the receiving coil that influences the SNR is the coil filling factor, η. This factor is defined as the fraction of RF energy created by the coil, which is stored in the sample volume [11]. The relation between the filling factor and SNR has been described [13] by the following formula:

$$SNR \propto \sqrt{\eta Q_L} \tag{5}$$

For the filling factor maximization, a volume coil is suitable. Due to the thermal isolation needed between the HTS coil and the sample, a slightly reduced filling factor is typical, which limits the potential SNR improvement [11]. Most recent studies have focused on the development of surface receiver coils for low-field scanners [14]. However, volume coils are still of great interest [15].

The aim of this work was to design novel measurement instrumentation, which consists of a volume coil and a preamplifier for low-field MRI systems. Such instrumentation will potentially provide better image quality, with higher SNR for future *in vitro*, as well as *in vivo* measurements, and for testing MR systems performance.

2. SUBJECT & METHODS

A. Design and construction of the HTS coil and pick-up loop

The receiving coil significantly affects the quality of images at low-field MR imaging. Thus, we designed the receiving coil in the form of a single-turn solenoid (volume coil), which has higher sensitivity compared to other single-turn volume receiving coils made of other conductive materials. The HTS receiving coil was built as a single loop (132 mm in diameter) of thin tape of bismuth strontium calcium copper oxide (BSCCO) with a width of 2.6 mm.

When the HTS coil is cooled to 77 K, the HTS windings have low resistance, and the impedance of the parallel resonance circuit is high. The cooled HTS coil had high frequency selectivity; therefore, it had to be precisely tuned to the Larmor frequency of the scanner, in our case, 7.605 MHz. For this purpose, the HTS coil was roughly tuned by fixed, high-quality capacitors and capacitance diodes were added for fine-tuning, as depicted in Fig.1.

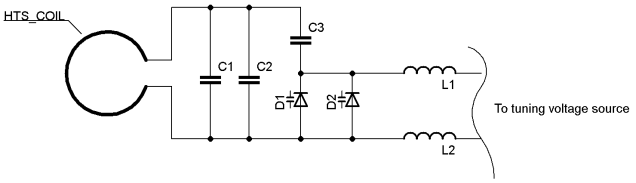

Fig.1. Schematic of HTS coil with fixed capacitors and with added capacitance diodes.

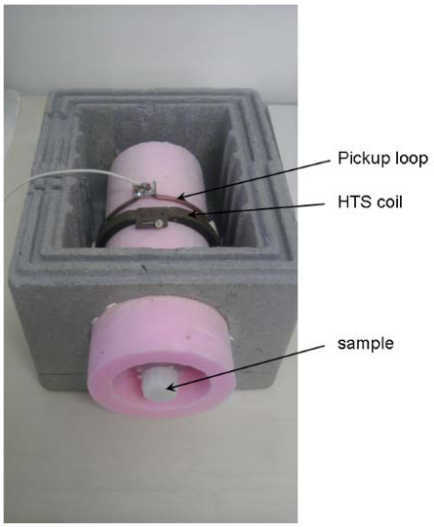

Fig.2. Cryostat with the HTS coil, the pickup loop and the sample. The sample consisted of a bottle with a water solution of 0.648 g/L $NiCl_2$ and 3.214 g/L NaCl.

At this resonance frequency, the skin effect of the material becomes significant; therefore, the thin silver tapes, originally molded to the BSCCO to increase the mechanical strength of the HTS tape, had to be removed by etching. The BSCCO loop modified in this way was placed into the cooling holder and attached there with epoxy glue.

As the HTS resonator has too high impedance at resonance frequency, and its direct connection to the preamplifier would cause an unwanted decrease in the quality of the HTS resonator, a pickup loop had to be used. The pickup loop was made of thin-wall copper tubing.

This loop was directly connected to the preamplifier without tuning. Impedance matching of the receiving HTS coil to the preamplifier was achieved by choosing an appropriate distance between the HTS coil and the pickup loop (Fig.2.).

B. Preamplifier

To achieve satisfactory SNR, the receive probe should be precisely tuned to the Larmor frequency of the MR scanner and matched to the transmission path. The classical approach is to tune the probe by two trimming capacitors that work as a tuning and matching set. This method is usually used when the probe is connected to the preamplifier by a coaxial cable, with a characteristic impedance of 50 Ohm. Another option for connecting the receive coil is to use a preamplifier with a high input impedance. Such a preamplifier can be directly connected as close as possible to the receive coil. In this case, the preamplifier must be constructed without magnetic components and the main magnetic field of the scanner must not interfere with its operation, e.g., amplification. The preamplifier circuit developed for our applications is shown in Fig.3.

This preamplifier can be directly (without coaxial cable) connected to the pickup loop. Given that the preamplifier has a high input impedance of 3.53 kΩ, the distance between the receiving coil (HTS coil) and the pickup loop was set to 1.5 cm, as determined experimentally. The output of this preamplifier was fixed by matching to a transmission line with characteristic impedance of 50 Ohm. In this way, the tuning of the probe was simplified, because it was sufficient to tune the probe to the resonance frequency, as no additional matching was required. The preamplifier was designed for low-field scanners, with the magnetic induction of the main field at 0.1 - 0.18 T. For protection of the signal input of the preamplifier, non-magnetic MELF (Metal Electrode Leadless Faced) diodes MADP-000235-10720T (M/A-COM Inc., Technology Solutions, Lowell, Massachusetts) were used. At the input of the preamplifier, two low-noise and high-linearity Pseudomorphic High Electron Mobility transistor (PHEMT) Field Effect Transistors (FET) transistors, ATF 34143 (Avago Technologies, San Jose, California), were used. The preamplifier was powered by the symmetrical voltage ± 5 V. Frequency selectivity of this preamplifier is given by the connected receiving coil and resonant coupling inside the preamplifier.

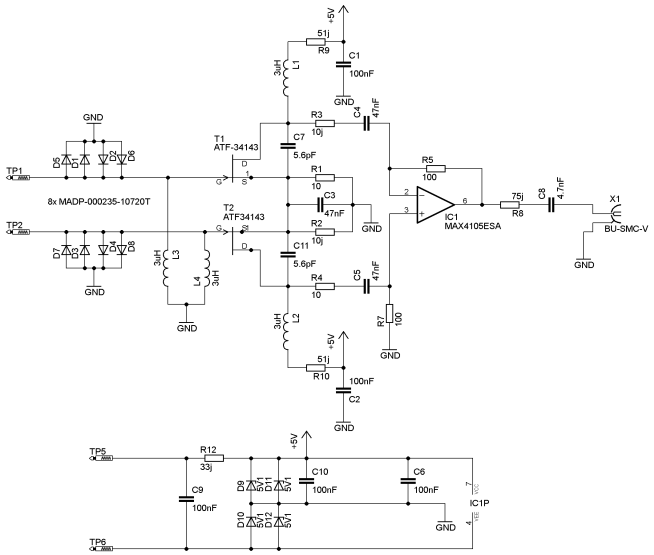

Fig.3. Schematic of high impedance differential preamplifier with power source.

C. Test of coil performance

HTS coil parameters (BW, Q) were measured outside the scanner by an impedance meter, TE 1000 RF (TOMCO Technologies, Norwood, Australia).

For comparison, the properties of the superconducting coil were compared with the properties of a standard copper coil constructed as a single loop of copper tape, 2.6 mm wide and 0.15 mm thick. The loop had the same diameter as the HTS coil, for direct comparison [15]. Properties of this copper coil were evaluated with and without nitrogen cooling.

The coils were also compared in terms of imaging performance, where the SNR was calculated for quantitative comparison. Both coils, HTS and copper, were placed into the same cryostat during imaging. The SNR was calculated (6) as the ratio between the mean signal intensity of a phantom image and the standard deviation of the background noise. A bottle phantom of 8 cm in diameter filled with a liquid solution containing 0.648 g/L $NiCl_2$ and 3.214 g/L NaCl in distilled water to mimic the body loading was used.

$$SNR = \frac{S_{mean}}{N_{S.D.}} \tag{6}$$

where S_{mean} is the mean value of the signal and $N_{S.D.}$ is the standard deviation of the noise background.

The phantom images were obtained by all three coils, using the developed preamplifier, on a 0.18 T MR scanner, the E-scan Opera (ESAOTE, Genoa, Italy). Equally set T_1-weighted spin echo images were obtained, with TE =18 ms, TR = 500 ms, an acquisition matrix 256x256, number of acquisitions (NumAcq) = 1, and a slice thickness of 5 mm. The SNR was calculated from the signal intensity taken from an area of 1x1 cm in the center of the imaged phantom.

3. RESULTS

The images in Fig.6. were obtained to compare the impact of different coils on the image quality. The quality of the obtained images was based on the calculated SNR value.

The quality factors of HTS and copper coils were measured and compared. The detailed values of the coil properties are summarized in Table 1. A decrease in frequency bandwidth with increased quality of the coil was detected, which was in agreement with the expectations.

Table 1. Parameters of used coils.

Coil	State	Bandwidth [kHz]	Quality of loaded receiving coil	Quality of unloaded receiving coil	Filing factor [%]
copper	uncooled	118	64.5	64.5	58
copper	cooled	41	185	186	58
HTS	cooled	23	330	387.47	58

Fig.6. shows a large difference in image quality, if cooled and uncooled copper coils, respectively, were used for acquisition. The differences between the cooled copper coil and the HTS coil were not obvious to the naked eye, but the measured SNR was higher for the HTS coil.

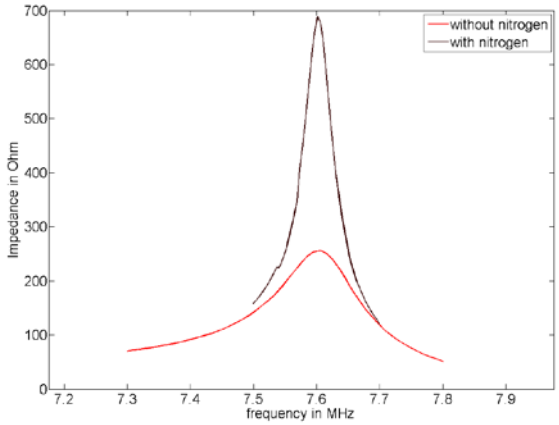

a)

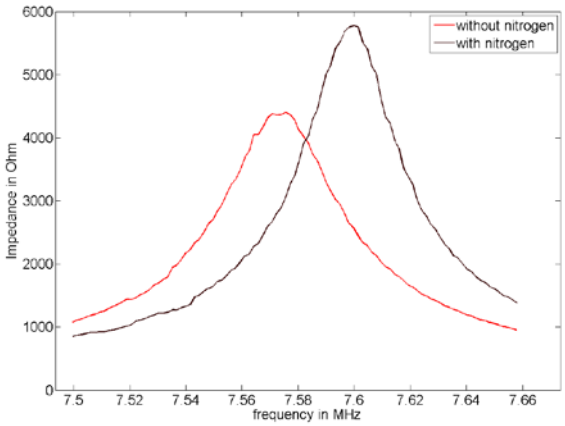

b)

Fig.4. Impedance characteristic of a) copper coil and b) an HTS coil.

The SNR of the room-temperature copper coil was 14.53, while the SNR of the cooled copper coil was 38.75, equal to a 2.67 times greater SNR in the cooled state. For the HTS coil, the achieved SNR was 52.9, which is 3.6 times higher and 1.4 times higher than the SNR of the room-temperature and cooled copper coils, respectively. The loaded winding resistance, R_C, of both coils decreased after cooling with liquid nitrogen, which caused an increased impedance of the receiving resonance circuit (Fig.4.), and a corresponding increase in the quality of the coils (Table 1.), as described by equation (2). The induction of the HTS coil was changed after cooling, unlike the copper coil, as shown in Fig.4. The improvement in SNR can be calculated from equation (7), as a ratio of SNRs at room temperature and at the working temperature of liquid nitrogen, 77 K. Theoretically, the improvement in SNR (for the tested copper coil at 296.15 K room temperature) can be calculated as follows:

$$\frac{SNR_{77\,K}}{SNR_{296.15\,K}} = \sqrt{\frac{Q_{77\,K} \cdot 296.15}{Q_{296.15\,K} \cdot 77}} = 3.32 \qquad (7)$$

4. DISCUSSION / CONCLUSIONS

Novel measurement instrumentation, with a high impedance preamplifier and a superconducting coil, was developed and tested on a clinical low-field scanner.

The preamplifier itself is broad-banded, as shown by amplitude frequency characteristic in Fig.5.

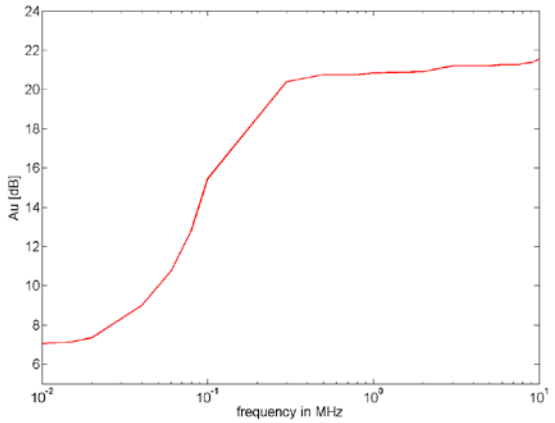

Fig.5. Amplitude frequency characteristic of preamplifier, measured without receiving coil.

Around the required frequency, which is 7.605 MHz (the Larmor frequency of hydrogen nucleus on a scanner with a main field of 0.18 T, which was the scanner we used), the gain of this designed and constructed preamplifier was 21.26 dB and the noise figure was 2.2 dB. The constructed preamplifier had acceptable parameters, which were independent of the magnetic field strength. The amplifier gain was independent relative to the B_0 field. It was identical inside and outside the main static magnetic field B_0. The placement of the preamplifier into the B_0 static magnetic field had no effect on the image quality.

For comparison, two types of receiving coils were constructed, one of copper and one of BSCCO tapes. These coils were of the same circular geometry: 2.6 mm wide and 132 mm in diameter. The quality of the acquired images was evaluated on the basis of the achieved SNR. A relatively high change in SNR is obvious in Fig.6.a) and Fig.6.b). From the obtained images, it was calculated that the SNR improved 2.67 times after the cooper coil was cooled (Fig.6.b). The theoretically calculated improvement in SNR was posited to be slightly higher (3.32) than the experimentally measured value. This was probably caused by the interference of the main static magnetic field of the tomograph with the impedance meter probe. Further improvement in SNR was achieved by using the HTS coil. The measured SNR was 3.64 times higher than the SNR for the uncooled copper coil. Compared to the cooled copper coil, SNR was further improved by a factor of 1.37.

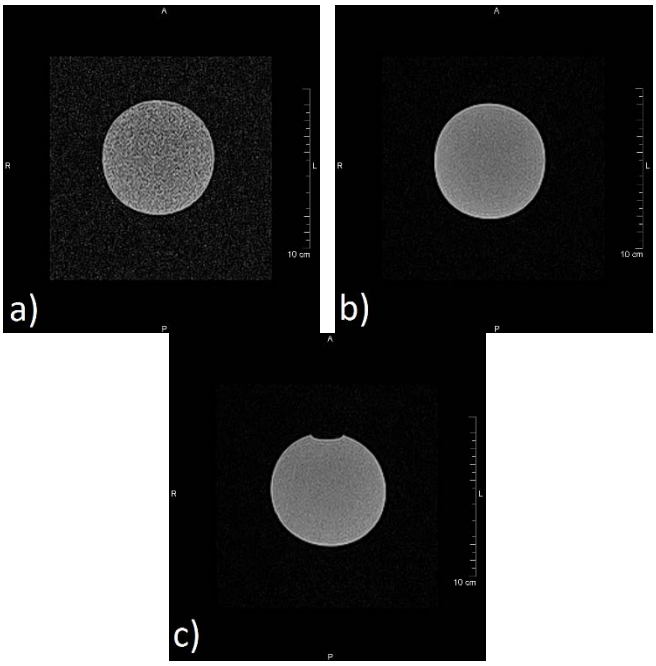

Fig.6. Images of the same slice of a water phantom: a) image obtained by uncooled copper coil, with the SNR = 14.53, b) image obtained by a cooled copper coil, with the SNR = 38.75, c) image obtained with an HTS coil, with the SNR = 52.9. An air bubble is visible in figure c, which had moved into this slice, causing an artifact, but this did not compromise the SNR evaluation.

This improvement was not obvious from a direct visual inspection of the image; however, it was clearly shown by the SNR calculations. While this may make it seem that the improvement in SNR for the HTS coil compared to the cooled copper coil was small or not significant, it should be noted that the coils were designed as simple, single-turn coils. Therefore, it could be anticipated that the construction of more complex receiving coils, such as birdcage, quadrature coils, and phased array coils, would lead to a significantly increased difference in SNR, if comparing HTS to cooled copper coils.

As described in [14], higher SNR could also be achieved using an HTS coil designed as a surface coil, but in a small area near the coil. These types of coils would find an application in MR microscopy [10], [17] or spectroscopy on high-field scanners. Cryogenic MR receiving coils can provide spatial resolution well below 100 μm in each direction of space, with acquisition times of a few minutes [18]. One of the disadvantages that prevents the wider application of cryogenic coils is the fact that they cannot be placed as close to the sample as an uncooled copper coil, because of thickness of thermal insulation. This reduces the SNR gain for cryogenic coils. However, currently, modern thermal isolation materials are available that are thin and provide a high thermal resistance at the same time. One example of such a material is aerogel.

In another study [19], an HTS surface coil was developed, with a diameter of 50 mm, designed for a high-field (1.5 T) scanner, and built from Bi-2223 material ($Bi_2Sr_2Ca_2Cu_3O_6$). Its critical temperature was 110 K. The investigators compared the HTS coil and cooled copper coil and reported an improvement in SNR by a factor of 1.11. When they compared an HTS coil and an uncooled copper coil, SNR improved by a factor of 1.36. These SNR improvements are significantly lower compared to our results. This was probably caused by the fact that the inherent noise of the receiving coil in a high-field (1.5 T) scanner does not contribute to the overall noise in the measured image as much as it does for low-field scanners. In a low-field study by Ma et al. [14], an HTS surface coil was developed and tested on a 0.2 T scanner. The measured SNR of an image acquired with this HTS coil was 1.4 times higher compared to an image measured with a cooled copper coil. This is in good agreement with our study, where we reported an SNR improvement by a factor of 1.37 with a volume coil constructed for low-field imaging.

Our study has some limitations. The width of our HTS coil was relatively small. By using wider HTS strips, the coil quality could be improved. However, our coil was compared with geometrically identical copper coils; thus, the improvement in the SNR is undeniable. The large distance between the coil and the sample also played an important role in the resultant SNR. This distance was determined by the isolation material used, which separated the insides of the cryostat at a temperature of 77 K from the area with the sample at a temperature of 296.15 K. Aerogel would seem to be a more suitable (thinner) material for thermal isolation, rather than the styrodur used. Aerogel would save about two-thirds of the insulation thickness and its thermal conductivity is approximately 0.017 $W.m^{-1}.K^{-1}$ instead of the 0.032 $W.m^{-1}.K^{-1}$ of styrodur. The use of aerogel as an isolation material could further increase the SNR gain.

Future steps would be the design of a more suitable cryostat, with closed circulation of nitrogen and better and thinner thermal isolation. Currently, different types of HTS materials, such as Hg-1223 ($HgBa_2Ca_2Cu_3O_8$), whose critical temperature is 134 K, are available. These materials need to be studied in more detail. Our next step is to test a complex receiving coil design using wider HTS tape.

5. Conclusion

We designed, analyzed, and experimentally verified the properties of cooled and uncooled copper and HTS receiving coils for low-field MRI as well as the influence of these coils on image quality. We demonstrated that a receiving coil built from HTS material with a dedicated preamplifier can significantly improve the SNR of the obtained image at low magnetic fields, thus time-intensive signal averaging is reduced by about a factor of 2.

Based on the results obtained, we can conclude that the HTS materials appear to be suitable for the construction of complex receiving coils, such as birdcage, quadrature coils, and phased array coils, for low-field scanners and will have applications in MR microscopy at high-field scanners as well.

Acknowledgment

This work was supported by the Slovak Scientific Grant Agency VEGA 2/0001/17 and by Slovak Research and Development Agency APVV-15-0029.

References

[1] Hoult, D.I., Richards, R.E. (1976). The signal-to-noise ratio of the nuclear magnetic resonance experiment. *Journal of Magnetic Resonance*, 24 (1), 71-85.

[2] Hoult, D.I., Lauterbur, P.C. (1979). The sensitivity of the zeugmatographic experiment involving human samples. *Journal of Magnetic Resonance*, 34 (2), 425-433.

[3] Ginefri, J.-Ch., Poirier-Quinot, M., Girard, O., Darrasse, L. (2007). Technical aspects: Development, manufacture and installation of a cryo-cooled HTS coil system for high-resolution in-vivo imaging of the mouse at 1.5 T. *Methods*, 43 (1), 54-67.

[4] Schulder, M., Azmi, H., Biswal, B. (2003). Functional magnetic resonance imaging in a low-field intraoperative scanner. *Stereotactic and Functional Neurosurgery*, 80 (1-4), 125-131.

[5] Valkovič, L., Juráš, V., Gogola, D., Frollo, I. (2012). The early effect of alcohol and caffeine on a BOLD signal measured in human hand at low-field MRI. *Applied Magnetic Resonance*, 42 (4), 463-471.

[6] Parra-Robles, J., Cross, A.R., Santyr, G.E. (2005). Erratum: "Theoretical signal-to-noise ratio and spatial resolution dependence on the magnetic field strength for hyperpolarized noble gas magnetic resonance imaging of human lungs" [Med. Phys. 32, 221–229 (2005)]. *Medical Physics*, 33 (5), 1525-1526.

[7] Vojtíšek, L., Frollo, I., Valkovič, L., Gogola, D., Juráš, V. (2011). Phased array receiving coils for low field lungs MRI: Design and optimization. *Measurement Science Review*, 11 (2), 61-66.

[8] Redpath, T.W. (1998). Signal-to-noise ratio in MRI. *The British Journal of Radiology*, 71, 704-707.

[9] Lee, H.-L., Lin, I.-T., Chen, J.-H., Horng, H.-E., Yang, H-C. (2005). High-T_c superconducting receiving coils for nuclear magnetic resonance imaging. *IEEE Transactions on Applied Superconductivity*, 15 (2), 1326-1329.

[10] Miller, J.R., Hurlston, S.E., Ma, Q.Y., Face, D.W., Kountz, D.J., MacFall, J.R., Hedlund, L.W., Johnson, G.A. (1999). Performance of a high-temperature superconducting probe for in vivo microscopy at 2.0 T. *Magnetic Resonance in Medicine*, 41 (1), 72-79.

[11] Cheng, M.-Ch. (2004). *High temperature superconductor tape RF volume coil for MRI systems*. Thesis, The University of Hong Kong.

[12] Giovannetti, G., Francesconi, R., Landini, L., Santarelli, M.F., Positano, V., Viti, V., Benassi, A. (2004). Conductor geometry and capacitor quality for performance optimization of low-frequency birdcage coils. *Concepts in Magnetic Resonance B*, 20B (1), 9-16.

[13] Mispelter, J., Lupu, M., Briguet, A. (2006). *NMR Probeheads: For Biophysical and Biomedical Experiments*, 1st Edition. Imperial College, 596.

[14] Ma, Q.Y., Chan, K.C., Kacher, D.F., Gao, E., Chow, M.S., Wong, K.K., Xu, H., Yang, E.S., Young, G.S., Miller, J.R., Jolesz, F.A. (2003). Superconducting RF coils for clinical MR imaging at low field. *Academic Radiology*, 10 (9), 978-987.

[15] Nouls, J.C., Izenson, M.G., Greeley, H.P., Johnson, G.A. (2008). Design of a superconducting volume coil for magnetic resonance microscopy of the mouse brain. *Journal of Magnetic Resonance*, 191 (2), 231-238.

[16] Cheng, M.C., Lee, K.H., Chan, K.C., Wong, K.K., Yang, E.S. (2003). HTS tape RF coil for low field MRI. In *Proceedings of the International Society for Magnetic Resonance in Medicine*, Toronto, Ontario, Canada, 2359.

[17] Ginefri, J.-Ch., Darrasse, L., Crozat, P. (2001). High-temperature superconducting surface coil for in vivo microimaging of the human skin. *Magnetic Resonance in Medicine*, 45 (3), 376-382.

[18] Darrasse, L., Ginefri, J.-Ch. (2003). Perspectives with cryogenic RF probes in biomedical MRI. *Biochimie*, 85 (9), 915-937.

[19] Yuan, J., Shen, G.X., Wang, Ch., Wu, B., Qu, P. (2004). Use of Bi-2223 multifilamentary tapes as RF coils for 1.5 T MRI application. *Physica C*, 415 (4), 189-196.

Received January 16, 2018.
Accepted April 25, 2018.

MEASUREMENT SCIENCE REVIEW, **18**, (2018), No. 3, 113-122

DE GRUYTER OPEN

MEASUREMENT SCIENCE REVIEW

Journal homepage: http://www.degruyter.com/view/j/msr

ISSN 1335-8871

Dimensional and Geometrical Errors in Vacuum Thermoforming Products: An Approach to Modeling and Optimization by Multiple Response Optimization

W. O. Leite[1], J. C. Campos Rubio[2], F. Mata[3], I. Hanafi[4], A. Carrasco[5]

[1] *Campus Betim, Departamento de Mecânica, Instituto Federal de Educação, Ciência e Tecnologia de Minas Gerias, Rua Itaguaçu, No. 595 - São Caetano, 32677-780, Betim, Brasil,* wanderson.leite@ifmg.edu.br

[2]*Escola de Engenharia, Departamento de Engenharia Mecânica,Universidade Federal de Minas Gerais, Av. Pres. Antônio Carlos, No.6627 - Pampulha, 31270-901, Belo Horizonte, Brasil.*

[3]*Escuela de Ingeniería Minera e Industrial de Almadén, Departamento Mecánica Aplicada e Ingeniería de Proyectos, Universidad de Castilla-La Mancha, Plaza Manuel Meca No.1,13400, Almadén, España.*

[4]*Ecole National des Sciences Appliquées d' Al Hoceima (ENSAH), Department of Civil and Environmental Engineering, BP. 03, Ajdir, Al Hoceima, Morocco.*

[5]*Escuela de Ingeniería Minera e Industrial de Almadén, Departamento de Filología Moderna, Universidad de Castilla-La Mancha, Plaza Manuel Meca No.1,13400, Almadén, España.*

In the vacuum thermoforming process, the product deviations depend on several parameters of the system, which make the analysis, the computational modeling, and the optimization of errors a multi-variable process with conflicting objectives. In this sense, the aim of this work was to study the dimensional and geometrical errors as well as the optimization (minimization) of these errors in one typical vacuum thermoforming product made of polystyrene (PS). In particular, it was intended to predict and minimize errors in a range of ideal tolerances using Multiple Response Optimization (*MRO*) Models. Thus, through the fractional factorial design (2^{k-p}), initial experimental tests were performed using proposed measurement procedures, and Analysis of Variance being the data analysis is discussed. Following that, the *MRO* models were implemented which were also validated to represent the sample data. Through this analysis of the results, it can be concluded that the regression models of errors are not linear functions, hence, the developed models are valid for the studied process, and finally that the validation results proved the efficiency of *MOR* models developed, but these models will not be able to generalize to new situations in a range far from the values studied.

Keywords: Dimensional and geometrical errors, vacuum thermoforming process, multiple response optimization, plastics processing.

1. INTRODUCTION

Thermoforming is a generic term for a set of thermoplastic manufacturing processes which allow the production of thin wall plastic parts from flat sheets or plastic films, such as vacuum thermoforming, also known as vacuum forming, drape forming technique, thermoforming with the use of air-slip forming, and other little-used techniques such as billow or free bubble forming, mechanical bending, matched-mold forming, and twin-sheet forming, which are the earliest and simplest methods of thermoforming [1], [2].

In this context, the vacuum forming technique is defined by [2]-[4] as the process where the vacuum force obtained by the negative atmospheric pressure is used to force a preheated sheet against the "cold" surface of the mold, which takes on its shape. Specifically, this is the forming technique and/or stretching where a sheet of thermoplastic material is preheated by a heating system (Fig.1.a), Fig.1.b)) and forced against the mold surface (positive or negative) by means of the negative vacuum pressure produced in the space between the mold and sheet (Fig.1.d1)), by mold suction holes and a vacuum pump which "sucks" the air from the space and "pulls" the sheet against the surface of the mold (Fig.1.d1)), transferring it, after cooling (Fig.1.e)) and removing excess material to shape it (Fig.1.f)), [4], [5]. The typical sequence of this technique is presented in Fig.1. [6].

However, according to [7], [8], there are still a number of challenges to be overcome in this process, caused by the conflict of objectives between the quality aspects and the adjustments of the process control variables. The evaluation of the performance of the system is usually dependent on many processing variables such as environmental manufacturing characteristics, equipment characteristics,

DOI: 10.1515/msr-2018-0017

stretch speed, plug characteristics, temperature of heating, and cooling system [1], [9], [10]. Therefore, for [7], [8], [11] it is necessary to understand the complex and multi-variable process, with non-linear characteristics and conflicting objectives, in order to optimize the product quality characteristics and reduce errors before molding the part.

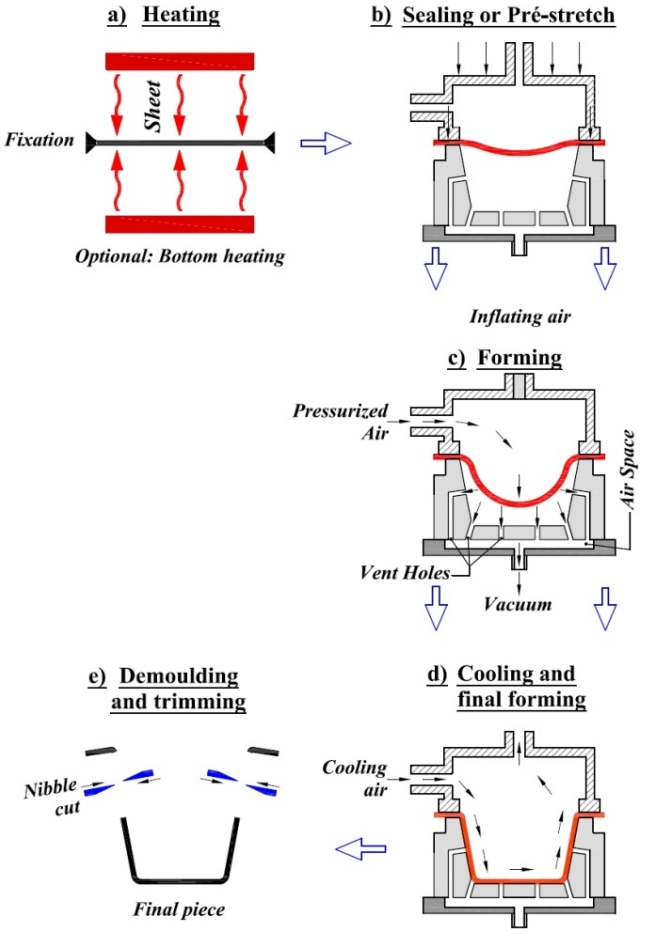

Fig.1. Schematic of basic vacuum thermoforming.

Several authors have developed work with the objective of modelling and predicting the quality of the final product of the vacuum thermoforming process, [12] using computational optimization techniques, Finite Element Method (FEM), Artificial Neural Network (ANN), and [7], [8] statistical models, aiming to predict and to optimize the quality characteristics. We still have the works of [10], and others focusing on the development of an elastic-plastic model for thickness analysis [2], [13]. Leite *et al.* describe the application of a methodology based on Artificial Neural Network models with objective function [11], the model has processing parameters as inputs and the product errors as outputs. References [6], [14]-[17] concentrated their studies on aspects of mold geometry and process parameters to verify their influence on the distribution of product thickness, [4], [18] have developed a methodology for optimization of production technologies with the product design. Martin *et al.* have studied the instrumentation and control of thermoforming equipment in real-time analysis with the control of multiple variables [19]. Other researchers have focused on modeling, simulation and prediction of sheet temperature and optimization of the heating system by different methods and techniques [20]-[22].

However, in complex manufacturing processes such as this, [23]-[25] suggest that the traditional approaches to process control fail to understand all aspects of process control or existing subsystems. Thus, researchers are using Multiple Response Optimizations (*MRO*) to model systems with multiple input and response variables, in order to minimize or maximize all responses based on an objective function. With a multi-criteria optimization problem involving more than one objective function to be optimized simultaneously, usually, the objective functions are in conflict with, or compete with each other, thus, the possible optimal solution functions do not allow the minimization of all objectives simultaneously. Researchers present several approaches and methods to optimize problems of multiple objectives [26], some of them reported by [27], [28].

One of the widely adopted techniques for *MOR* models uses Multiple Linear Regression Models (*MLR* models) to describe the relationship between a response and its regressor variables (process parameters), and also to estimate the response [29]-[31]. These models described by Montgomery [32] are linear regression equations that contain more than one independent variable or regressor and a dependent or response variable, that are related to *k* regressors or variables of input. Thus, these models need to be developed for each of the response variables for the modeling of an *MLR* algorithm [33]. The developed models are converted into a system that combines the n individual equations and an objective function through the programming of a multiple response optimization algorithm [18], [32]. Thus, the objective of this algorithm is to find a satisfactory solution or several possible configurations of the input variables that simultaneously offer the best performance for the multiple objectives of the n models [33], using solution space of input variables [29]. These equations can be solved by several mathematical methods of solving systems of linear equations or software [29].

First, the objective of this work was to study the dimensional and geometrical errors and the optimization (minimization) of these errors in one typical vacuum thermoforming product. For this purpose, the manufacturing parameters (factors) were studied statistically to determine their influence on the deviations of the product (response variables), and then, the Multiple Response Optimization Method that uses Multiple Linear Regression models to describe the relationships of the variables studied, (simultaneously) was used to simultaneously minimize the partial errors. A validation test was performed to evaluate the predictive capacity of the models and efficiency of the methodology studied. Finally, this study allowed us to identify the main significant factors, and also to develop models and algorithms that estimate and minimize errors of vacuum thermoforming parts.

2. EXPERIMENTAL WORK

2.1. Material and equipment

In this work, 2.0 x 2.5 m of white laminated polystyrene (PS) sheets with a thickness of 1.0 mm were used to manufacture the parts. The plates were cut into 300 x 360 mm sheets, cleaned with water and neutral liquid soap (pH), and then dried and wrapped in plastic film packages previously heated at 50°C and maintained for two hours.

For the manufacturing of the mold, considering the inherent aspects of the manufacturing process and the volume contraction of the product of 0.5 % [1], [34], Medium Density Fiberboard (MDF) plates were used as the raw material. The three-dimensional (3D) design of the model was developed using Computer-Aided Design (CAD, SolidWorks® 2008) software, which was integrated with Computer-Aided Manufacturing (CAM, Edge CAM® 2010) software. The mold was machined in a Computer Numeric Control machine (CNC, Discovery 560 ROMITM Machining Center), and subsequently, the vacuum holes and the final finish were performed. Finally, we performed the Computer-Aided Inspection (CAI) of the mold in a Coordinate Measuring Machine 3D (CMM 3D, Micro-Hite 3D TESATM with Reflex Software) to determine the dimensional and geometric deviations present in the mold.

A semi-automated vacuum thermoforming machine was developed and automated by the researchers. This equipment has the capacity to work with plates of thickness of 0.1 to 3.0 mm, a useful area of 280 x 340 mm, displacement of the mold (*z* axis) of up to 150 mm, vacuum pumps of 160 mbar with motors of 1.0 CV, infrared heating systems composed of two resistors of 750 W and 1,000 W, movement by pneumatic systems and acquisition of temperature data by "K" thermocouples and non-contact infrared. The system is programmable through a commercial Personal Computer (PC) integrated with microcontroller board (Arduíno UNO Revision 3).

2.2. Parameters and measurement procedure

There is no consensus among authors [4], [5], [7], [8] about the measurement parameters of control and quality in the vacuum thermoforming process and still, [1], [4], [9] there is no specific measurement procedure or equipment to be used. As a result, they were defined and developed to measure the errors of the piece. The procedures, scales, measurement process and tolerances are described in the following paragraphs.

For measurement errors, 3D MMC was used carrying a 4 mm diameter solid probe, calibrated with an error of ± 0.004 mm and CAI software. The reference values for dimensions were calculated, based on the final dimensions of the mold. Also, according to [3], [9], a deviation of ± 1 % for linear dimension and ± 50 % for flatness on surfaces are acceptable, and as a reference, the values calculated for dimensions were adopted as the general criteria for acceptance of sample dimensions. Fig.2. presents the geometry of the standard product, where dimensions and parameters to be measured in the samples are represented.

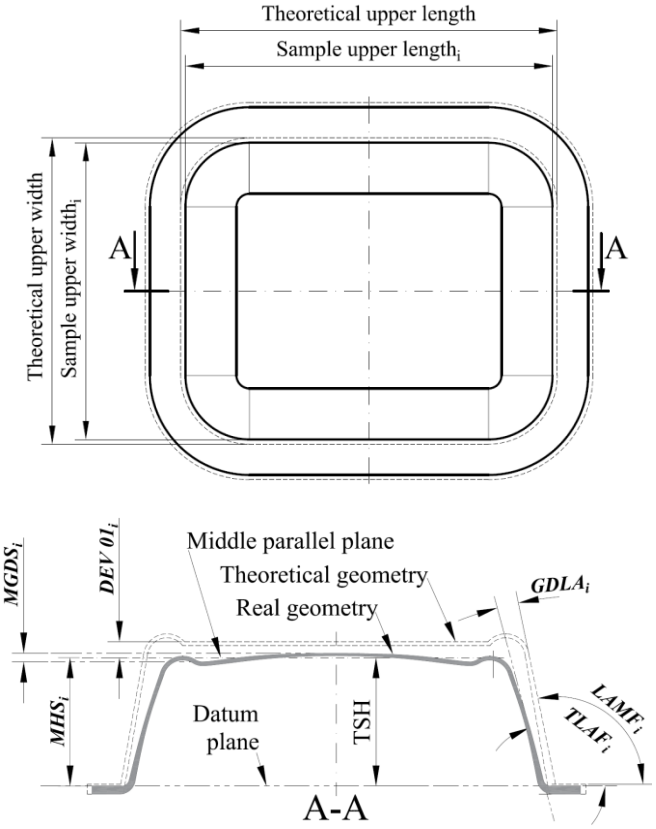

Fig.2. Product standard: dimensions on piece or dimensional deviations parameters.

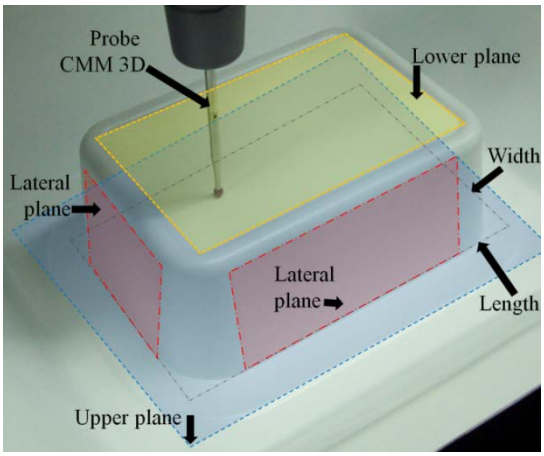

Fig.3. Measurement: Planes and references in the sample.

So, the Dimensional Deviation Height (DDH_i) or *DEV 01* was defined thus:

$$DDH_i = (MHS_i - TSH\ ) == DEV01_i = (MHS_i - 57.92) \quad (1)$$

where *i* is the index of the analyzed sample and *TSH* is the Theoretical Sample Height (57.92 mm). The MHS_i is the Measured Height in the Sample, calculated by the distance between two parallel planes formed by the upper and lower parts of the sample (Fig.2. and Fig.3.).

To determine the planes, 8 points were collected in each region using the 3D MMC (Fig.3.) and via CAI software the perpendicular distance between the planes was calculated. A negative (-) mean value indicates that the height is less than the ideal and a positive mean value (+) that it is greater than the ideal.

The Deviation of the Diagonal Length (DDL_i) or *DEV 02* is calculated by the difference between the values of the $MLDS_i$ and the value of the *TDL*, being:

$$DDL_i = (MLDS_i - TDL\ ) \tag{2}$$

where, $MLDS_i$ is the Measured Length of the Diagonal in the Sample or *DEV 02*, which in this work was defined as the quadratic relation of the lateral distances of the upper end of the sample (length and width) (Fig.2. and Fig.3.) and *TDL* is Theoretical Diagonal Length of the Sample = 207.97 mm, so:

$$DDL_i = DEV02_i(\sqrt{(width_i)^2 + (length_i)^2 - 207.97}) \tag{3}$$

To determine lateral distances, 5 points were collected along each side of the samples (Fig.3.), and later, via CAI, the distances between sides were calculated. A negative (-) mean value indicates that the length is smaller than the ideal and a positive mean value that it is greater than the ideal. Also, *TDL* is the Theoretical Diagonal Length of the Sample (208.0 mm).

The *DEV 03* or Geometric Deviation of Side Angles ($GDSA_i$), in this study, is expressed as:

$$\begin{aligned} GDSA_i &= 1/z \sum_{J-1}^{Z} GDLA_i == ... \\ DEV04_i &= 1/4 \sum_{J-1}^{4} (LAMF_S - TLAF_S\ ) \end{aligned} \tag{4}$$

where *z* is the number of sides and *s* the evaluated face. The *GDLA* is the difference between the Lateral Angle Measured on the Face of sample *i* ($LAMF_i$) and the Theoretic Lateral Angle of the Face (*TLAF*), for *s* = 1 ... 4, respectively, 95.93º, 95.93º, 96.02º and 96.06º. To determine each *ALMF*s, 09 points were collected on the surface to design the plan of control (lateral planes, Fig.2. and Fig.3.). The *GDLA*i was calculated, using CAI software, by the difference between the planes of the angles.

The Geometric Deviation of Flatness (GD_i) or *DEV 04*, that will have a zero value (0) for an ideal surface or positive values, was calculated as:

$$GD_i = (MGDS_i - TGDS\ ) == DEV03_i = (MGDS_i - 0.11) \tag{5}$$

where $MGDS_i$ is the Measurement Geometric Deviation of the *i-th* Sample, calculated by measuring 09 points on the surface of sample bottom (lower plane, Fig.2. and Fig.3.). Later, using CAI software, the distance between the two boundary planes of measured surface was calculated. Also, this procedure was used to calculate the Theoretical Geometric Deviation of the Sample (*TGDS*), which is 0.11 mm.

2.3. Analysis method

The Analysis of Variance (ANOVA) method has been performed to determine the importance of the process input parameters. The ANOVA is a set of statistical methods used to analyze data and to investigate implication of the main effects and interactions in the response variable. Moreover, it provides enough data to compare the parameter levels and the significances. [35].

Also, to estimate the response variable and evaluate the first-order models in A, C, ..., E, along with the AC, ..., AE interaction, the Fractional Factorial Designs [35] technique was used. For this, the coefficients of multiple linear regression models (*MLR*) were calculated. The *MLR* is the regression model that contains more than one independent variable *x*, that is, the response variable *Y*, is related to *k* input variables [29], so:

$$Y = \beta_0 + \beta_1 x_1 + \beta_2 x_2 + \ldots + \beta_j x_k + \ldots + \beta_j x_1 x_2 + \ldots + \beta_j x_k x_{k+1} + \varepsilon \tag{6}$$

Finally, Multiple Response Optimization Models (*MRO* models) were developed [29], [32]. For this, the coefficients of *MLR* and statistical analysis data are used for computational modeling of the *MLR* models for each type of response variable. Afterwards, the *MRO* algorithms are developed with the *MLR* models, in order to generalize and estimate minimum error values and generate a list of possible optimal solutions. The script codes are programmed in the MATLAB® numerical analysis and programming software, with the techniques of analysis described.

2.4. Experimental study and analysis of data

In this research, we used the parameters (factors) described by [3] and compatible with the geometry of sample and equipment, namely: A. Heating Time (in seconds - s), B. Electric heating power (in percentage - %), C. Mold actuator power (in Bar and cm/s), D. Vacuum time (s), and E. Vacuum Pressure (in millibar - mbar). Table 1. shows the levels - high and low and values of parameters. For these selected values, test trials were performed to determine the operating value (center points) and limits with which the samples could be manufactured [7].

Table 1. Factors and levels selected for the main experiments.

Level	**Factors**				
	***A* [s]**	***B* [%]**	***C* [bar and cm/s]**	***D* [s]**	***E* [mbar]**
1 (-1)	80	3.4 (100%)	18.4 (100%)	7.2	10
2 (+1)	90	4.0 (85%)	21.6 (85%)	9.0	15

The experiment consisted of 17 treatment combinations according to the planning Fractional Factorial Design $2_V^{5-1}2$ with one center point [35]. For each treatment, two (2) runs were performed in a random sequence being that, 01 sample and 01 repetitions were manufactured in the same run, totaling 68 runs (4 samples per treatment combinations). The 68 samples of PS were produced and then cooled completely

in an air-conditioned room at 22ºC with 60 % humidity. Then, to quantify the linear and geometric errors of the parts, the inspection methods described in the previous chapter were applied using CMM 3D and the results found were tabulated. Table 2. shows the types of deviations and respective mean values of 34 samples. It is observed that the data *vs.* type of deviation are well distributed, except for only two (02) points for *DEV 03*, respectively, samples 26 and 31 (outliers in data: values below $Q1 - 1.5 \times IQR$ or above $Q3 + 1.5 \times IQR$, respectively for *DEV* 03 the interval from -0.415 to 1.345. Where: *IQR* is the Interquartile Range, *Q1* first quartile and *Q2* is third quartile.).

Table 2. Experimental main results.

Order test	**Responses (values)**			
	DEV 01[a] ***[mm]***	***DEV 02***[a] ***[mm]***	***DEV 03***[a] ***[º]***	***DEV 04***[a] ***[mm]***
1	-0.122	-0.238	0.358	0.269
2	-0.628	-0.217	1.050	0.476
3	-0.464	-0.305	0.238	0.113
4	-0.463	-0.248	0.213	0.204
5	-0.467	-0.231	0.294	0.082
6	-1.565	-0.160	0.910	0.539
7	-0.229	-0.294	0.270	0.218
8	-0.490	-0.288	0.204	0.302
9	-0.323	-0.198	0.418	0.410
10	-0.943	-0.277	0.281	0.398
11	-0.463	-0.383	0.288	0.107
12	-1.000	-0.241	0.451	0.416
13	-0.989	-0.217	0.301	0.128
14	-0.328	-0.377	0.265	0.239
15	-0.597	-0.423	0.110	0.235
16	-0.492	-0.473	0.279	0.292
17	-0.563	-0.227	1.150	0.476
18	-1.431	-0.254	0.955	0.462
19	-0.645	-0.328	0.502	0.433
20	-0.576	-0.460	0.213	0.232
21	-1.234	-0.245	0.805	0.442
22	-0.794	-0.301	0.457	0.322
23	-1.022	-0.310	1.106	0.442
24	-0.639	-0.366	0.531	0.242
25	-0.757	-0.297	0.230	0.043
26	-1.306	-0.248	1.551[b]	0.628
27	-0.785	-0.317	0.505	0.285
28	-0.419	-0.358	0.265	0.223
29	-0.692	-0.407	0.238	0.181
30	-0.792	-0.466	0.213	0.164
31	-1.294	-0.279	1.532[b]	0.642
32	-0.824	-0.455	0.062	0.221
33	-1.096	-0.288	0.320	0.477
34	-0.832	-0.430	0.736	0.231

[a] Mean average value for 02 pieces; [b] Outlier

The ANOVA assumptions were verified and validated using analysis of normality assumption (Anderson-Darling), assumption of homogeneity of variances (plot of residuals versus fitted values) and independence assumption (plot of residuals in time sequence) processed by MiniTab 16® software, none showed abnormal values. The ANOVA results for deviations versus the factors studied are summarized in Table 3., or *F*-test table, with a confidence level of 95 % ($\alpha = 0.05$), and the critical test value for the *F* distribution $f_{0,05;1;17} = 4.45$.

Table 3. ANOVA summary table, results for the deviation analysis vs. factors in main experiments.

Factor	**Responses**							
	DEV 01		***DEV 02***		***DEV 03***		***DEV 04***	
	$F_{(0)}$	*p-valor*	$F_{(0)}$	*p-valor*	$F_{(0)}$	*p-valor*	$F_{(0)}$	*p-valor*
A	10.2	0.005	89.7	0.000	77.72	0.000	0.42	0.542
B	37.0	0.000	82.6	0.000	86.23	0.000	22.5	0.000
C	0.30	0.592	4.6	0.046	8.93	0.008	1.44	0.246
D	0.98	0.336	6.43	0.021	56.03	0.000	0.02	0.899
E	0.08	0.776	4.50	0.049	1.36	0.259	0.34	0.567
A*B	1.92	0.184	52.1	0.000	43.81	0.000	3.91	0.065
A*C	4.86	0.042	2.73	0.117	6.24	0.023	0.27	0.612
A*D	6.13	0.024	1.29	0.271	5.58	0.030	2.27	0.150
A*E	1.87	0.189	2.63	0.123	2.04	0.171	0.29	0.596
B*C	5.66	0.029	0.01	0.943	0.42	0.525	5.04	0.038
B*D	0.05	0.833	6.98	0.017	30.14	0.000	0.12	0.739
B*E	0.63	0.438	0.08	0.783	2.45	0.136	0.89	0.359
C*D	0.03	0.867	1.81	0.196	1.54	0.232	0.14	0.709
C*E	3.02	0.100	2.23	0.154	29.55	0.000	1.12	0.305
D*E	4.89	0.041	0.37	0.550	0.25	0.817	1.38	0.257

All: $S = 0.0648608$; $R^2 = 70.26\%$ and; $R^2_{(adj)} = 42.28\%$.

P-Value by Anderson-Darling test: *DEV 01* = 0.235, *DEV 02* = 0.100, *DEV 03* = 0.057 and *DEV 04* = 0.123.

From Table 3., it is concluded that the critical manufacturing parameters are B and A, and also for *DEV 01*. For *DEV 02*, the factor B stands out as significant; for *DEV 03*, all factors are significant; and in *DEV 04*, in sequence, the most significant factors are B, A, and D. Also, at least 01 factor, or its interaction effect, is significant for one error type analyzed (except the factor E for *Dev 4*).

It is graphically presented in Fig.4.: the interactions of the factors vs. the errors using ANOVA. The analysis of the graphs confirms that the critical process factors are A and B, and that correlation between them is predominantly inverse and not proportional. Also, for all deviations, there is evidence of interaction between all the factors, and we see that there is no direct relationship between the levels (-1 and +1) of the factors and lower value of deviations.

Finally, it can be concluded, by this data analysis, that the modification of factor levels cannot be studied in isolation for each type of deviation because the optimal levels are different for each deviation, for example: for *DEV 01* are the +1 levels of factors A, B and D combined with the -1 levels of factors C and E (+A, +B, -C, +D and -E); for *DEV* 02, the optimal selection would be + A, + B, - C, + D and + E; for DEV 03: +A, +B, +C, +D and + E; and to minimize DEV 04 are +A, -B, -C, -D, and 0 (center point level).

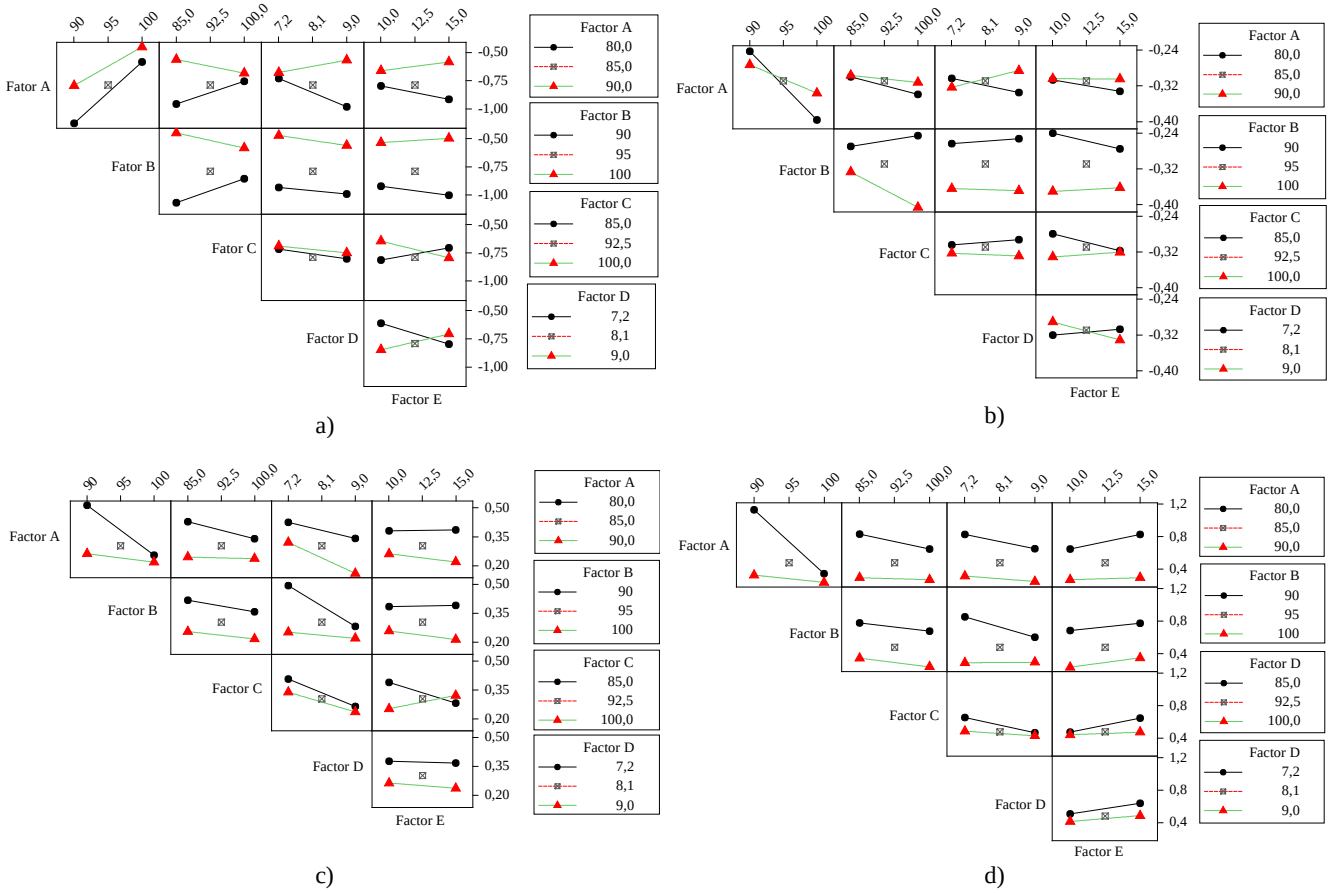

Fig.4. Interactions plot of factors: a) Interactions for *DEV 01*; b) Interactions for *DEV 02*; c) Interactions for *DEV 03*;d) Interactions for *DEV 04.*

3. DEVELOPMENT OF MULTIPLE RESPONSE OPTIMIZATION MODELS BY MULTIPLE LINEAR REGRESSION

First, with the data analysis developed, Multiple Linear Regression Models were developed for each type of response variable (error). So, for each one it was calculated: the constants β_0, the regression coefficients β_j, the cross-product terms of the input variables taken two to two $\beta_j x_k x_{k+1}$, and the random error term ε. Table 4. presents the calculated coefficients for each type of error being *MLR* model 01 for DEV 01, *MLR* model 02 for *DEV 02*, and so on, respectively. To evaluate the adequacy of these models to the data, we calculated the Coefficient of Determination (R^2), the Pearson Correlation Coefficient (r), the Mean Squared Error (*MSE*), and Mean Absolute Error (*MAE*), which are presented in the table. It is evident by the R2 value that capabilities of the models to predict the data are higher that 94 %, the r values above 0.97 indicate a very strong correlation between the response variables of regression models and *MSE* and *MAE*, which prove that mean values of prediction errors are less than 6 %.

The Multiple Response Optimization Models algorithms were developed and implemented using the *MLR* set as sub-models. For this purpose, the script sub-codes were developed in numerical analysis and programming software (MATLAB®), which uses *MLR*s to develop part of the *MRO* algorithm. The regression models developed for each type of error were programmed and the coefficients and constants of the estimates were coded and converted into external data files. The correlation of outputs of multiple response models were tested and evaluated, being that the *r* values found were lower than 0.76.

Also, to select the set of optimal values of factors by the *MRO* algorithms, a general objective function was developed. Equation (7) presents this O_j estimator value used to quantify a solution given a set of input factors.

$$O_j = \frac{1}{8}\sum_{i=1}^{4}\{(D_i)x\ Weight_i\} \qquad (7)$$
$$\text{for } D_i = \frac{MLR_{i,j}}{admissible\ error_i}$$

where j represents the *j-th* coefficient of performance for a (01) solution vector and i the deviation type, where i = 1, 2, 3, and 4 for the deviations *DEV* 01, *DEV* 02 *DEV* 03, and *DEV* 04. Consequently, they are pretested and restrict the desired ranges for all deviation of solution for: $0 \leq MLR_i < admissible\ error_i$. For each test the function O_j assigns numbers between 0 and 1, where $O_j = 1$ is a value completely undesirable and $O_j = 0$ is the optimal value and so, the function's internal search minimizes D values for the target values of $D_i = 0$. The values of the "admissible errors" for i = 1, 2,…4 were defined as | 0.6 mm |, | 2.1 mm |, | 1 mm |, | 0.72º | and the *i-th* weights adopted are: 2, 2, 3 and 1, respectively.

Table 4. Multiple linear regression models: Coefficients of the model parameters.

Parameter	**Model Type**			
	MLR for DEV 01	***MLR for DEV 01***	***MLR for DEV 01***	***MLR for DEV 01***
	Coefficient value			
Constant	-27. 949777290	9. 868354195	69. 065370830	27. 416482210
A	0.147198177	-0.127872101	-0.710060972	-0.208447796
B	0.309674115	-0.064336080	-0.713180139	-0.221828149
C	-0.166175729	-0.047886613	0.131432500	0.007012008
D	4. 219830150	0.274325867	-0.459804784	-1.188922512
E	-0.992314896	-0.005321494	-0.739571944	-0.250265384
A*B	-0.002028656	0.000906562	0.006966083	0.002162254
A*D	-0.017926562	0.001316982	0.008850926	0.004532616
A*E	0.007246438	0.001383035	0.002194667	-0.001543027
A*C	0.001335354	0.000165253	-0.001043778	-0.000311275
B*D	-0.019336285	-0.005722334	-0.000390741	0.001178064
B*E	-0.000626063	-0.000311248	0.005097667	0.003586834
B*C	0.000775354	0.000287991	0.000180222	-0.000340673
D* E	0.002764931	-0.001937292	0.014426852	0.004500225
D*C	-0.009421644	0.001797519	-0.005333642	0.006576914
E*C	0.004313208	-0.000717682	-0.000784556	-0.000218731
Center point adjustment constant	-0.049108594	0.003270649	-0.029714583	-0.007910518

R^2: *MLR* for *DEV 01* = 94,29%; *MLR* for *DEV 02* = 99,99%; *MLR* for *DEV 03* = 99,97%; *MLR* for *DEV 04* = 99,98% and; All models = 98.56%;
r: *MLR* for *DEV 02* = 0.971; *MLR* for *DEV 02* = 1.000; *MLR* for *DEV 03* = 1.000; *MLR* for *DEV 04* = 1.000 and; All models = 1.000;
MSE: *MLR* for *DEV 01* = 0,1950; *MLR* for *DEV 02* = 0,0; *MLR* for *DEV 03* = 0,0002; *MLR* for *DEV 04* = 0,0; all models = 0,0488;
MAE: *MLR* for *DEV 01* = 0,0484; *MLR* for *DEV 02* = 0,0016; *MLR* for *DEV 03* = 0,0149; *MLR* for *DEV 04* = 0,0040; all models = 0,0172.

Based on this pre-development, the first code of the algorithm, the *MRO* model 01, was written to find the *n-th* best solutions inside of the full factorial design. The algorithm is processed according to this logic: first it discretizes the input values (factors) in the *j-th* possible solution and then it uses the data matrix and the sub-code developed with the *MLR* model to calculate the deviations of a *j-th* prediction. Then, by means of (7) the values of the general objective functions are calculated and, finally, compared, ranked and written in descending order are the *n-th* possible solutions with the respective input values. Thus, it searches for the minimum value of the general solution vector (minimizes O_j). This procedure was developed and implemented using MATLAB® software.

Table 5. presents the 05 best results. From the table it is evident that only one (01) set of factors/parameters is presented as the best solution to minimize deviations, having a value of O_j equal to 0.18, and factors A = 90 s, B = 100 %, C = 100 bar, D = 7.2 s and E = 15 mbar.

A second attempt was made to find optimal solutions. For this the solution space of the input variables was expanded to values beyond those used in the main experimental procedure, and also, smaller limits were defined for the discretization. For this new search the *MRO* model 02 Algorithm was programmed. Table 6. presents the 05 best results.

As shown in Table 6., the *MRO* model 02 algorithm can predict other *n-th* configurations of input variables, which minimize the O_j estimator. We see that several configurations have the same value of *Oj* and very close values, which were already predicted when dealing with a problem with multiple solution spaces. However, analyzing Fig.4., we see that in general, for the set of deviations, factor "A" has better results in levels ≥ 85, factor "B" in levels ≥ 95, since factor "C" improves next at levels ≤ 92.5, factor "D" at mean levels ≥ 8.1, and factor "E" close to level ≥ 12.5. From this follows that the first solution from Table 6. is the most appropriate solution to the problem.

Table 5. Summary of the 05 best minimum of O_j value for the 1st variation of the optimization algorithm.

O_j value	**Factor**				
	A (s)	***B (%)***	***C (bar)***	***D (s)***	***E (mbar)***
0.18	90	100	100	7. 2	15.0
0.25	90	100	100	7. 2	12. 5
0.27	90	100	93	7. 2	15.0
0.27	81	100	85	9.0	10.0
0.28	90	100	100	8. 1	15.0

Table 6. Summary of the 05 best minimum of O_j value for the 2nd variation of the optimization algorithm.

O_j value	**Factor**				
	A (s)	***B (%)***	***C (bar)***	***D (s)***	***E (mbar)***
0.05	94. 5	97. 5	92. 5	6. 3	15
0.06	94. 5	95	96. 25	6. 3	15
0.06	94. 5	95	100	7. 2	15
0.08	81	105	92. 5	7. 2	7. 5
0.08	78. 75	105	92. 5	7. 2	7. 5

3.1. Validation tests

New experimental tests were performed to validate the MRO algorithms and to test their efficiencies in predicting the multiple errors in two different search conditions developed. For the development of these validation tests, two test sequences were performed, using five samples of each type, according to the selection of factors (parameters) developed, respectively. Also, the same experimental conditions, infrastructure and material were preserved. Afterwards, the samples were inspected, adopting the same procedures already described and the errors previously calculated. Table 7. and Table 8. show the errors measured in the pieces for each test model.

Table 7. Deviations: samples of 1st *MRO* model.

Sample	**Results**			
	DEV 1 (mm)	DEV 2 (mm)	DEV 3 (º)	DEV 4 (mm)
1st	-0.269	0.240	0.201	-0.521
2nd	-0.367	0.215	0.308	-0.536
3nd	-0.113	0.108	0.259	-0.423
4nd	-0.084	0.246	0.114	-0.460
5nd	-0.272	0.142	0.169	-0.520

Table 8. Deviations: samples of 2nd *MRO* model.

Sample	**Results**			
	DEV 1 (mm)	DEV 2 (mm)	DEV 3 (º)	DEV 4 (mm)
1st	-0.138	0.260	0.154	-0.308
2nd	-0.084	0.217	0.221	-0.287
3nd	-0.092	0.194	0.115	-0.406
4nd	-0.122	0.164	0.129	-0.342
5nd	-0.302	0.107	0.106	-0.339

As evidenced by the values of the tables, the tests produced parts within the tolerance limits defined in this study; even the lower and upper limits of the deviations were at acceptable levels. The values of the errors are shown in Fig.5. For comparative purposes, the data of the best performing test pair (01 and 11) are shown with A = 90 s, B = 100 %, C = 90 Bar, D = 7,2 s and D = 10 mBar.

As shown in Fig.5., even at different levels, all the deviations follow the same trend, independently of the optimal configurations of the models. Also, we see that, on average, the results of the *MRO* model 02 samples present errors in smaller values when compared with the parts produced with the parameters of the *MRO* model 01, and in general, a significant improvement when compared with the best samples of the experimental test.

To compare the efficiency of the predictions, Table 9. and Table 10. present the results of the expected value (or mean) of the deviations for samples in the validation tests, at the 95 % confidence interval (IC) on the mean ($\alpha = 0.05$). The predictions of the models and also the results of the best samples in the main experimental tests, samples 01 and 11, are shown (Table 2.).

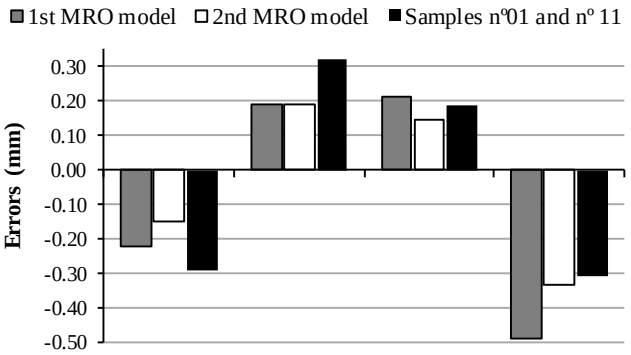

Fig.5. Comparison of mean value of the errors in the samples.

Table 9. General comparative of results for the 1st *MRO* model.

Error type	**Samples of validation**			***MRO* model 01**	**Samples nº01 and nº 11**
	Mean	***95% CI***		***predicted***	***Mean***
DEV 01	-0.221	-0.117	-0.325	-0.075	-0.293
DEV 02	0.190	0.136	0.244	0.273	0.323
DEV 03	0.210	0.144	0.276	0.084	0.188
DEV 04	-0.492	-0.449	-0.534	-0.297	-0.310
O_j	0.26	0.18	0.34	0.18	0.31

Table 10. General comparative of results for the 2nd *MRO* model.

Error type	**Samples of validation**			***MRO* model 01**	**Samples nº01 and nº 11**
	Mean	***95% CI***		***predicted***	***Mean***
DEV 01	-0.148	-0.070	-0.226	-0.006	-0.293
DEV 02	0.188	0.138	0.238	0.029	0.323
DEV 03	0.145	0.104	0.185	0.055	0.188
DEV 04	-0.336	-0.297	-0.376	-0.230	-0.310
O_j	0.20	0.13	0.26	0.05	0.31

Finally, based on these results, we conclude that the validation tests produced samples within the tolerance limits defined in this study with a significant improvement in product quality.

4. DISCUSSION AND CONCLUSIONS

The proposed procedure can be considered a new method to mutually model the manufacturing parameters and to predict and minimize dimensional and geometric errors in products during the vacuum thermoforming process, using a small number of tests in a laboratory.

As already presented by other authors [7], [8], [11], [30], [26], the simultaneous analysis of parameters and errors of products does not allow us to select a single set of optimal values. This is because different levels of one factor could be optimal levels for different response variables (e.g., factor E). Consequently, it is necessary to use a multi-objective optimization technique to find the set of optimal levels for the problem.

The analysis of the interaction between product errors and parameters of manufacture presented us new information, such as:

- The parameters of heating influence all types of geometrical and dimensional errors in a more significant way, considering all their different levels.
- In addition to mold characteristics [15], [36] the parameters of mold can influence geometric errors;
- The interaction of two factors can influence the deviations of the product by reducing the value of dimensional errors, but a significant increase of geometric errors can occur;
- The manufacturing parameters interact simultaneously with the errors in a non-linear and non-proportional model;

  In the analysis of the deviation value as a function of the variation of factor levels, we can conclude that:
- The factors "Heating Time" and "Heating Power" at high levels result in smaller dimensional deviations of height and lateral angles;
- In relation to the reduction of deviations the parameters "Vacuum Time" and "Vacuum Pressure" for some deviations have direct correlation and to others, inversely, "Vacuum Time" and "Mold Pressure" have direct correlation in all deviations;
- The parameter "heating time" in value equal to or greater than 90 seconds, produces smaller deviation values.
- In general, among the analyzed factors, the "Mold Pressure" has the lowest ratio rate in its levels and, for the "*DEV 02*", the factors have an inverse correlation behavior in relation to the other deviations.

As for the *MLR* models, it can be concluded from the R^2 values that they are valid to represent the sample data and that this technique is valid to model errors in this process.

From Table 9. and Table 10., we conclude that within the confidence interval, the implemented models have indeed been able to find new improved solutions and have a significant gain in the overall reduction of errors of validation test and of value of objective function.

The *MRO* models have been able to find a set of *n-th* possible solutions that altogether minimize errors and these solutions are in values outside the limits of test of the main experiment.

In addition, by the analysis of Fig.5. and Table 9. and Table 10., we conclude that the minimization solution found by the optimization of model 02 is the best configuration of factor levels for the problem.

However, as shown in Table 10., there were failures in the predicted values in the new range of values [7], and from this we conclude that the solutions of optimization models for the errors are neither linear nor curved in the surface model. Thus, when using a linear model (*MLR*) with center point to model an (01) error, we obtain a representative model in relation to slope and direction [27], but this model is not able to represent all the local minima and the global minimum of a solution surface in this problem.

ACKNOWLEDGMENT

The authors are grateful to "Instituto Federal de Educação, Ciência e Tecnologia de Minas Gerais – Campus Betim", for supporting the development of this paper.

REFERENCES

[1] Throne, J.L. (2008). *Understanding Thermoforming* (2th ed.). Hanser, 279.

[2] Sala, G., Landro, L.D., Cassago, D. (2002). A numerical and experimental approach to optimise sheet stamping technologies: Polymers thermoforming. *Journal of Materials and Design*, 23, 21-39.

[3] Throne, J.L. (1996). *Technology of Thermoforming*. Hanser, 882.

[4] Kuttner, R., Karjust, K., Ponlak, M. (2007). The design and production technology of large composite plastic products. *Proceedings of the Estonian Academy of Sciences: Engineering*, 13 (2), 117-128.

[5] Muralisrinivasan, N.S. (2010). *Update on Troubleshooting in Thermoforming*. Smithers Rapra Technology.

[6] Ghobadnam, M., Mosaddegh, P., Rejani, M.R., Amirabadi, H., Ghaei, A. (2015). Numerical and experimental analysis of HIPS sheets in thermoforming process. *International Journal of Advanced Manufacturing Technology*, 76, 1079-1089.

[7] Yang, C., Hung, S.W. (2004). Modeling and optimization of a plastic thermoforming process. *Journal of Reinforced Plastics and Composites*, 23 (1), 109-121.

[8] Yang, C., Hung, S.W. (2004). Optimising the thermoforming process of polymeric foams: An approach by using the Taguchi method and the utility concept. *The International Journal of Advanced Manufacturing Technology*, 24, 353-360.

[9] Klein, P. (2009). *Fundamentals of Plastics Thermoforming* (11th ed.). Morgan & Claypool Publishers.

[10] Engelmann, S. (2012). Optimizing a thermoforming process for packaging. In *Advanced Thermoforming: Methods, Machines and Materials, Applications and Automation*. John Wiley & Sons, 125-136.

[11] Leite, W.O., Campos Rubio, J.C., Mata Cabrera, F., Carrasco, A., Hanafi, I. (2018). Vacuum thermoforming process: An approach to modeling and optimization using artificial neural networks. *Polymers*, 10 (143), 1-17.

[12] Pasandideh, S.H, Niakti, S.T.A., Atyabi, S.M. (2014). A new approach to solve multi-response statistical optimization problems using neural network, genetic algorithm, and goal attainment methods. *International Journal of Advanced Manufacturing Technology*, 75, 1149-1162.

[13] Warby, M.K., Whitemana, J.R., Jiang, W.G., Warwick, P., Wright, T. (2003). Finite element simulation of thermoforming processes for polymer sheets. *Mathematics and Computers in Simulation*, 61, 209-218.

[14] Yhan, Z., Zhang, H. (2000). Wall thickness distribution in thermoformed food containers produced by a Benco aseptic. Polymer Engineering & Science, 40 (1), 1-10.
[15] Erdogan, E.S., Eksi, O. (2014). Prediction of wall thickness distribution in simple thermoforming moulds. *Journal of Mechanical Engineering*, 60 (3), 195-202.
[16] Kumar, A., Kumar, V., Kumar, J. (2013). Multi-response optimization of process parameters based on response surface methodology for pure titanium using WEDM process. *International Journal of Advanced Manufacturing Technology*, 68, 2645-2668.
[17] Kommoji, S., Banerjee, R., Bhatnaga, N., Ghosh, K.G. (2015). Studies on the stretching behaviour of medium gauge high impact polystyrene sheets during positive thermoforming. *Journal of Plastic Film & Sheeting*, 31 (1), 96-112.
[18] Velsker, M., Eerme, M., Majak, J., Pohlak, M., Karjust, K. (2011). Artificial neural networks and evolutionary algorithms in engineering design. *Journal of Achievements in Materials and Manufacturing Engineering*, 44 (1), 88-95.
[19] Martin, P.J., Keaney, T., McCool, R. (2014). Development of a multivariable online monitoring system for the thermoforming process. *Polymer Engineering & Science*, 54 (12), 2815-2823.
[20] Chy, M.M.I., Boulet, B., Haidar, A. (2011). A model predictive controller of plastic sheet temperature for a thermoforming process. In *American Control Conference (ACC)*, San Francisco, CA, USA, 4410-4415.
[21] Boutaous, M., Bourgin, P., Heng, D., Garcia, D. (2005). Optimization of radiant heating using the ray tracing method: Application to thermoforming. *Journal of Advanced Science*, 17 (1-2), 139-145.
[22] Zhen-Zhe, L., Cheng, T.H., Shen, Y., Xuan, D.J. (2015). Optimal heater control with technology of fault tolerance for compensating thermoforming preheating system. *Advances in Materials Science and Engineering*, 2015 (12), 1-5.
[23] Meziane, F., Vadera, S., Kobbacy, K., Proudlove, N. (1990). Intelligent systems in manufacturing: Current developments and future prospects. *Integrated Manufacturing Systems*, 11 (4), 218-238.
[24] Tadeusiewicz, R. (2011). Introduction to intelligent systems. In *Intelligent Systems: The Industrial Electronic Handbook* (2nd ed.). CRC Press, 1.1-1.12.
[25] Pham, D.T., Pham, P.T.N. (2001). Computational intelligence for manufacturing. In *Computational Intelligence in Manufacturing Handbook*. CRC Press, 1.1-1.8.
[26] Costa, N., Garcia, J. (2016). Using a multiple response optimization approach to optimize the coefficient of performance. *Applied Thermal Engineering*, 96, 137-143.
[27] Fogliatto, F. (2008). Multiresponse optimization of products with functional quality characteristics. *Quality and Reliability Engineering International*, 24, 927-939.
[28] Jeyapaul, R., Shahabudeen, P., Krishnaiah, K. (2005). Quality management research by considering multi-response problems in the Taguchi method – a review. *International Journal of Advanced Manufacturing Technology*, 26, 1331-1337.
[29] Pal, S., Gauri, S.K. (2010). Assessing effectiveness of the various performance metrics for multi-response optimization using multiple regression. *Computers & Industrial Engineering*, 59, 976-985.
[30] Khanlou, H.M., Ang, B.C., Talebian, S., Barzani, M.M., Silakhori, M., Fauzi, H. (2015). Multi-response analysis in the processing of poly (methyl methacrylate) nano-fibres membrane by electrospinning based on response surface methodology: Fibre diameter and bead formation. *Measurement*, 65, 193-206.
[31] EL-Taweel, T.A. (2009). Multi-response optimization of EDM with Al-Cu-Si-TiC P/M composite electrode. *International Journal of Advanced Manufacturing Technology*, 44, 100-113.
[32] Montgomery, D.C. (2013). *Design and Analysis of Experiments* (8th ed.). John Wiley, 10.1-10.9.
[33] Wan, W., Birch, J.B. (2011). A semiparametric technique for the multi-response optimization problem. *Quality and Reliability Engineering International*, 27, 47-59.
[34] Rosen, S.R. (2002). *Thermoforming: Improving Process Performance*. Society of Manufacturing Engineers.
[35] Montgomery, D.C. (2013). *Design and Analysis of Experiments* (8th ed.). John Wiley, 9.1-9.7.
[36] Kumar, P.S., Kumar, G.K., Kommoji, S., Banerjee, R., Ghosh, A.K. (2014). The effect of material characteristics and mould parameters on the thermoforming of thick polypropylene sheets. *Journal of Plastic Film & Sheeting*, 30 (2), 162-180.

Received December 12, 2017.
Accepted May 14, 2018.

MEASUREMENT SCIENCE REVIEW, **18**, (2018), No. 3, 123-129

DE GRUYTER OPEN

MEASUREMENT SCIENCE REVIEW

Journal homepage: http://www.degruyter.com/view/j/msr

ISSN 1335-8871

Experimental Models and Correlations between Surface Parameters after Slide Diamond Burnishing

Mieczyslaw Korzynski[1], Kazimiera Dudek[1], Arkadiusz Palczak[1], Bartosz Kruczek[1], Paweł Kocurek[2]

[1] *Centre for Innovative Technologies, University of Rzeszow, Pigonia 1, 35-310 Rzeszow, Poland, mk@ur.edu.pl*
[2]*Mechanical Engineering and Aeronautics Faculty, Rzeszow University of Technology, W. Pola 2, 35-959 Rzeszow, Poland*

In the paper the set of representative parameters for a comprehensive assessment of the surface texture status after slide burnishing has been proposed. The analysis of correlations between the parameters of the surface texture, obtained by slide diamond burnishing of 317Ti steel has been performed. Correlations have been determined and several groups of surface texture parameters with strong mutual correlations (also parameters uncorrelated with the other) have been selected. For both groups of parameters - representative and uncorrelated - experimental mathematical relations defining influences of the input parameters of slide diamond burnishing on the surface texture parameters have been developed. Also, interaction effects for individual parameters of this finishing process have been disclosed. It has been found that by appropriate selection of input conditions of the slide diamond burnishing process, it is possible to obtain a wide range of states of the surface texture.

Keywords: Surface texture, finishing, slide diamond burnishing, 317Ti.

1. INTRODUCTION

Surface texture of the machine parts is the result of their finishing treatment. Often, the appropriate shaping of surface texture can radically change properties of the product, such as abrasion resistance, corrosion resistance, as well as their strength during changing operational loads. Therefore, various finishing techniques (inter alia slide diamond burnishing) are more and more developed and increasingly used. They are enabling to obtain optimal surface texture for the working conditions of given parts of machines. In such cases, the assessment of surface texture by conventional amplitude parameters is far from enough [1]-[3]. It's commonly found that the surfaces, having same values of the amplitude parameters, can have very different values of other surface texture parameters and thus different functional properties. Therefore, already in 1990, the surface texture has been evaluated on the basis of eight parameters [4]. According to later proposals, which are included on the so-called Birmingham List [5], [6], it is necessary to take measurements of 14 parameters of the surface texture, to estimate its properties. A slightly different opinion have the authors of paper [1], who believe, that a representative set of surface texture parameters should be different and should depend on the type of work of the particular surface.

According to the current ISO 25178-2 standard for the complete characterization of the surface texture, dozens of parameters should be measured. However, in industrial practice such a comprehensive characterization is never needed and a full assessment is never carried out. In the case of general-purpose, not very responsible machine parts, requirements are often set by determining the maximum permissible values of *Ra*/*Sa* or other amplitude parameters [7]. In paper [8], measurements of the polymers wear were based on the *Ra* parameter. Meanwhile in [9], tests of the correlations between bearing vibrations and various surface parameters were made. It was stated that vibration level had had the highest correlation coefficient with Sa/*Ra* parameters. However, in [10] it was found, that single *Ra* parameter is insufficient to describe the surface texture functionality. The optimization of hard turning process based on different stereometric parameters was made. Also in [7] there was surface state valuation based on different amplitude parameters, and in [11] roughness of the polished specimens was modelled with the use of *Ra* and *Ry* (maximum height of the profile) parameters.

In case of parts working in the friction conditions, numerous other parameters are also important. In work [12], there are 11 highlighted parameters that need to be considered during testing the correlation between surface texture and sliding friction. In [13], five amplitude parameters (*Ra, Rq, Rz, Rku, and Rsk*) and five material ratio parameters (*Rk, Rpk, Rvk, MR*1, *and MR*2) were used to determine the best indicator of run-in. However, it follows from the study presented in [14] that one can fairly precisely describe a piston skirt surface topography using the following parameters: *Sq, Ssk, Str,* and *Sdq*. For the detailed description of topography, the authors of work [14]

DOI: 10.1515/msr-2018-0018

also recommend parameters $St_{\pm 3\sigma}$, *Sku*, *Sds*, *Ssc*, and $P\Delta a_x/P\Delta a_y$. Meanwhile in [15], tribological properties were evaluated in connection with six 3D parameters such as: *Sa*, *Sq*, *St*, Abbot-Firestone Curve, Texture Directivity, and 3D view of surface. In similar researches presented in [16], besides the Abbot-Firestone Curve and functional parameters, that came out of it, parameters *Sq*, *Ssc*, *Sds*, *Spd* were also considered. Correlations between tribological properties and the state of surface, based on the 3D view of surface, and surface profile, but also *Sz*, *Sq*, *Ssk*, *Sku*, *Str*, *Sal*, *Spd* parameters, were described in [17]. In [18] the *Ssk* parameter was strongly correlated with the pressure, thickness of the lubrication layer in elastohydrodynamically lubricated sliding joints. The effect of surface geometry on the hydrodynamic bearing parameters was also shown in [19]. In [20] it was proven, that with usage of *Ssk* and *Sku* parameters it is possible to predict the contact region's tribological behavior. It was stated that higher *Sku* and negative *Ssk* value will end in lower friction and it was confirmed that both of *Ssk* and *Sku* parameters can be used to design the textured surface. Meanwhile in [21] the *Rq*, *Rz*, *tp* (bearing coefficient), *Rsk* parameters were used to describe the fabric's wear level. The spatial and hybrid stereometric parameters were used in [22] to estimate the surface topography in sliding friction conditions. In [23] after the tests of the surface roughness and texture parameters during lubricated sliding friction, there were few different specimens used. They were made with the isotropic and anisotropic surface roughness and with different textures. Thanks to these various specimens, the influence of the isotropic/anisotropic surface structure and *Ssk* and *Sku* parameters on the friction was proven. Also in [24] it was shown, that the tribological wear was correlated not only with *Ra* but also *Ssk* and *Sku* parameters.

The mentioned researches have varied approach to the problem. It also can be seen in the researches of the dynamic loaded surfaces. For example in [12], parameters *Sa*, *Sq*, *Std*, and *Svi* were considered as the most important. In [25], during fatigue tests, only *Sq*, *Sk* parameters were verified and in [26] only *Sa*/*Ra* and *Sz*/*Rz* parameters and 3D view of surface were considered.

It is known and has been frequently found during experiments, that there are correlations between different surface texture parameters (including those not necessarily resulting from physical dependencies). For example, in [27], correlations between 21 surface texture parameters defined in the ISO 25178-2 standard have been found and during the examination of the 17 surfaces obtained as a result of different machining methods there was found the existence of many strong correlations between surface texture parameters. The existence of this kind of correlations has also been shown in [28], after examining the surfaces of the cylinder liners. And in [29] the correlations between different surface texture parameters have been described and a way of identifying parameters that are significantly changing during the manufacturing process has been proposed. The fact that some surface texture parameters are unnecessary because of redundancy has also been shown in [30].

Analysis of these dependencies enables determination of necessary requirements for the drawings of the state of machined surfaces, but also allows us to reduce the number of surface texture parameters that should be controlled during the production process. This kind of analysis for the slide diamond burnishing process of the cylindrical-shaped parts made of austenitic stainless steel has been carried out in this work. The work also includes the calculations of mathematical relations, defining the influence of the basic parameters of slide diamond burnishing on the surface texture properties.

2. RESEARCH METHODOLOGY & MEASURING TECHNIQUES

The samples made of austenitic stainless steel 317Ti after drawing process have been used for the model studies. The samples were prepared (by cold drawing) in the shape of shafts, with a diameter of 12 mm, a length of 100 mm and a surface roughness *Sa* = 1.05 µm. Presented in Fig.1., slide burnishing process (this technology was described in detail in [31]) was performed on the universal lathe using a special chuck ensuring elastic and adjustable burnishing force. One-piece spherical burnishers made of PCD (synthetic polycrystalline diamond also known as carbonado) have been used. During the burnishing process a lubricating mixture of oil and kerosene with the proportion of 20:80 has been used. Studies of influence of selected slide burnishing parameters on the surface roughness were carried out according to the Hartley plan PS/DS-P:Ha3 [32] (Table 1.). Calculation methodology was described in detail in [33].

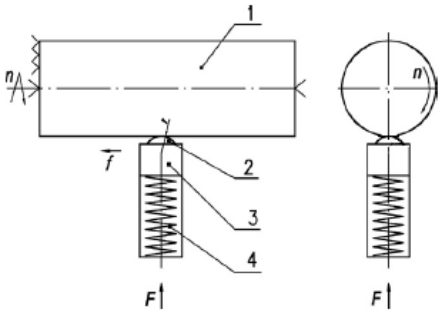

Fig.1. Slide diamond burnishing: 1 - object burnished, 2 - burnishing tool, 3 - tool holder, 4 - pressure control spring, n - rotational speed, f - feed, F - burnishing force.

Experiment required implementation of the N = 11 tests, with input parameters on three levels of variation. Values of input parameters have been selected according to the previously acquired experience, technical capabilities of the test bench and the preliminary studies. The experiment was carried out with three repetitions. Regression analysis of the results was performed with the significance level of 0.05. This allowed us to obtain mathematical relationships (regression equation), which describe the influence of the input parameters of the slide diamond burnishing process on the achieved results. The input parameters were: radius of the tool tip, load force, and tool feed. Output parameters were parameters of the surface texture obtained during the

process. The values of input parameters used during the individual tests are given in Table 2.

Table 1. Matrix of the Hartley's plan PS/DS – P:Ha3.

Processing variant	x_1	x_2	x_3	x_1^2	x_2^2	x_3^2	$x_1 x_2$	$x_1 x_3$	$x_2 x_3$
1	+	+	+	+	+	+	+	+	+
2	+	-	-	+	+	+	-	-	+
3	-	+	-	+	+	+	-	+	-
4	-	-	+	+	+	+	+	-	-
5	+	0	0	+	0	0	0	0	0
6	-	0	0	+	0	0	0	0	0
7	0	+	0	0	+	0	0	0	0
8	0	-	0	0	+	0	0	0	0
9	0	0	+	0	0	+	0	0	0
10	0	0	-	0	0	+	0	0	0
11	0	0	0	0	0	0	0	0	0

Table 2. Values of the input parameters for the experiments.

Input parameters	**Tool tip radius *r* [mm]**	**Load force *F* [N]**	**Tool feed *f* [mm/rev]**
Zero level (0)	3	100	0.07
Upper level (+)	4	150	0.11
Lower level (-)	2	50	0.03

Measurements of surface texture parameters were carried out on the Talyscan 150 profilometer with the software for surface analysis TalyMap Expert 2.0.15. The measurements were performed with the contact method, using inductive contact sensor equipped with the measuring needle with tip radius 5 microns. The set of 28 parameters given in ISO-25178-2 and ISO-4287 standards was measured. With the use of results of these measurements (listed in Table 3.) Pearson's linear correlation coefficients between all studied parameters were calculated. The results of these calculations are given in the Table 4.

Table 3. Results of the surface texture measurements of tested samples.

Measured parameter		**Processing variants**										
		1	**2**	**3**	**4**	**5**	**6**	**7**	**8**	**9**	**10**	**11**
1	*Sa*	0.153	0.209	0.349	0.341	0.206	0.234	0.145	0.2	0.216	0.12	0.156
2	*Sq*	0.262	0.435	0.496	0.616	0.438	0.313	0.211	0.416	0.291	0.189	0.256
3	*Sp*	3.16	2.22	4.47	2.04	2.42	2.84	2.59	3.83	1.35	1.23	2.13
4	*Sv*	6.19	8.61	5.82	16.2	8.54	4.53	4.79	11.1	6.95	7.44	8.52
5	*St*	9.39	10.8	10.3	18.3	11	7.37	7.38	14.9	8.31	8.67	10.7
6	*Ssk*	-6.04	-6.8	-0.954	-7.31	-7.79	-0.748	-2.99	-9.91	-2.43	-7.17	-8.82
7	*Sku*	83.3	77	9.27	115	99.5	6.84	41.5	179	36	158	197
8	*Sz*	7.22	8.92	8.75	12.1	9.63	5.16	5.02	11.3	5.02	4.58	7.54
9	*STp*	57.2	61.1	56.6	56.4	57.8	53.7	52.3	55.1	50.5	53.2	52.8
10	*Smmr*	0.00619	0.00861	0.00582	0.0162	0.00854	0.00453	0.00479	0.0111	0.00695	0.00744	0.00852
11	*Smvr*	0.00316	0.00222	0.00447	0.00204	0.00242	0.00284	0.00259	0.00383	0.00135	0.00123	0.00213
12	*SPc*	213	190	315	88.5	208	299	220	235	77.1	288	144
13	*Sds*	1823	1852	1486	1595	1887	1835	1791	2315	1168	2225	1482
14	*Str*	0.447	0.549	0.0872	0.563	0.858	0.264	0.218	0.634	0.0558	0.545	0.213
15	*Sal*	0.0437	0.0421	0.0285	0.0706	0.0892	0.0475	0.0316	0.076	0.0312	0.115	0.035
16	*Std*	22	45	2	63.5	26.5	1.5	88	45	88.5	45	63.5
17	*Sfd*	2.13	2.06	2.38	2.1	2.03	2.38	2.27	2.08	2.23	2.12	2.14
18	*Sdq*	0.0355	0.0484	0.104	0.0495	0.0399	0.0624	0.0306	0.037	0.0291	0.0213	0.0284
19	*Ssc*	0.00562	0.00557	0.0148	0.00698	0.00542	0.00976	0.00599	0.00515	0.00582	0.00444	0.00545
20	*Sdr*	0.0623	0.115	0.536	0.121	0.078	0.193	0.0466	0.0669	0.0421	0.0226	0.04
21	*Sbi*	0.0913	0.238	0.131	0.442	0.221	0.131	0.0919	0.122	0.315	0.193	0.141
22	*Sci*	0.96	0.739	1.22	0.929	0.864	1.32	1.28	0.917	1.39	1.2	1.12
23	*Svi*	0.149	0.165	0.167	0.141	0.146	0.152	0.137	0.122	0.113	0.121	0.119
24	*Sk*	0.421	0.455	0.865	0.914	0.46	0.7	0.443	0.512	0.706	0.347	0.479
25	*Spk*	0.164	0.237	0.496	0.447	0.305	0.273	0.179	0.398	0.208	0.159	0.173
26	*Svk*	0.465	0.903	0.834	0.995	0.808	0.458	0.322	0.672	0.381	0.239	0.337
27	*Sr1*	8.79	11.7	11.4	9.17	13.2	9.03	9.28	10.3	9.55	10.2	8.99
28	*Sr2*	87.9	86.6	83.8	87.3	87.2	87.6	89.9	89.4	93	88.4	90.2

Table 4. Pearson's correlation coefficients between all measured surface texture parameters.

	Sr2	***Sr1***	***Svk***	***Spk***	***Sk***	***Svi***	***Sci***	***Sbi***	***Sdr***	***Ssc***	***Sdq***	***Sfd***	***Std***	***Sal***	***Str***	***Sds***	***SPc***	***Smvr***	***Smmr***	***STP***	***Sz***	***Sku***	***Ssk***	***St***	***Sv***	***Sp***	***Sq***	***Sa***
Sa	-0.54	0.18	0.76	0.89	0.93	0.48	-0.06	0.48	0.74	0.73	0.80	0.31	-0.30	-0.21	-0.13	-0.41	-0.07	0.40	0.40	0.29	0.55	-0.39	0.32	0.52	0.39	0.40	0.87	1
Sq	-0.55	0.40	0.96	0.87	0.68	0.46	-0.51	0.57	0.48	0.39	0.58	-0.16	-0.24	0.04	0.32	-0.12	-0.19	0.34	0.68	0.58	0.86	-0.08	-0.11	0.78	0.68	0.34	1	
Sp	-0.56	0.15	0.36	0.59	0.25	0.52	-0.13	-0.54	0.68	0.64	0.69	0.35	-0.59	-0.30	-0.08	0.15	0.54	1	-0.16	0.32	0.39	-0.23	0.18	0.13	-0.16	1		
Sv	-0.03	0.03	0.59	0.47	0.32	-0.17	-0.57	0.72	-0.18	-0.27	-0.12	-0.61	0.25	0.39	0.50	0.07	-0.55	-0.16	1	0.27	0.79	0.54	-0.64	0.96	1			
St	-0.20	0.07	0.69	0.65	0.39	-0.02	-0.60	0.57	0.01	-0.07	0.08	-0.51	0.08	0.29	0.48	0.12	-0.39	0.13	0.96	0.37	0.91	0.47	-0.59	1				
Ssk	-0.13	-0.15	-0.15	0.07	0.46	0.36	0.71	-0.14	0.56	0.69	0.54	0.91	-0.21	-0.55	-0.71	-0.48	0.29	0.18	-0.64	-0.28	-0.54	-0.92	1					
Sku	0.25	-0.05	-0.11	-0.14	-0.44	-0.57	-0.42	0.04	-0.53	-0.62	-0.56	-0.72	0.25	0.53	0.48	0.43	-0.21	-0.23	0.54	-0.01	0.35	1						
Sz	-0.40	0.34	0.85	0.73	0.33	0.24	-0.75	0.37	0.19	0.06	0.27	-0.49	-0.14	0.18	0.54	0.14	-0.23	0.39	0.79	0.61	1							
STP	-0.73	0.58	0.77	0.33	-0.04	0.76	-0.85	0.09	0.27	0.09	0.36	-0.42	-0.48	0.10	0.57	0.27	0.14	0.32	0.27	1								
Smmr	-0.03	0.03	0.59	0.47	0.32	-0.17	-0.57	0.72	-0.19	-0.27	-0.12	-0.61	0.25	0.39	0.50	0.07	-0.55	-0.16	1									
Smvr	-0.56	0.15	0.36	0.60	0.25	0.52	-0.13	-0.54	0.68	0.64	0.69	0.35	-0.59	-0.30	-0.08	0.15	0.54	1										
SPc	-0.57	0.24	-0.12	0.12	-0.19	0.42	0.15	-0.69	0.48	0.46	0.44	0.42	-0.72	0.19	0.02	0.55	1											
Sds	-0.20	0.20	-0.03	-0.04	-0.56	-0.00	-0.40	-0.36	-0.26	-0.35	-0.24	-0.39	-0.28	0.69	0.68	1												
Str	-0.24	0.50	0.42	0.11	-0.37	0.08	-0.79	0.19	-0.36	-0.49	-0.28	-0.80	-0.17	0.77	1													
Sal	-0.09	0.31	0.03	0.03	-0.31	-0.26	-0.31	0.21	-0.34	-0.42	-0.35	-0.55	-0.12	1														
Std	0.77	-0.31	-0.29	-0.36	-0.13	-0.65	0.16	0.36	-0.61	-0.58	-0.65	-0.25	1															
Sfd	-0.13	-0.31	-0.26	0.15	0.48	0.24	0.79	-0.32	0.62	0.77	0.58	1																
Sdq	-0.77	0.28	0.55	0.74	0.68	0.74	0.06	-0.07	0.98	0.95	1																	
Ssc	-0.63	0.11	0.32	0.63	0.69	0.59	0.33	-0.14	0.97	1																		
Sdr	-0.74	0.28	0.45	0.69	0.63	0.66	0.15	-0.12	1																			
Sbi	0.09	0.07	0.47	0.29	0.51	-0.12	-0.19	1																				
Sci	0.38	-0.46	-0.67	-0.21	0.24	-0.34	1																					
Svi	-0.86	0.39	0.61	0.38	0.25	1																						
Sk	-0.27	-0.11	0.50	0.75	1																							
Spk	-0.57	0.32	0.77	1																								
Svk	-0.63	0.54	1																									
Sr1	-0.47	1																										
Sr2	1																											

3. DISCUSSION OF TEST RESULTS

If we consider correlation coefficients with absolute value greater than 0.7 as significant (highlighted in the Table 4.), it can be concluded, that there are many dependences between the surface texture parameters after the slide burnishing process. Most parameters are correlated with one of the following: *Sa*, *Sv*, *Str*, *Ssk*, *Svk*, *Std*, *Svi* or *Sp*. These parameters were found to be representative for the most of the others, as it was shown in Table 5. It also revealed parameters, which have been very poorly correlated with the others: *Sds* and *Sr1*.

Table 5. Correlation coefficient values of surface texture parameters.

Representative parameter	Correlated parameters	Correlation coefficient value
Sa	*Sdq*	0.80
	Ssc	0.73
	Sdr	0.74
	Sk	0.93
	Spk	0.89
Sv	*St*	0.96
	Sz	0.91
	Smmr	1
	Sbi	0.72
Str	*Sal*	0.77
	Sci	-0.79
Ssk	*Sku*	-0.92
	Sfd	0.91
Svk	*Sq*	0.96
	STp	0.77
Std	*SPc*	-0.72
Svi	*Sr2*	-0.86
Sp	*Smvr*	1
Sds	-	-
Sr1	-	-

For some above mentioned representative parameters, but also for parameters with poor correlation coefficient, the calculation procedure was performed according to the methodology given in [32], [33]. This allowed us to obtain the regression equation, which defines the influence of the input parameters of the slide burnishing process on the obtained surface texture parameters. Regression equation coefficients were calculated and then their relevance and repeatability of experimental results were assessed. Adequacy of the obtained regression equation has been rated at the end. This calculation cycle has been performed repeatedly, each time for the different parameters from the above listed surface texture parameters. The result is a few mathematical models in the form of polynomials of the second degree. These models not only allow us to determine the direct influence of input parameters of the slide diamond burnishing process, but also allow us to observe the effects of interactions (synergy) of these parameters. Following mathematical relations have been obtained:

- influence of the slide diamond burnishing parameters on the arithmetical mean height:
-

$$Sa = 0.624 - 0.371r + 0.002P + 2.887f + 0.054r^2 - 0.029Pf \quad (1)$$

- influence of the slide diamond burnishing parameters on the root-mean-square height:

$$Sq = 1.651 - 0.739r - 0.0017P + 0.123r^2 \quad (2)$$

- influence of the slide diamond burnishing parameters on the total height:

$$St = 13.546 + 3.118r - 0.228P + 133.625f + 0.0009P^2 - 44.542rf \quad (3)$$

- influence of the slide diamond burnishing parameters on the texture direction of the surface:

$$Std = -66.234 + 101.377r - 1.219P - 15.007r^2 + 0.0061P \quad (4)$$

- influence of the slide diamond burnishing parameters on the texture aspect ratio:

$$Str = 0.587 - 0.002P \quad (5)$$

- influence of the slide diamond burnishing parameters on the root mean square gradient of the surface:

$$Sdq = 0.150 - 0.103r + 0.0004P + 0.662f + 0.019r^2 - 2.503f^2 - 0.0001rP - 0.065rf - 0.0017Pf \quad (6)$$

- influence of the diamond burnishing parameters on the arithmetic mean summit curvature of the surface:

$$Ssc = 0.019 - 0.12r + 0.0001P + 0.071f + 0.002r^2 - 0.326f^2 - 0.00001rP - 0.01075rf - 0.0006Pf \quad (7)$$

- influence of the slide diamond burnishing parameters on the kurtosis of the surface:

$$Sku = -129.290 + 233.738r - 1.444P - 260.347f - 44.767r^2 + 0.349rP \quad (8)$$

- influence of the slide diamond burnishing parameters on the skewness of the surface:

$$Ssk = 4.196 - 12.553r + 0.224P - 14.267f + 1.702r^2 - 0.034rP + 44.979rf - 1.207Pf \quad (9)$$

Experiments have shown that the slide diamond burnishing process is an effective method of treatment of the parts made of 317Ti stainless steel. It allows us to obtain not

only a very smooth surface, but also other advantageous features of surface texture without any difficulties. For all obtained dependencies with assumed experimental implementation conditions, all received equations except one, are non-linear. The only linear equation is a model describing the relationship between the input parameters of slide diamond burnishing process and surface texture *Str* parameter. The calculated regression equations are useful for further analysis (e.g., optimization) and allow for selection of input parameters to obtain a surface texture with desired characteristics during the slide diamond burnishing.

4. CONCLUSIONS

1. Slide diamond burnishing process is a relatively easy method to obtain a good surface smoothness of parts made of 317Ti stainless steel.
2. For the comprehensive assessment of the state of the surface texture after the slide roller burnishing process it is enough to measure 10 representative parameters. The other parameters are relatively well correlated with them.
3. The influence of the slide diamond burnishing process input parameters on the surface texture parameters was described by the obtained regression equations. It allowed the disclosure of the synergies of individual parameters of the slide diamond burnishing process.

REFERENCES

[1] Oczos, K.E., Liubimov, V. (2003). *Struktura geometryczna powierzchni [Surface Geometric Structure]*. Rzeszow, Poland: Rzeszow Technical University Publishing House. (in Polish)

[2] Berglund, J., Brown C.A., Rose, B.G., Bay, N. (2010). Milled die steel surface roughness correlation with steel sheet friction. *CIRP Annals - Manufacturing Technology*, 59, 577–580.

[3] Sedlacek, M., Podgornik, B., Vizintin, J. (2012). Correlation between standard roughness parameters skewness and kurtosis and tribological behaviour of contact surfaces. *Tribology International*, 48, 102-112.

[4] Stout, K., Davis, E.I., Sullivan, P.I. (1990). *Atlas of Machined Surfaces*. Chapman and Hall.

[5] Stout, K.J., Dong, W.P., Mainsah, E. (1993). *A proposal for standardization of assessment of three-dimensional micro-topography - Part 1. Surface digitisation and parametric characterisation*. University of Birmingham.

[6] Thomas, T.R. (1999). *Rough Surfaces*. Imperial College Press.

[7] Niemczewska-Wójcik, M. (2017). Multi-sensor measurements of titanium alloy surface texture formed at subsequent operations of precision machining process. *Measurement*, 96, 8–17.

[8] Low, K.O. (2011). Surface characteristics modification of polyoxymethylene and polyurethane using burnishing. *Tribology Transactions*, 54 (1), 96-103.

[9] Yusof, N.F.M., Ripin, Z.M. (2014). Analysis of surface parameters and vibration of roller bearing. *Tribology Transactions*, 57 (4), 715-729.

[10] Coutinho, R., Marinescu, I.D. (2005). Methodology to compare 3-D and 2-D parameters for the optimization of hard turned surfaces. *Machining Science and Technology*, 9 (3), 383-409.

[11] Wang, G., Zhou, X., Meng, G., Yang, X. (2017). Modeling surface roughness for polishing process based on abrasive cutting and probability theory. *Machining Science and Technology*, 22 (1), 86-98.

[12] Grzesik, W. (2016). Prediction of the functional performance of machined components based on surface topography: State of the art. *Journal of Materials Engineering and Performance*, 25 (10), 4460–4468.

[13] Wagner, J.J., Jenson, A.D., Sundararajan, S. (2017). The effect of contact pressure and surface texture on running-in behavior of case carburized steel under boundary lubrication. *Wear*, 376-377, 851-857.

[14] Krzyzak, Z., Pawlus, P. (2006). 'Zero-wear' of piston skirt surface topography. *Wear*, 260, 554–561.

[15] Profito, F.J., Vlădescu, S-C., Reddyhoff, T., Dini, D. (2017). Transient experimental and modelling studies of laser-textured microgrooved surfaces with a focus on piston-ring cylinder liner contacts. *Tribology International*, 113, 125–136.

[16] Khelifi, C., Do, M.T., Kane, M., Adenot Meyer, M. (2017). Wear and wet friction of steel tracks for rubber-tired metros. *Wear*, 376-377, 1912-1918.

[17] Niemczewska-Wójcik, M. (2016). Multi-sensor measurements of titanium alloy surface texture formed at subsequent operations of precision machining process. *Measurement*, 96, 8–17.

[18] Kang, Y.S., Hager, C.H., Evans, R.D. (2015). Effects of skewed surface textures on lubricant film thickness and traction. *Tribology Transactions*, 58 (3), 397-406.

[19] Gherca, A., Fatu, A., Hajjam, M., Maspeyrot, P. (2013). Influence of surface geometry on the hydrodynamic performances of parallel bearings in transient flow conditions. *Tribology Transactions*, 56 (6), 953-967.

[20] Sedlaček, M., Gregorčič, P., Podgornik, B. (2017). Use of the roughness parameters Ssk and Sku to control friction—a method for designing surface texturing. *Tribology Transactions*, 60 (2), 260-266.

[21] Wang, L., Ouyang, W., Gao, W., Xu, B. (2017). Instrumental evaluation of fabric abrasive wear using 3D surface images. *Journal of the Textile Institute*, 108 (5), 846-851.

[22] Lu, W., Zhang, G., Liu, X., Zhou, L., Chen, L., Jiang, X. (2014). Prediction of surface topography at the end of sliding running-in wear based on areal surface parameters. *Tribology Transactions*, 57 (3), 553-560.

[23] Masuko, M., Aoki, S., Suzuki, A. (2005). Influence of lubricant additive and surface texture on the sliding friction characteristics of steel under varying speeds ranging from ultralow to moderate. *Tribology Transactions*, 48 (3), 289-298.

[24] Eiss, N.S., Bayraktaroglu, M.M. (1980). The effect of surface roughness on the wear of low-density polyethylene. *ASLE Transactions*, 23 (3), 269-278.

[25] Shi, X., Wang, L., Qin, F. (2016). Relative fatigue life prediction of high-speed and heavy-load ball bearing based on surface texture. *Tribology International*, 10, 364–374.

[26] Trauth, D., Klocke, F., Welling, D., Terhorst, M., Mattfeld, P., Klink, A. (2016). Investigation of the surface integrity and fatigue strength of Inconel718 after wire EDM and machine hammer. *International Journal of Material Forming*, 9 (5), 635–651.

[27] Qi, Q., Li, T., Scott, P.J., Jiang, X. (2015). A correlational study of areal surface texture parameters on some typical machined surfaces. *Procedia CIRP*, 27, 149–154.

[28] Rosen, B.G., Anderberg, C., Ohlsson, R. (2008). Parameter correlation study of cylinder liner roughness for production and quality control. *Proceedings of the Institution of Mechanical Engineers, Part B: Journal of Engineering Manufacture*, 222, 1475-1487.

[29] Das, J., Linke, B. (2017). Evaluation and systematic selection of significant multi-scale surface roughness parameters (SRPs) as process monitoring index. *Journal of Materials Processing Technology*, 244, 157–165.

[30] Franco, L.A., Sinatora, A. (2015). 3D surface parameters (ISO 25178-2): Actual meaning of Spk and its relationship to Vmp. *Precision Engineering*, 40, 106–111.

[31] Korzynski, M. (2013). Slide diamond burnishing. In *Nonconventional Finishing Technologies*. Warsaw, Poland: Polish Scientific Publishers PWN.

[32] Korzynski, M. (2017). *Metodyka eksperymentu [Methodology of Experiment]*. Warsaw, Poland: Science Publishing Home. (in Polish)

[33] Korzynski, M., Lubas, J., Swirad, S., Dudek, K. (2011). Surface layer characteristics due to slide diamond burnishing with a cylindrical-ended tool. *Journal of Materials Processing Technology*, 211 (1), 84-94.

Received December 12, 2017.
Accepted May 14, 2018.